

LIGHT TRAPPING AND ABSORPTION ENHANCEMENT FOR HIGH PERFORMANCE SOLAR
CELLS AND INFRARED PHOTODETECTORS

by

LI CHEN

Presented to the Faculty of the Graduate School of
The University of Texas at Arlington in Partial Fulfillment
of the Requirements
for the Degree of

DOCTOR OF PHILOSOPHY

THE UNIVERSITY OF TEXAS AT ARLINGTON

MAY 2010

Copyright © by LI CHEN 2010

All Rights Reserved

ACKNOWLEDGEMENTS

First and foremost I would like to express my greatest thanks to my advisor, Professor Weidong Zhou for his instruction and direction during my pursuit of Ph.D. at UTA. His stringent scientific methods and diligent research attitude taught so much from research to life. I must thank Professor Meng Tao for his sincere help and support on my entire solar cells work. I want to thank Professor Mingyu Lu for his sustaining support on my 2D PCS photodetector simulations. I would like to express my appreciations to the rest of my committee members, Professor Michael Vasilyev and Professor Michael Jin for their suggestion and help on my thesis. I would like to thank Professor Zeynep Celik-Butler for her support during my application to UTA. I also want to thank all professors who taught me EE at UTA.

I would like to express my special thanks to Dr. Zexuan Qiang for his support and cooperation in the photodetector simulations and testing. I also would like to express my special thanks to Hongjun Yang for his support and cooperation in the fabrication and testing. I want to express my appreciations to Dr. Yuehui Wang and Rajesh Tummala for their help and support in the solar cells coating process. I would like to thank all other group members: Dr. Deyin Zhao, Dr. Weiquan Yang, Santhad Chuwongin, Tapas Saha, Yi-Chen Shuai, Rui Li and Arvinder M Chadha for their help.

I want to express my appreciation to Dr. Gail J. Brown from Air Force Research Laboratory for her guidance and support on the photodetector project. Special thanks go to Professor Zhenqiang Ma at University of Wisconsin-Madison and his students Huiqing Pang, Lei Sun for transferring Fano filters. Special thanks to Professor Jian Xu in Pennsylvania State University and his students Ting Zhu, Shuai Gao for providing PbSe QDs solutions. Special thanks also go to Duke University Professor Adrienne Stiff-Roberts and her student Ryan Pate for depositing PbSe QDs.

I would like to thank all staff members at Nanofab Center. Special thanks go to Dennis Bueno and Eduardo Maldonado for training me various instruments in the clean room.

I would like to appreciate my friends in UTA: they are Dr. Qitao Zhao, Dr. Deqiang Wang, Dr. Peng Xie, Lun Ma, Yuan Long, Kunhee Han, Xiaofei Han, Liang-Chieh Ma, and many others.

Finally, I thank my family members: my parents Xiusheng Chen and Fengqiao Liu, my wife Juanzhen He, my daughter Nicole Chen, my parents-in-law Shiquan He and Baojin Chen and my brother Fei Chen. Their eternal love and support are invaluable.

This work was supported by Air Force Office of Scientific Research (AFOSR), Air Force Research Laboratory (AFRL), NASA Texas Space Grant Consortium, and National Science Foundation (NSF), NanoFAB Center at UTA and University of Texas, Austin MRC center, STEM Doctoral Research Assistant Fellowship.

April 16, 2010

ABSTRACT

LIGHT TRAPPING AND ABSORPTION ENHANCEMENT FOR HIGH PERFORMANCE SOLAR CELLS AND INFRARED PHOTODETECTORS

LI CHEN, PhD

The University of Texas at Arlington, 2010

Supervising Professor: WEIDONG ZHOU

This dissertation presents the work on light trapping and absorption enhancement in solar cells and infrared photodetectors. Hemispherical microstructure based omni-directional anti reflection (Omni-AR) coating has been designed and developed for solar cells, based on rigorous coupled-wave analysis (RCWA) and convective coating process. Omni-AR coating enhances light absorption in solar cells, due to the reduced reflection on the structured solar cell surfaces, and the increased optical path length (OPL) inside the solar cells. Omni-AR coating has been demonstrated as a cost-effective light trapping approach for different material systems, with very low reflection and high transmission over a large range of incident angles (0° to 60°) and over a wide spectral range (400-1000nm). Omni-AR coating has also been applied on commercial solar cells based on the cost-effective solution techniques. With omni-AR coating, we obtained increased short circuit current, and increased conversion efficiency, in both organic solar cells and amorphous silicon solar cells.

Significant infrared absorption enhancement can also be achieved in photonic crystals (PC) cavities. In 1D PC structures, the ratio of absorption enhancement to suppression at the photonic bandedge can be as high as 40. The absolute infrared absorption can be tuned and

enhanced by more than 90% in both the defect cavity and the resonance cavity 1D PC structures. In 2D photonic crystals slab (PCS) cavities, the absorption enhancement factor is more than 6000 under lateral light stimulation. With vertical light stimulation, the enhancement factor is about 100. Enhanced infrared absorption can also be obtained through Fano resonance based PC structures. The light is effectively coupled between the in-plane discrete resonance modes and the vertical continuum radiation modes. Based on this principle, 2D PC patterned silicon nanomembrane (SiNM) Fano filters are fabricated and transferred onto transparent substrates. This type of ultra compact SiNM Fano filters demonstrates strong angular and polarization dependent transmission properties. More significantly, enhanced absorption is achieved via the incorporation of the spectrally aligned colloidal quantum dots (CQDs) into the air holes of Fano filters. Finally, we propose two kinds of spectrally-selective photodetector structures, based on Fano resonance filters.

TABLE OF CONTENTS

ACKNOWLEDGEMENTS	iii
ABSTRACT	v
LIST OF ILLUSTRATIONS.....	x
LIST OF TABLES	xvii
Chapter	Page
1. INTRODUCTION.....	1
1.1 Background	1
1.1.1 Light Trapping in Solar Cells	2
1.1.2 Infrared Photodetectors (<i>IRPD</i>)	3
1.1.3 Enhanced Infrared Absorption in Photonic Crystals	5
1.2 Overview of Dissertation	7
2. OMNI-DIRECTIONAL ANTI-REFLECTION (OMNI-AR) COATINGS FOR SOLAR CELLS.....	9
2.1 Background on AR Coatings.....	9
2.1.1 Planar Thin Film AR Coatings.....	9
2.1.2 Graded Index AR Coatings	11
2.1.3 Moth – Eye AR Coatings.....	11
2.1.4 Textured Surface AR Coatings	12
2.2 Optical Design of Omni-AR Coatings.....	13
2.2.1 Simulation Method and Theory	14
2.2.2 Hemispherical Surface and Omni-AR Structures.....	18
2.2.3 Pyramidal, Conical, versus Hemispherical Structures	22
2.2.4 Index Matching to Si Substrate	24

2.2.5 Solar Cell Performance	26
2.3 Omni-AR Coatings on Different Substrates	29
2.4 Omni-AR Coatings Integration with Commercial Solar Cells	35
3. INFRARED ABSORPTION ENHANCEMENT IN ONE-DIMENSIONAL (1D) PHOTONIC CRYSTAL (PC).....	40
3.1 Simulation Approach for 1D PC	40
3.2 Absorption Enhancement at Photonic Bandedge	42
3.3 Defect Cavity versus Resonance Cavity	44
4. TWO DIMENSIONAL (2D) ABSORPTIVE PHOTONIC CRYSTAL SLAB (PCS) SIMULATION	47
4.1 In-Plane Source in 2D PCS.....	47
4.1.1 2D PCS Configuration	47
4.1.2 3D FDTD Simulation Setup	49
4.1.3 Absorption Enhancement.....	51
4.2 Vertical Source above 2D PCS	55
4.2.1 Simulation Setup	55
4.2.2 Absorption Enhancement.....	57
5. INFRARED ABSORPTION WITH FANO RESONANCE	62
5.1 Fano Resonance in PCS.....	62
5.2 Design and Fabrication of Fano Filters on Transparent Substrates	62
5.3 Angular and Polarization Dependent Transmission on Transferred Fano Filters	66
5.3.1 Surface-Normal Incidence	68
5.3.2 Incident Beam Plane Parallel with x-z Plane (Γ_X direction)	69
5.3.3 Incident Beam Plane 45 Degree off x-z Plane (Γ_M direction)	73
5.3.4 Filter Transmission Contrast Ratio	74
5.3.5 Spectral Engineer from Bending	76

5.4 Absorption Enhancement of PbSe/PbS Colloidal Quantum Dots (CQDs) in Flexible Fano Filters	76
5.4.1 Direct Absorption Measurement	76
5.4.2 Principle of Absorption Enhancement	79
6. INFRARED PHOTODETECTORS DESIGN BASED ON FANO FILTERS	86
6.1 Schottky Photodetectors Design	86
6.2 PN Photodetectors Design	90
7. CONCLUSIONS AND FUTURE WORK	92
7.1 Conclusions	92
7.2 Suggestion and Future Work	92
7.2.1 Light Trapping in Other Types of Solar Cells	92
7.2.2 2D PCS Vertical Illumination Absorption	93
7.2.3 Photodetector Design and Fabrication	93
APPENDIX	
A. LIST OF PUBLICATIONS	95
REFERENCES	99
BIOGRAPHICAL INFORMATION	107

LIST OF ILLUSTRATIONS

Figure	Page
1.1	Three major categories of light trapping in solar cells.....2
2.1	Simulated quarter wavelength planar thin film AR structures with ideal indices and thicknesses for (a) single and (b) triple layers. 10
2.2	Low GRIN AR structure by physical vapor deposition[47] 11
2.3	Various nanostructures by RIE[18] 12
2.4	Pyramid microstructure created by KOH wet etching[17] 13
2.5	Cartoon of RCWA based simulation for hemisphere microstructure 14
2.6	Hemispherical grating as the basic anti-reflection structure for simulation: (a) Three-dimensional view of the square lattice; (b) top view and (c) cross-sectional view of the basic structure..... 15
2.7	Light trapping in Omni-AR microstructure (a) under normal incident light (b) under oblique incident light..... 16
2.8	Crystal silicon complex index dispersion curve $n = n + ik$ from ultraviolet to infrared and (b) refractive index dispersion curve of silicon and silicon dioxide used in our simulation..... 17
2.9	Simulation results for hemispherical structures with index $n_1 = 1.5$ on silicon substrate: (a) Square lattice hemispherical structure with radius $R = 1\mu\text{m}$ and lattice constant $a = 2.5\mu\text{m}$ and (b) Omni-AR structure with hemispherical structure on top of a thin film with the same index n_1 and thickness $h_1 = R = 1\mu\text{m}$ 18
2.10	(a) Simulation results for Omni-AR structure on Si substrate with a SiN_x thin film in between ($n_2 = 2.0$ and $h_2 = 75\text{ nm}$); Other simulation parameters are the same as those in Figure 2.5(b). The reflectivity for (b) small incident angles ($\theta = 0^\circ$ and 30°) and large incident angles ($\theta = 60^\circ$ and 75°), for two cases: SiN_x coated Si and Omni-AR on SiN_x coated Si. 19
2.11	Packing density impact for the proposed hemispherical Omni-AR structure similar to the one in Figure 2.10 (a) with $R = 1\mu\text{m}$, $n_1 = 1.5$ and lattice constant (a) $a = 2\mu\text{m}$ and (b) $a = 5\mu\text{m}$. (c) Surface normal reflectivity for different packing densities20

2.12	Spherical radius impact for the proposed hemispherical Omni-AR structure similar to the one in Figure 2.10 (a) with $R/a = 0.4$, $n_1 = 1.5$ and spherical radius (a) $R = 0.5 \mu\text{m}$ and (b) $R = 2\mu\text{m}$. (c) Surface normal reflectivity and (d) large incident angle reflectivity for different spherical radius.....	21
2.13	The structures and simulation results for three differently shaped structures: (a) pyramids, (b) cones and (c) hemispheres. Both non-close-packed structures and close-packed structures are simulated for comparison.....	23
2.14	Reflectivity simulation results for index matching of silica Omni-AR to Si substrate: (a) SiNx film with a fixed index of 2.0 and (b) graded index film with index varying linearly from Omni-AR ($n = 1.5$) to substrate ($n = 4.0$).....	24
2.15	Reflectivity simulation results for graded index Omni-AR structures on high index Si substrate: (a) Index profile from air ($n = 1.0$) to SiNx film below ($n = 2.0$) and (b) ideal index matching from air to Si substrate (n varying from air $n = 1.0$ to Si $n = 4.0$).....	25
2.16	Reflectivity simulation result for ideal GRIN thin films on Si substrate, n varies from 1.0 to 4.0.....	25
2.17	Simulation procedure for solar cell performance evaluation based on the optical characteristics of solar cell thin films.....	26
2.18	Solar weighted reflection (SWR) on Omni-AR w/ SiNx microstructure and reference SiNx on Si microstructure(both are shown in Figure 2.10).....	27
2.19	(a)Short-circuit current density(J_{sc}) of Omni-AR w/ SiNx and SiNx on Si (both are shown in Figure 2.10). (b) J_{sc} improvement with Omni-AR.....	27
2.20	Normalized photons number and normalized total power in nine different structures.....	29
2.21	(a) Omni-AR coating based on monolayer of spherical particles and spin-on-glass (SOG) film; (b) Scanning electron micrographs of fabricated Omni-AR coatings: (i) top view; (ii) cross-sectional view before SOG film and (iii) cross-sectional view after SOG film.	30
2.22	Total transmittance under normal incidence of quartz wafers with various surface coatings.	31
2.23	(a) Angle-dependent transmissivity of a quartz wafer before and after an Omni-AR coating; (b) Schematic of experimental setup for angle dependent total transmittance setup.	31
2.24	Simulated transmissivity at different incident angles for quartz wafers with and without an Omni-AR coating.....	33

2.25	2 μ m nanoparticles self assembly on Si by (a) dip coating (b) convective coating	34
2.26	(a) Convective coating Omni-AR on 6x6" glass slide (b) SEM image of Omni-AR coating on glass	34
2.27	Convective coating setup	35
2.28	a-Si (a) w/o (b) w/ Omni-AR coating (c) SEM picture of 1 μ m Silica nanoparticles self assembly on a-Si solar cells (d) SEM picture after Omni-AR formed on a-Si solar cells	36
2.29	Reflection measurements on a-Si solar cells before and after Omni-AR coating under normal incident	36
2.30	Solar Cell I-V characterization (a) setup (b) as example of 45° testing under AM 1.5 illumination.....	37
2.31	I-V measurement results for a-Si solar cells before (solid lines) and after (dash lines) Omni-AR coating under incident angle from 0° to 75°	37
2.32	Organic Solar Cells (a) before and (b) after Omni-AR coating	38
2.33	I-V measurement results for organic solar cells before (solid lines) and after (dash lines) Omni-AR coating under incident angle from 0° to 75°	38
2.34	Performance improvement after Omni-AR coating in I _{sc} (in solid blue) and efficiency (in dash red) with incident angle from 0° to 75°	39
3.1	Structures under simulation: (a) 1D PC structure with absorptive layers; (b) Reference bulk absorptive material with equivalent absorption thickness.	40
3.2	Schematic of the transfer matrix method (TMM) theory.....	41
3.3	Simulated absorptance for 1D PCs, with the refractive index of the absorptive layer to be either (a) lower or (b) higher than that of the non-absorptive layer. The absorptance for the reference bulk material is also shown as the reference.	42
3.4	(a) Schematically show the 1D PC (b) Enhanced absorption in wavelength domain at bandedge with periods N=5,10 for 1D PC consists by PbSe and Si. Inset shows the absorptance at frequency domain.....	43
3.5	(a) PC with defect: distributed absorption at defect level with $n_1=3.6+0.028i, n_2=3.0, n_s=3.5$. (b) Resonant cavity: cavity absorption at defect level with $n_1=3.5, n_2=3.1, n_s=3.5$, and $n_d=5+0.03i$	44
3.6	Absorption comparison of Figure 3.5(a), (b) and bulk with periods from 10 to 20.	44

3.7	Absorptance peak optimization by (a) tuning bottom DBR period (b) by tuning defect absorptive layer thickness	45
4.1	2D absorptive PCS (a) top view of H_1 defect cavity (b) cross-section for H_1 H_0 and reference bulk.....	48
4.2	(a) PBG dispersion plot for 2D PCS (b) Simulated PBG and the defect mode characteristics in the single defect H_1 PC cavity. The defect level was confirmed to be a dipole mode(inset) with center wavelength (1.504 μm) close to the center of the PBG (1.41 to 1.67 μm)	48
4.3	(a) Top view (b) Cross-section view of 3D FDTD simulation setup with perfectly matched layers as the boundary. An in-plane dipole source was placed at the center of the slab (red square) with monitors (blue lines) surrounding the simulation domain for both vertical and in-plane power monitoring.....	49
4.4	In-plane light source simulation on detected power densities from all monitors. Spectral power density based on the vertical and in-plane monitors in (a) single defect H_1 PC cavity; (b) defect-free H_0 PC cavity; and (c) reference slab without PC structure. To show the fine spectral features and relative transmitted power spectra density, the monitored values were plotted in both linear scale (top) and log-scale for both vertical monitor ($H_{1\perp}$, middle panel) and in-plane monitor ($H_{1\parallel}$,bottom panel), respectively.	51
4.5	(a) Linear scale absorption of H_1 cavity (b) Log-scale absorption power spectra of both H_1 and H_0 (c) and (d) are value after normalization with respect to the reference sample (slab without PC) correspond to (a) and (b) respectively. $k_a = 0.016$ for all cases.	52
4.6	(a) Absorption enhancement factor for H_1 and H_0 cavity for different absorption coefficients and different surrounding air hole periods. Note the dominant absorption occurs along the vertical direction (top). (b) The impact of air hole period: normalized absorption power spectra for air hole periods of 4 and 3 in single defect H_1 cavity. Note the change in the enhancement factor (peak value) and corresponding reduction in the cavity Q.	53
4.7	Total quality factor Q for the single defect cavity H_1 ($H_{1\perp}$, $H_{1\parallel}$) at different absorption coefficients	54
4.8	Absorption power spectra (a) before and (b) after normalization with respect to the reference sample (slab without PC) for different absorption coefficients. Note a reduction in normalized absorption at peak wavelength with the increase of absorption coefficient.....	55
4.9	3D FDTD simulation setup with vertical dipole source location and launch direction shown. The relative locations for the vertical and in-plane monitors enclosing the entire simulation domain are also shown with blue lines, more details can be found in Table 4.3	56

4.10	Vertical light source simulation on detected power densities from all monitors. Spectral power density based on the vertical and in-plane monitors in (a) single defect H_1 PC cavity; (b) defect-free H_0 PC cavity; and (c) reference slab without PC structure. Top panel shows vertical power middle panel shows in-plane power and bottom panel shows total power.....	58
4.11	Absorption power spectra before normalization (a) (linear scale) and (b) (log scale)) and after normalization (c) (linear scale)and (d) (log scale)) with respect to the reference sample (slab without PC) for $ka=0.016$	59
4.12	Absorption power spectra (a) before and (b) after normalization with respect to the reference sample (slab without PC) for different absorption coefficient. Note a reduction in normalized absorption at peak wavelength with the increase of absorption coefficient.	60
4.13	Vertical light source (a) total quality factor Q for $H_{1\perp}$ and $H_{1\parallel}$ (b) absorption enhancement and suppression factor result for H_1 and H_0 cavity for different absorption coefficients.....	60
5.1	(a) Measured and simulated surface normal transmission spectra for the fabricated patterned SiNM Fano filters on glass substrates; (b) Simulated dispersion plot for Fano filters on glass substrates, where $r/a=0.19$, $t/a=0.25/0.6\sim 0.417$. The refractive indices of silicon and glass are 3.48 and 1.5, respectively. Note the surface-normal transmission dips/peaks at all three wavelength points ($\lambda_1, \lambda_2, \lambda_3$) agree well with the dispersion plot $\omega_1, \omega_2, \omega_3$ at Γ point. (c) and (d) The simulated snapshots of electrical field intensity profiles for on-resonance wavelength (λ_1) and off-resonances, respectively.....	63
5.2	Fano resonance change from small variation of air holes	65
5.3	Fano filter fabrication procedure (a) pattern generation by e-beam lithography and RIE (b) pattern release by BHF etching (c) wet pattern transferring to obtain Fano filter on transparent substrates	66
5.4	Angle and polarization definition for incident light beam onto patterned SiNM Fano filters. The PC lattice and Brillouin zone symmetric points (Γ , X and M) in the k -space are also shown in the inset.	67
5.5	Measured surface-normal transmission spectra at different angles ϕ for the incident beam either (a) without polarizer; or (b) with polarizer fixed at $\psi=0$	68
5.6	Measured transmission intensity contour plots under different polarization conditions (a) Γ - X direction with p -polarization light (b) Γ - X direction with s -polarization light; (c, d) Simulated transmission spectra under p - and s -polarizations, respectively.....	69

5.7	Snapshots of electric field distributions of Fano filters at large incident angle ($\theta=20^\circ$ and $\theta = 0^\circ$): (a) p -polarization, on-resonance; (b) p -polarization, off-resonance; (c) s -polarization, on-resonance; and (d) s -polarization, off-resonance.	70
5.8	Measured transmission intensity plots for incident beam lies within x - z plane (along Γ - X direction) with (a) hybrid polarization ($\psi=45^\circ$) and (b) without polarization. (c) Simulated transmission with the same conditions shown in (a). (d) Dispersion plot along Γ - X shown the p - and s -polarization states.	72
5.9	Measured transmission intensity contour plots under different polarizations (a) Γ - M direction with p -polarization light (b) Γ - M direction with s -polarization light; (c) Simulated transmission spectra with p -polarizations; and (d) (c) Simulated transmission spectra with s -polarizations.	73
5.10	(a) Measured transmission intensity contour plots for incident beam lies at 45 degree off x - z plane (Γ - M direction) with hybrid polarization ($\psi=45^\circ$). (b) Simulated transmission spectra for different incident angles with the same incident beam orientation and polarization shown in (a). (c) Dispersion plot along Γ - M direction shown both p - and s -polarization states.	74
5.11	Comparison of the simulated (Simu.) and experimental (Expr.) transmission contrast ratios for the dominant resonant modes for beam along: (a) Γ X direction for p - and s -polarizations (Figure 5.6); (b) Γ X direction for hybrid-polarization and un-polarized beams (Figure 5.8); (c) Γ M direction for p - and s -polarizations (Figure 5.9); and (d) Γ M direction for hybrid-polarizations (Figure 5.10)	75
5.12	Measured transmission intensity map of Fano filter with dominant Fano resonance at 1560nm under different bending curvature with (a) p -polarization (b) s -polarization and (c) hybrid-polarization.	76
5.13	SEM of Fano filter (a) Before (b) After PbSe CQDs deposition by drop casting. TEM of QDs is shown in inset (c) Typical absorption spectrum of PbSe QDs (d) Schematic of SiNM based Fano filters filled with CQDs on flexible substrates. Surface normal optical measurement is also shown for both transmission (T) and reflection (R).	77
5.14	(a) Schematically show (b) Real image of simultaneous transmission and reflection experimental setup for Fano filter.	78
5.15	Measured transmission and reflection spectra for Fano filter without and with PbSe CQDs	79
5.16	Experimental and simulated absorption characteristics for the Fano filter filled with CQDs. Shown in the inset is the spectra of CQD extinction coefficient, k	80

5.17	(a) Absorption of Fano filter and glass substrate (b) Absorption enhancement for Fano filter	81
5.18	(a) Three sets of QDs with different absorption peak locations; (b) Three different Fano filters with different resonance locations; and (c) Absorption enhancement factors for these three sets of samples.....	82
5.19	Measured incident angle θ dependent p-polarization transmission along with $\psi=0^\circ$, $\phi=0^\circ$ for Fano filter on PET substrate; solid and dash curves accounts for with and without PbSe QDs respectively.....	84
5.20	(a) Shows Fano filter transmission (solid blue) and PbSe quantum dots absorption (red dash) used for this simulation (b) Corresponding simulated absorption in this Fano filter on PET substrate with p-polarization (solid curves) and s-polarization light (dash curves)	84
6.1	Schematically show the Schottky junction photodetector model	86
6.2	(a) The extinction coefficient of PbSe QDs used for the simulation (b) Absorption based on different QD locations on the Fano filters.	88
6.3	Schematically show (a)the QDs pillow on the glass substrate (b) QDs filled in the Fano filter (c) The absorption in case(a) and (b) (d) The absorption enhancement.....	88
6.4	(a) The QDs layer above the glass substrate (b) The QDs layers coated on the Fano filter (c) The absorption in case(a) and (b) with different QD layer thickness (d) The absorption enhancement of different thick QD layers	89
6.5	Schematically show the PN junction photodetector model	90
6.6	The thickness of top and bottom Fano filter impact on absorption	91

LIST OF TABLES

Table		Page
1.1	Current infrared photodetectors status and challenges	4
2.1	Parameters of pyramid, cone and hemisphere shaped microstructures	22
2.2	Description and key parameters of nine different structures.....	28
4.1	2D absorptive photonic crystal slab parameters.....	47
4.2	3D FDTD simulation setup for 2D PCS with in-plane light source	50
4.3	3D FDTD simulation setup for 2D PCS with vertical light source	56
5.1	1550nm Fano filter design parameters	62
5.2	Variation of bandwidth, quality factor and lifetime between simulation and fabrication	64
5.3	Three set of Fano filter absorption experiments with different colloidal quantum dots.....	83
6.1	Some parameters in Schottky junction photodetector	87
6.2	Design parameters for pn junction photodetectors	91

CHAPTER 1
INTRODUCTION
1.1 Background

Fossil fuels provide more than 80% energy source but also produce more than 80% carbon dioxide[1, 2]. In order to prevent further increase of the carbon dioxide concentration in the atmosphere, carbon-free energy source like geothermal, nuclear, wind, solar, etc, must be developed. Among them, solar energy probably is the most promising form of energy abundant enough to meet the requirements that the planet will face in the future[3, 4]. As a matter of fact, solar energy capacity has been kept increasing at double digit percentage pace over the last few years. However, due to the 8-10 times higher production cost than fossil fuels energy for producing a given amount of power, currently solar energy only shares less than 0.1% of the whole energy market[1, 2]. High efficiency with low cost solar cell is highly desirable. Increasing light absorption by light trapping technology is one direction to improve the efficiency in terms of photocurrent for solar cells. How to develop a cost effective light trapping technology becomes vital to solar cells.

As another important photonic device, infrared photodetectors (IRPD) with high spectrally selective response are highly desirable for applications such as hyper-spectral imaging and gas sensing. However, current dominant HgCdTe (MCT) photodetectors require costly growth equipment, work at low temperature but lack large area uniformity[5]. Quantum well infrared photodetectors (QWIP) can achieve large area uniformity but also involved with complicated design and process to achieve efficient normal incident absorption[6]. Quantum dots infrared photodetectors (QDIP) have better performance theoretically but in practice face some issues such as low absorption efficiency, non-uniform dots distributions and dot sizes, and high dark current[7, 8].

This dissertation presents high spectral resolution photonic crystal (PC) based quantum dots infrared photodetectors (QDIPs) and proposes an omni-dimensional anti-reflection (Omni-AR) coating approach for light trapping in solar cells.

1.1.1 Light trapping in solar cells

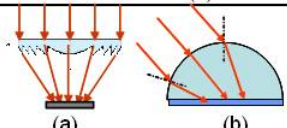
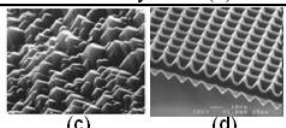
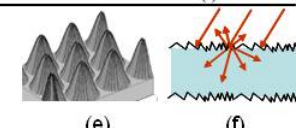
Length Scale	Macro-Scale (>1mm) Light Concentrator	Micro-Scale (1-100 μ m) Textured Surfaces	Nano-Scale (1-1000nm) Moth's Eye (Lambertian)
Structures	•Fresnel Lens (a) •Domed Lens (b)	•Pyramid (c) •Inverted Pyramid (d)	•Moth's Eye (e) •Diffusive Surface (f)
Examples			
Processing	•Bulk optics •Efficient	•Efficient •Wet etching	•Dry or wet etching
Conditions	•Large area (Bulky) •Solar tracker	•Crystal orientation dependent •Only suitable for Bulk Si	•Nanoscale pattern definition and control
Applications	Large Scale Electricity Plant, High End Space	•Si solar cells (dominant currently)	•Future applications (2nd,3rd generation solar cells)

Figure 1.1 Three major categories of light trapping in solar cells

To increase light absorption in solar cells, there are three major categories in terms of length scale as summarized in Figure 1.1. The first category as shown in the left panel is to utilize large optical lens and/or mirrors to concentrate solar radiation from large area onto smaller solar cells area. Based on this method, high performance a few thousands of concentrated sun intensity can be generated onto concentrating photovoltaic (CPV) solar cells. The efficiency can easily exceed 25-35%. CPV has been widely developed by many solar cell companies such as Sunpower, Amonix, Spectrolab and Sharp. However CPV system, including optics system, tracking system and cooling system, is very complicated and bulky. It is not suit for small load and recent building integrated photovoltaics (BIPV). It is only feasible for utility scale power plant installed at isolated areas[9, 10].

The second category is surface texturing at micro-scale, as shown in the middle panel of Figure 1.1. Reflection is reduced and absorption is increased by 2nd chance strike on the

textured surface. There are quite a few techniques proposed to texture including isotexturing[11], reactive ion etching (RIE)[12], mechanical scribing[13], masked isotropic etching[14] and acid etching[15]. But they are only used in polycrystalline silicon (p-Si) or amorphous silicon (a-Si) under costly process. Laser ablation can be used for both p-Si and single crystalline silicon (c-Si), but involves too many steps (lasing, alkaline etching and acid etching) to perform economically[16]. Potassium hydroxide (KOH) based alkaline etching is the only cost-effective solution for texturing on (100) surface of single crystal Silicon(c-Si). The pyramid shaped texture is formed and reflection is reduced effectively[17]. KOH solution etching still works as a standard process step for commercial c-Si solar cells[9]. However, it is hard replanted to p-Si and non-Si solar cells because of unreliable anisotropic etching.

The third category is based on nanotechnology as shown in the right panel of Figure 1.1. The typical feature size of moth-eye or other diffusive shape is typically much smaller than 1 μ m. Plasma reactive ion etching (RIE) or wet etching is always involved to make such features[18, 19]. Other nanoscale configurations, such as quantum dot[20] / well[21], nanorod[22] / nanowire[23] etc, also attract considerable attentions for light trapping. Unlike previous two approaches, nanoscale structure is still under laboratory phase because of high manufacturing cost.

1.1.2 Infrared Photodetectors (IRPD)

High spectrally selective Infrared photodetectors has various applications in military target detection/identification, foliage and camouflage detection, multi-spectral classification of dissimilar materials, IR gas sensing and absorption spectroscopy[7, 24]. As summarized in Table 1.1, up to now, infrared photodetectors are based on HgCdTe (MCT) since 1960's[5, 8]. Because of a dramatic change of the band gap as a function of material composition, it is very challenging to reproducibly obtain large array uniformity.

Table 1.1 Current infrared photodetectors status and challenges

	Pros	Cons	Status	Challenges
HgCdTe (MCT)	<ul style="list-style-type: none"> ▪ Easy bandgap tailoring ▪ Well developed theory ▪ Multicolor 	<ul style="list-style-type: none"> ▪ Non-uniformity over large area ▪ High cost growth and processing ▪ Surface instability 	<ul style="list-style-type: none"> ▪ Covers: MWIR,LWIR,FIR ▪ Responsivity: A/W range ▪ Detectivity: 10^{12} cmHz^{1/2}/W ▪ T: <80K or ~200K for MWIR 	<ul style="list-style-type: none"> ▪ Material growth and fabrication ▪ Large array uniformity ▪ High operation temperature
QWIPs Type I	<ul style="list-style-type: none"> ▪ Mature III-V technology ▪ Good uniformity over large area ▪ Multicolor 	<ul style="list-style-type: none"> ▪ High thermal generation ▪ Complicated design (non-normal incidence) 	<ul style="list-style-type: none"> ▪ Covers MWIR,LWIR,FIR ▪ Responsivity: A/W range ▪ Detectivity: 10^{11} cmHz^{1/2}/W ▪ T: <40-80K 	<ul style="list-style-type: none"> ▪ Size and wavelength independent coupling scheme ▪ High operation temperatures
QWIPs Type II Antimonide Supperlattices	<ul style="list-style-type: none"> ▪ Higher operation temperature ▪ Low Auger recombination ▪ Easy wavelength control 	<ul style="list-style-type: none"> ▪ Complicated design ▪ Sensitive to interface 	<ul style="list-style-type: none"> ▪ Covers MWIR,LWIR,FIR ▪ Uncooled operation at LWIR with $D=10^9$ cmHz^{1/2}/W 	<ul style="list-style-type: none"> ▪ Growth technique and passivations
QDIPs	<ul style="list-style-type: none"> ▪ Normal incident absorption ▪ Low thermal generation 	<ul style="list-style-type: none"> ▪ Complicated design ▪ QD non-uniformity 	<ul style="list-style-type: none"> ▪ Covers MWIR,LWIR,FIR ▪ Responsivity: 2.5A/W ▪ Detectivity: 10^{11} cmHz^{1/2}/W ▪ T: >100K(RT) 	<ul style="list-style-type: none"> ▪ QD uniformity ▪ Absorption efficiency ▪ Dark Current reduction

Mature materials growth technologies for III–V semiconductors such as AlGaAs/GaAs and InGaAs/GaAs make quantum well infrared photodetector (QWIPs) as a new promising candidate[6, 8]. QWIPs can provide good spatial uniformity and detect multicolor lights by employing the intersubband and the subband to-continuum transitions in quantum wells. The main drawback of this type of QWIPs is that they can not identify normal incident light due to restriction of selection rules for the optical transition. Additional Light coupling or other new technology is required for QWIPs[24, 25].

To conquer this limitation improved QWIP structures, like InAs/Ga_{1-x}In_xSb (x from 0 to 1) strained layer superlattices (SLSs) on GaSb substrate, has been presented[26]. In the case of SLS structures, the absorption becomes strong for normal incidence of light. Consequently, the SLS structures provide high responsivity, as already reached with HgCdTe, without any need for gratings. But the growth technique and passivations are still challenges for SLSs[8].

Alternative solution is quantum dot infrared photodetectors (QDIPs). The representative device heterostructures comprises repeated InAs QD layers buried between GaAs barriers with top and bottom contact layers at active region boundaries. QDIPs offer many theoretical advantages over QWIPs including normal incidence detection due to the geometry with the carrier confinement in all three directions, reduced thermal generation of electrons due to three dimension the energy quantization and lower dark current due to three dimensional quantum confinement of the electron wavefunction[8, 27]. But in fact, there are still some challenges need to overcome such as uniform distribution and size quantum dots and thick active layer without misfit dislocations.

1.1.3 Enhanced infrared absorption in Photonic Crystals

Photonic Crystals (PC) exhibits photonic band gaps (PBGs) and unconventional dispersion and refractive properties making it great candidate for potential photodetector applications[24, 28, 29]. PC structures can lead to absorption property alteration, through the photonic density of states (DOS) engineering. Enhanced absorption can happen near or at the

band edge where the electromagnetic Bloch wave is still extended throughout the structure, its group velocity is near zero, and the photonic DOS is greatly increased[30, 31]. Enhancement and suppression of thermal emission and absorption reported so far are mostly based on bandedge effect in various metallic PC structures or clusters. On the other hand, the DOS at defect level within PBG is also significantly increased, more than 95% absorption can be achieved in one dimensional (1D) PC[32].

Simultaneous inhibition and redistribution of spontaneous emission in PC has been demonstrated theoretically and experimentally[33]. However, most of presented work focused on 2D dielectric photonic crystal slab (PCS) involved light emission. Only a few work demonstrate the modified absorption characteristics in 2D PCS cavities[24]. The introduction of an absorptive layer in a dielectric PCS structure (e.g. quantum well, quantum dots) can lead to the modification of the absorption characteristics, due to the spectrally-selective light-matter interaction in the cavity. Photonic crystal based quantum dots or quantum well infrared photodetector (PCIP) can work at high temperature due to low dark current compared with traditional QDIP or QWIP.

Recently, great attention has been paid to guided resonances, a class of “leaky” modes in PCS. These guided resonances are standing electromagnetic waves that are guided with the electric field distribution confined within PCS, but are also strongly coupled to out-of-the-plane radiation modes due to phase matching provided by the periodic lattice structure. The interaction between the discrete guided resonances and the continuum incident radiation manifests itself in the form of very sharp peaks or dips in the transmission spectrum, called Fano resonances[34, 35], or guided mode resonance (GMR) in 1D grating structures[36, 37]. Unlike PCS structures with a complete photonic bandgap, the effects of guided resonance phenomena do not require exceptionally high index contrast. The substrate index requirement is also substantially relaxed[38]. This Fano resonance effect has been investigated, both

theoretically and experimentally, in photonic crystal structures for many photonic devices. It could be a good solution to high performance infrared photodetectors[39, 40].

1.2 Overview of Dissertation

Chapter 2 first introduces background of anti-reflection (AR) coatings and discusses the advantages and disadvantages of current coating approaches. Then our omni-directional anti-reflection (Omni-AR) coating approach is presented. Based on Rigorous Coupled Wave Analysis (RCWA), more details on Omni-AR structures are analyzed and compared to other type of AR structures. Finally Omni-AR on different material systems and Omni-AR integrated commercial solar cell are discussed. Omni-AR coatings can reduce reflection with large angle ($> 60^\circ$ incident angle) and wide spectrum ($> 800\text{nm}$ on Si). The experimental efficiency of solar cell with Omni-AR is increased.

Chapter 3-6 proposes absorption enhancements in different types of photonic crystals based infrared photodetectors structures. The advantages of photonic crystals are attempted to incorporate with the superiority from quantum dots infrared photodetectors to realize multicolor, high spectral selectivity and high operation temperature photonic crystal quantum dots infrared photodetectors (PC+QDIPs).

Chapter 3 presents absorption enhancement in 1D PC based on transfer matrix method (TMM). The absorption enhancement from bandedge effect is simulated. Then absorption of defect cavity and resonance cavity is discussed.

Chapter 4 presents 2D absorptive PCS simulation. First describes simulation setup under 3D finite difference time domain (FDTD) environment. Secondly, absorption with in-plane light source is demonstrated for both defect cavity and defect free cavity. The last part switches to absorption with vertical light source.

Chapter 5 covers infrared absorption in Fano filters. First introduces Fano filter design and fabrication. Secondly, transmission properties are discussed and correlated to dispersion charts. Lastly, the absorption of colloidal quantum dots (CQDs) in Fano filter is dug out.

Chapter 6 further investigates absorption enhancement for two possible Fano filter based infrared photodetectors.

Chapter 7 summarizes this dissertation work and suggests for future work on solar cells and infrared photodetectors

CHAPTER 2

OMNI-DIRECTIONAL ANTI-REFLECTION (OMNI-AR) COATINGS FOR SOLAR CELLS

2.1 Background on AR Coatings

When light strikes at the front surface of solar cells, two major optical losses will emerge. The first loss comes from the shading of top metal contacts which amounts to 8-10% solar cells efficiency reduction. Shading loss can be reduced via many improved technologies such as shaped fingers, prismatic covers, or cavities[9]. Back contact solar cells are able to completely restrain shading loss by moving top contacts to the back side of solar cells[41]. Another more crucial optical loss stems from the reflection at the solar cells surface. For example, the bare silicon (Si) loses more than 30% incident light in the air due to its high refractive index. To prevent reflection loss, anti-reflection (AR) coatings are always used in solar cells. An ideal AR structure should lead to zero reflection loss on solar cell surfaces over an extended solar spectral range for all angles of incidence. Such a coating can eliminate the need for a mechanical tracking device for proper optical alignment of the solar cell with respect to incident sunlight[9]. The perfect omni-directional AR (Omni-AR) structure has been a subject of intensive research in solar cells as well as other thin film optics. A series of papers were published by Dobrowolski and Poitras et al. in search for the perfect AR structure[42, 43]. In this section, several prevalent AR technologies are introduced and discussed.

2.1.1. Planar Thin Film AR Coatings

Considering non-polarized sunlight for solar cells, the reflection at two media interface is given by the equation 2.1[44]

$$R = 1/2 * \left\{ \left(\frac{\sin(\theta_2 - \theta_1)}{\sin(\theta_2 + \theta_1)} \right)^2 + \left(\frac{\tan(\theta_2 - \theta_1)}{\tan(\theta_2 + \theta_1)} \right)^2 \right\} \quad (2.1)$$

Where θ_1 is the incident angle from superstrate with refractive index n_1 and θ_2 is the refractive angle in the substrate with refractive index n_2 . The relationship between θ_1 , θ_2 , n_1 and n_2 is given by Snell's law

$$n_1 \sin \theta_1 = n_2 \sin \theta_2 \quad (2.2)$$

According to this theory, a single layer can be used as AR coating if the refractive indices condition, $n_1^2 = n_0 n_s$, is satisfied, where n_0 , n_1 and n_s are the indices of superstrate, single layer and substrate, respectively. The zero reflection wavelength location, λ , can be engineered by the quarter wavelength thickness, $d = \lambda / (4n_1)$, of that single AR layer. In practice, 75nm SiN_x ($n=2.0$) or 100nm SiO₂ ($n=1.44$) thin film aimed at 600nm is often used in Si solar cells as an effective AR and passivation layer. Similarly, for multi-layer ARC, the idea indices for the double layer and triple layer ARC are $(n_2/n_1)^2 = n_s/n_0$ and $(n_1 n_3 / n_2)^2 = n_0 n_s$, respectively[44].

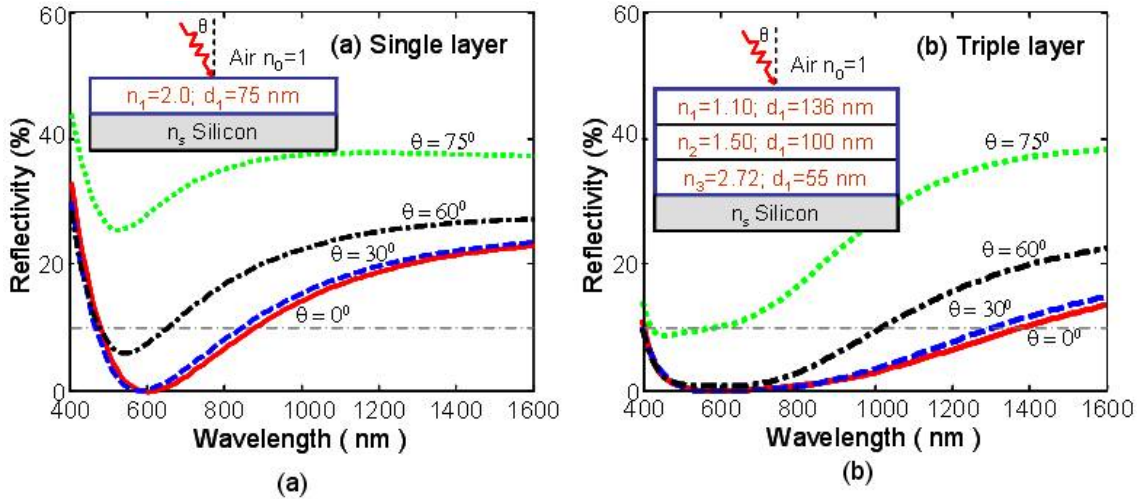


Figure 2.1 Simulated quarter wavelength planar thin film AR structures with ideal indices and thicknesses for (a) single and (b) triple layers.

As expected, for the single layer AR structure, close to zero reflection can be achieved only at the target wavelength with normal incident direction as shown in Figure 2.1(a). By increasing the number of layers shown in Figure 2.1(b), it is possible to achieve relatively wider spectral coverage with close to zero reflection in a reasonably wide range of incident angles (up to 60°). Very low refractive index is imperative ($n=1.1-1.3$) in the multilayer AR structures.

However most transparent materials has high refractive index, like SiO ($n = 1.8-1.9$), SiO₂ ($n = 1.44$), Si₃N₄ ($n = 1.9$), TiO₂ ($n = 2.3$), Al₂O₃ ($n = 1.86$), Ta₂O₅ ($n = 2.26$), SiO₂-TiO₂ ($n = 1.8-1.96$), make them hard to apply for multilayer AR coatings. MgF₂($n = 1.3-1.4$) combined with ZnS ($n = 2.33$) or ZeO₂ ($n = 2.3-2.4$) are two of few matched double AR structures to Si solar cell[45, 46]. Precise control of multi layer thickness is another challenge.

2.1.2 Graded Index AR Coatings

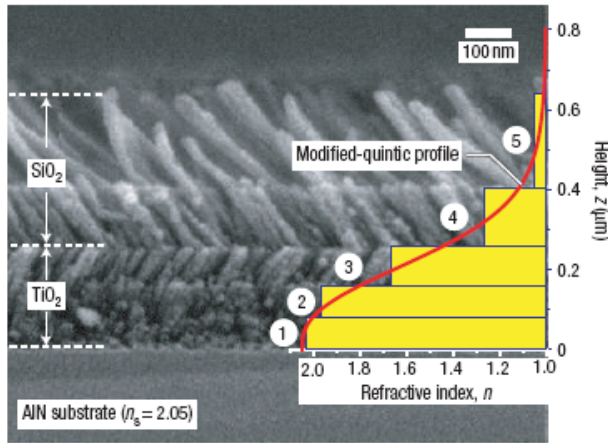


Figure 2.2 Low GRIN AR structure by physical vapor deposition[47]

The second group is the graded index (GRIN) AR structures[48], where the refractive index of the structure changes gradually from the superstrate to the substrate[49, 50]. The index profile can follow different mathematical functions, such as linear, cubic or quintic. With a GRIN AR structure, extremely low reflection can be achieved over a broad spectral range for a wide range of incident angles, especially with the quintic index profile[48]. The difficulty associated with the choice of materials for practical control of index profiles has prevented this structure from practical applications. Sol-gel based approaches with either porosity control and/or high index doping introduction were reported[51-53]. As shown in Figure 2.2, a SiO₂/TiO₂ GRIN AR coating was reported by Xi *et al.*, by oblique-angle physical vapor deposition, where the refractive index can vary from 1.0 to 2.0[47].

2.1.3 Moth – Eye AR Coatings

Moth eye AR coatings have same effective graded index profile from superstrate to substrate on single material typically by pattern transfer and plasma Reactive Ion Etching (RIE)[18, 19]. The size, shape and density of moth eye can be well controlled by RIE recipe as shown in Figure 2.3. The high cost process associated with RIE prevents it from mass promotions. Another technique, soft roller nanoimprint[54], is recently proposed to generate subwavelength moth eye on Si. The feature of moth eye is determined by the master module. Low reflection (<12%) is achieved with up to 60° incident angle.

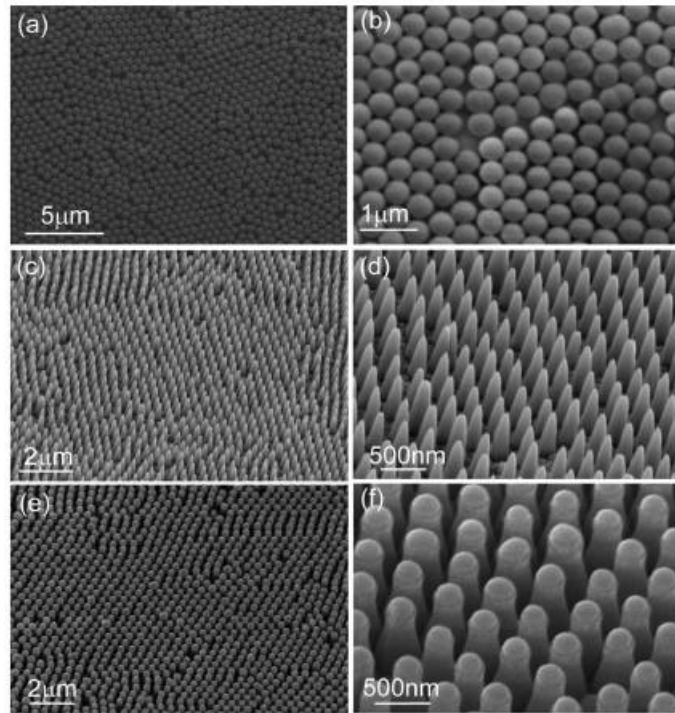


Figure 2.3 Various nanostructures by RIE[18]

2.1.4 Textured Surface AR Coatings

The fourth group is the textured surface AR structures. Potassium hydroxide (KOH) etching on c-Si (100) surface is the only successful paragon. The anisotropic etching results from intrinsic anisotropic etching rate of c-Si. Pyramid microstructure with 54.74° apex angle is formed as shown in Figure 2.4. Reflected light from one pyramid is able to strike on another

pyramid instead of escaping. It has led to record solar cell efficiencies in the lab and has been the standard AR structure on all commercial single crystal Si solar cells[17, 49, 50]. Close to zero reflection over a wide spectral range can be achieved when an additional layer of low index film (e.g. SiN_x) is coated on these microscale pyramidal structures on Si surface. However, the microscale surface texture involves anisotropic etching of the Si substrate, which does not apply to poly-crystal Si and non-Si solar cells. In this case, anisotropic etching becomes too unreliable and photolithography-defined surface textures too expensive. A cost-effective and materials independent method for surface texturing is needed.

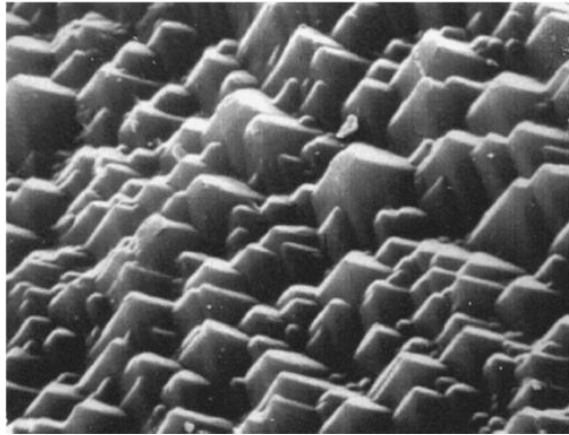


Figure 2.4 Pyramid microstructure created by KOH wet etching[17]

2.2 Optical Design of Omni-AR Coatings

This section presents a new Omni-AR coatings design for microscale surface texturing. The process is solution based, which is compatible with large scale manufacturing and flexible for integration on various solar cell substrates[55, 56]. It is inherently low-cost and energy efficient, without complicated large vacuum systems. A detailed theoretical investigation has been carried out to understand the optical performance of the microscale surface textures for AR applications. Omni-AR structures is compared to pyramidal and conical structures. The impact of refractive index, feature size and density is also reported. Some typical microstructure performance are summarized in terms of daily photons and current generation.

2.2.1 Simulation Method and Theory

The simulation is based on rigorous coupled-wave analysis (RCWA)[57-59], which analyzes the diffraction of an electromagnetic plane wave incident on a grating structure composed of materials with different indices. The fields inside all the layers are expanded in a sum of spatial harmonics, i.e. Fourier expansion. This expansion can be expressed and solved as an eigenvalue problem for all of the harmonic orders. For each order of the field components, the wave undergoes simultaneously forward and backward diffraction in a predefined periodic structure with different indices as shown in Figure 2.5. By solving the coupled wave equations for both transmitted and reflected waves, the fundamental and higher order forward and backward wave diffraction efficiencies are determined. The final solution to the electric field will be the sum of a series of Fourier components based on the solutions from the above coupled wave equations. Both total transmission and reflection waves can finally be computed[60, 61].

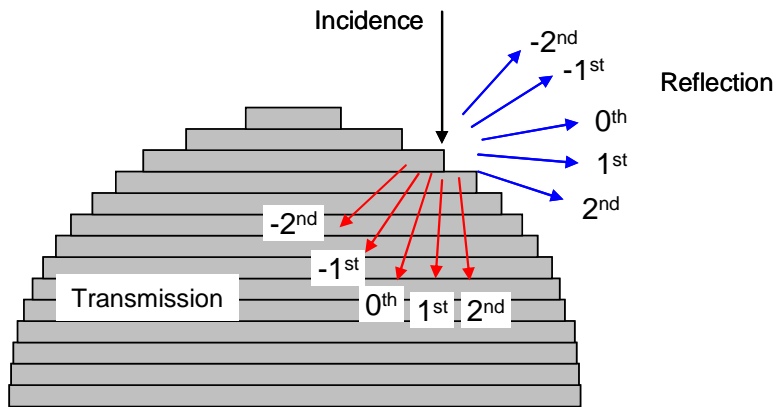


Figure 2.5 Cartoon of RCWA based simulation for hemisphere microstructure

All the simulations done here include both transverse-electric (TE) and transverse-magnetic (TM) polarizations. Since we are mostly concerned with sunlight, which is non-polarized, all the reflection results are a simple average of reflection calculated from both TE and TM polarized incident waves. Note the calculation counts for both specular (zero order) component, as well as the diffusive (higher order) component, as the total reflected/transmitted

power. This also agrees well with our experimental setup, where integrating sphere is used for the total reflection/transmission measurement.

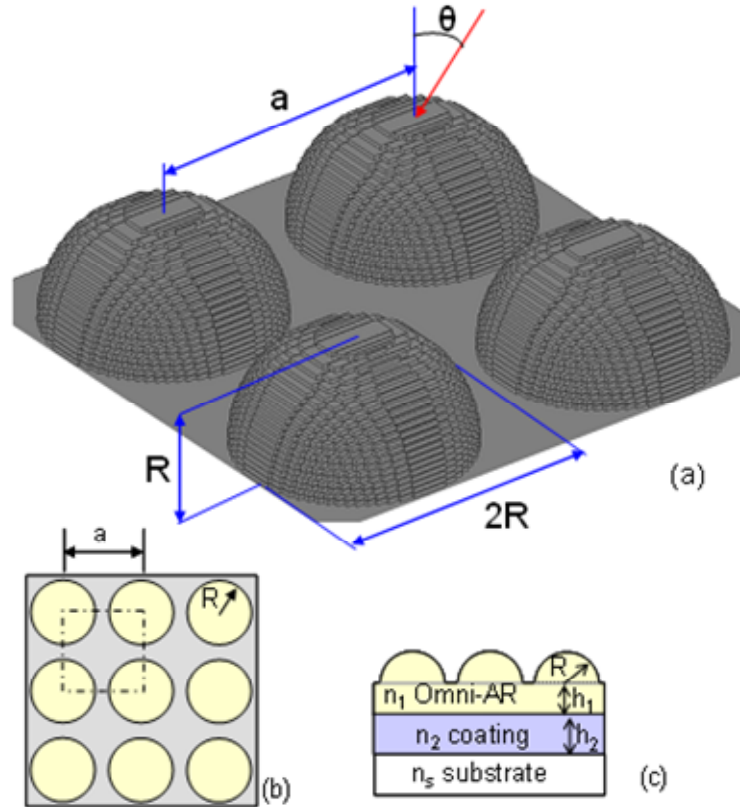


Figure 2.6 Hemispherical grating as the basic anti-reflection structure for simulation: (a) Three-dimensional view of the square lattice; (b) top view and (c) cross-sectional view of the basic structure

The geometrical structure under consideration is depicted in Figure 2.6. A square lattice of hemispheres is constructed on an optional dielectric film, which sits on a substrate. The hemispherical Omni-AR structure, optional dielectric film and substrate may have the same or different refractive indices n_1 , n_2 and n_s , respectively. The structural parameters, as shown in the top view and cross-sectional view of the Omni-AR structure in Figure 2.6, are variables in our simulations to investigate their impact on reflection.

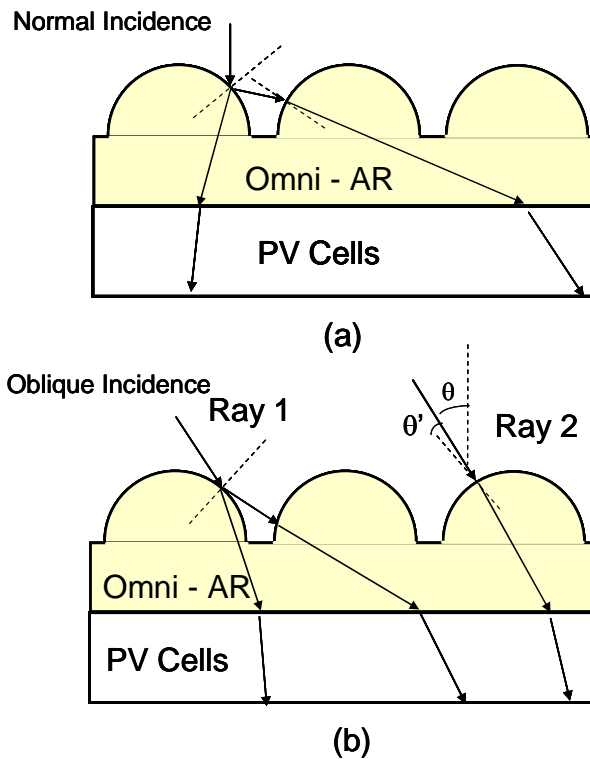


Figure 2.7 Light trapping in Omni-AR microstructure (a) under normal incident light (b) under oblique incident light

Figure 2.7 shows the light trapping of Omni-AR structures. Under normal incidence in Figure 2.7(a), The light ray strikes on one hemisphere surface is reflected back onto another hemisphere. Reflection is reduced by 2nd chance strike and absorption is increased accordingly. Due to extended optical path length (OPL), the absorption can be further increased which is more critical for thin film solar cells which has very thin (<2 μm) active layer[62]. As incident angle increased, the Omni-AR structure obtains even better performance. As shown in Figure 2.7(b), on half part of hemisphere, the light (Ray 1 as shown in Figure 2.7(b)) strikes twice similar as normal incident case. While on the other part of hemisphere, the reflection of light (Ray 2 as shown in Figure 2.7(b)) is reduced because the real incident angle (θ') forming at the interface is much smaller than incident angle (θ) formed on the planar surface. In addition, the OPL in this case also increased compared to planar structure case. So, the light trapping in hemisphere is very effective and suitable for high performance ARC applications.

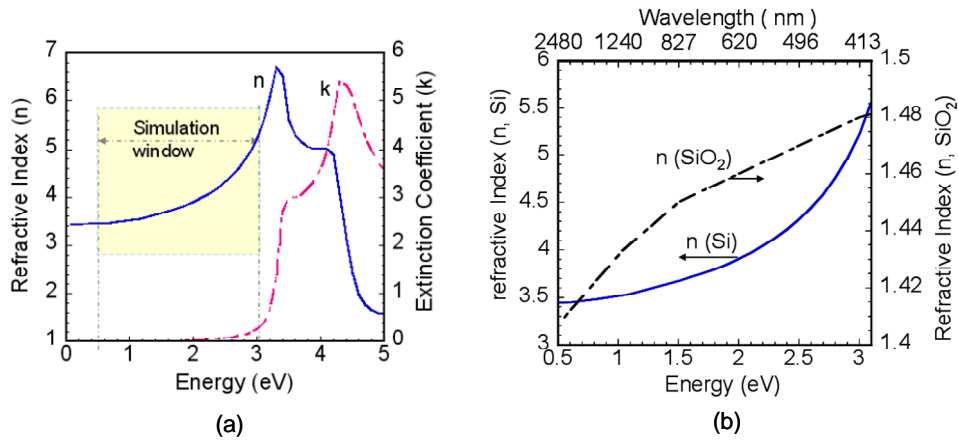


Figure 2.8 Crystal silicon complex index dispersion curve $n = n + ik$ from ultraviolet to infrared and (b) refractive index dispersion curve of silicon and silicon dioxide used in our simulation

Although the substrate material under investigation is Si (1.12 eV of bandgap) in most cases, the Omni-AR structure proposed here can be also applied to other substrate materials with different optical properties. For this reason, spectra of most investigated cases in this work are extended to 1600nm which can cover most of small bandgap solar cell materials like Germanium (Ge, 0.7eV of bandgap). In some cases quartz substrates are used in order to be able to measure the total transmission over the visible spectral region. Shown in Figure 2.8(a) are the dispersion curves for the refractive index and extinction coefficient for Si used in our simulations. The complex index is expressed as $\mathbf{n} = n + ik$, where n and k are the real and imaginary part of the refractive index, respectively. The imaginary part k , i.e. the extinction coefficient, is related to the absorption coefficient α , with $\alpha = 4\pi k/\lambda$, where λ is the free-space wavelength. Note the refractive index of Si changes with the wavelength over the spectral region of interest. The primary focus of our work is on light propagation through an Omni-AR structure on a Si substrate, where the Omni-AR structure has no or little absorption. The refractive index profiles for Si and silicon dioxide (SiO₂) used in our simulation in the wavelength region of interest is shown in Figure 2.8 (b).

2.2.2 Hemispherical Surface and Omni-AR Structures

Hemispherical structures with different structural parameters are firstly considered. In what follows, assuming the substrate material is Si, and the coating material is SiO₂, with a refractive index dispersion curve shown in Figure 2.8(b) ($n_{\text{SiO}_2} \sim 1.45$). Starting with a simple case in Figure 2.9 (a), where a hemispherical structure is coated on a Si substrate, with the hemispherical radius $R = 1\mu\text{m}$ and lattice spacing $a = 2.5\mu\text{m}$. The reflection is reduced by $\sim 50\%$ for incident angles up to 60° over the entire spectral region of simulation, as compared to the reflection for a bare Si substrate at surface normal incident conditions. The reflection for incident angle of 75° is also reduced in the shorter wavelength regime. The result is encouraging, as it proves the incident angle independence, thus *omni-directional*, of the hemispherical structure investigated here.

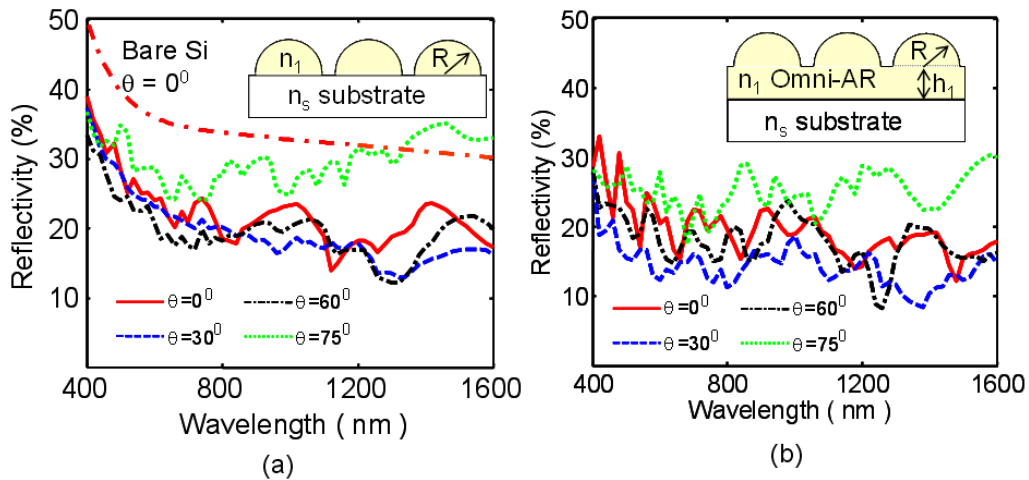


Figure 2.9 Simulation results for hemispherical structures with index $n_1 = 1.5$ on silicon substrate: (a) Square lattice hemispherical structure with radius $R = 1\mu\text{m}$ and lattice constant $a = 2.5\mu\text{m}$ and (b) Omni-AR structure with hemispherical structure on top of a thin film with the same index n_1 and thickness $h_1 = R = 1\mu\text{m}$.

It is worth pointing out here that the hemispherical structure considered here is not ideally closely-packed, which leads to slightly under-estimated results as compared to ideally close-packed structure (with $a = 2R$), especially at surface-normal or small incident angle directions. This will be discussed later on the packing density impact section. The parameters

chosen here have little impact on the reflection as compared to the ideal close packed case. The parameters chosen in the simulation are better representation of the actual experimental conditions, where spherical particles may not be closely packed together to form a mono-layer in a large area domain.

The low index film between substrate and hemispherical structure, as shown in Figure 2.9(b), is inherently present in the structure which will be discussed in the Omni-AR experiment section. The impact of such thin film (h_1) on reflection is investigated, as shown in Figure 2.9(b) for different incident angles. Compared to Figure 2.9(a), insignificant changes in reflection are observed. The oscillations in Figure 2.9 are due to interferences at different interface.

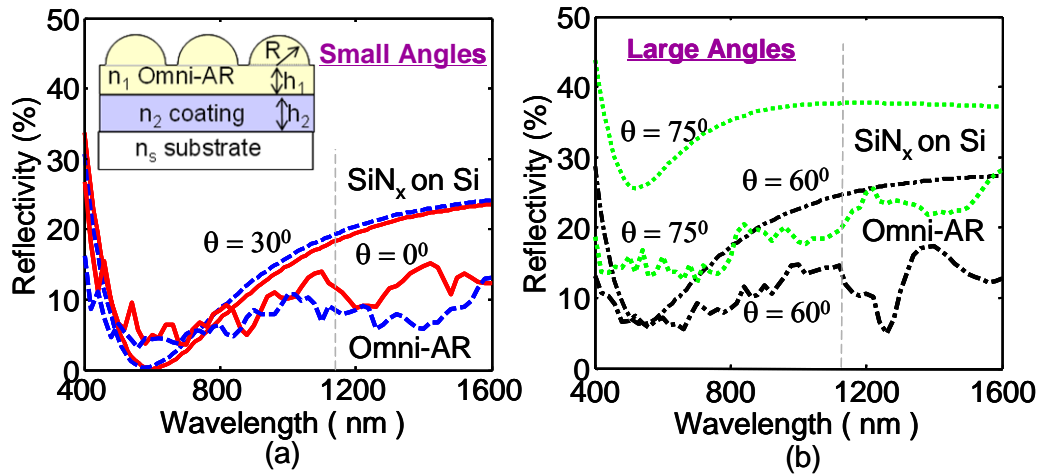


Figure 2.10 (a) Simulation results for Omni-AR structure on Si substrate with a SiNx thin film in between ($n_2 = 2.0$ and $h_2 = 75$ nm); Other simulation parameters are the same as those in Figure 2.5(b). The reflectivity for (b) small incident angles ($\theta = 0^\circ$ and 30°) and large incident angles ($\theta = 60^\circ$ and 75°), for two cases: SiNx coated Si and Omni-AR on SiNx coated Si.

Another scenario is further considered where the Omni-AR structure is an add-on to current Si solar cells, where 75nm SiNx single layer is coated on top of the solar cells. SiNx plays as a passivation role of high index contrast between Si and SiO_2 . The results are shown in Figure 2.10. Compared with previous structures shown in Figure 2.9, significantly reduced reflection is achieved over a wide spectral range for incident angles from 0° to 60° . A comparison is given in Figure 2.10(a) and (b) for SiNx coated Si substrates with and without

Omni-AR coatings. The improvement in reflection is relatively small for small incident angles of 0° and 30° (Figure 2.10(a)). However, significant improvement in reflection can be achieved for large incident angles of 60° and 75° (Figure 2.10(b)). This is the most attractive feature of the Omni-AR structure, which provides angle independent reflection over a wide spectral range.

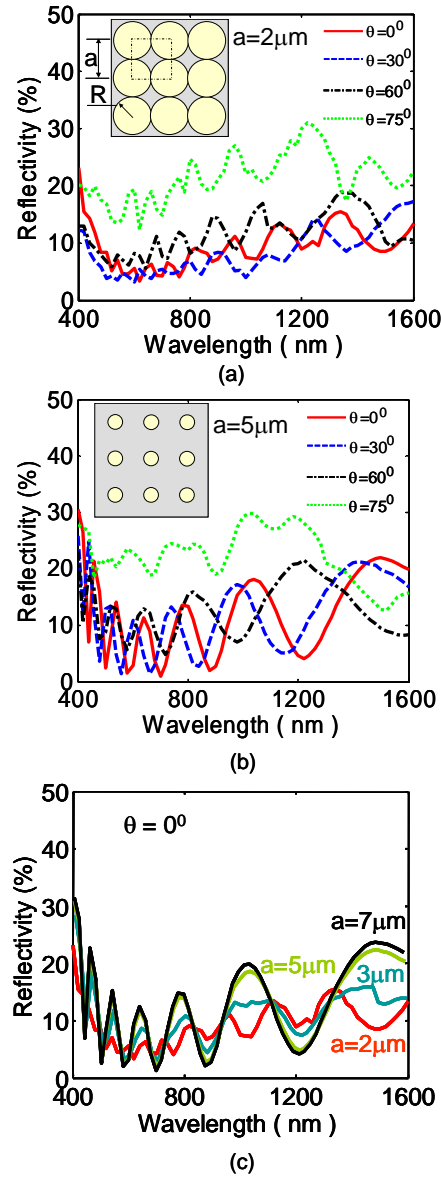


Figure 2.11 Packing density impact for the proposed hemispherical Omni-AR structure similar to the one in Figure 2.10 (a) with $R = 1\mu\text{m}$, $n_1 = 1.5$ and lattice constant (a) $a = 2\mu\text{m}$ and (b) $a = 5\mu\text{m}$. (c) Surface normal reflectivity for different packing densities

The impact of packing density and particle size was investigated as well. Shown in Figure 2.11 is the simulated reflection with different packing densities. With fixed radius $R = 1\mu\text{m}$, the packing density can be varied by changing the lattice constant a . Shown in Figure 2.11(a) and (b) are two examples with $a = 2\mu\text{m}$ and $a = 5\mu\text{m}$, respectively. The surface normal reflection for different packing densities is shown in Figure 2.11(c). It is worth noting that the simulated reflection does not change significantly over a relatively large range of packing densities. The only notable feature is the increased oscillation for smaller packing densities. This could mainly be due to the dominance of the interferences in the layer under the particle (h_1) layer as shown in the inset of Figure 2.11(a)), as the exposed flat surface area increases with the reduction of packing density.

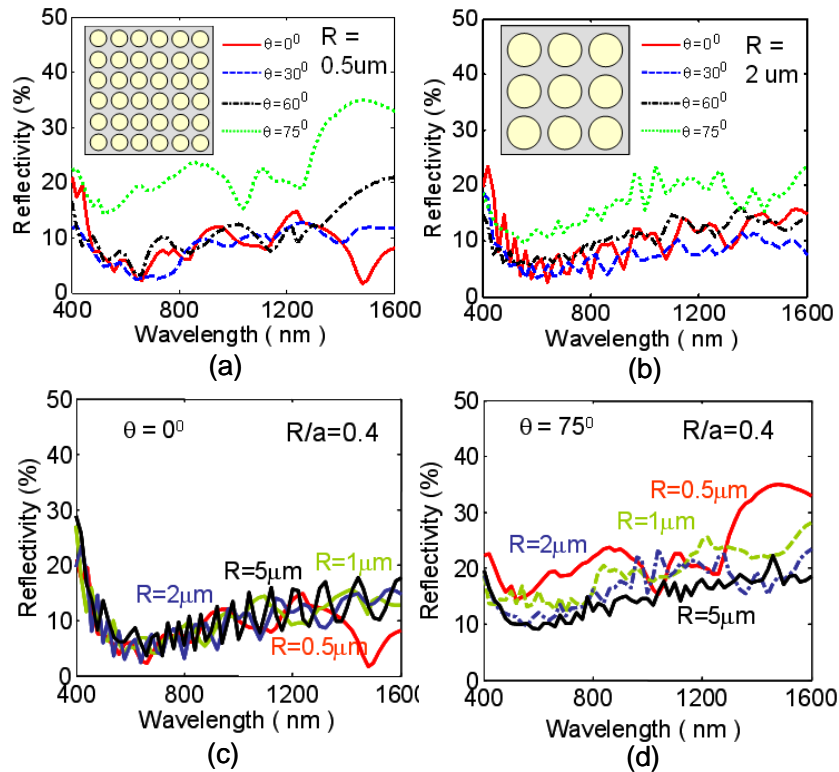


Figure 2.12 Spherical radius impact for the proposed hemispherical Omni-AR structure similar to the one in Figure 2.10 (a) with $R/a = 0.4$, $n_1 = 1.5$ and spherical radius (a) $R = 0.5\mu\text{m}$ and (b) $R = 2\mu\text{m}$. (c) Surface normal reflectivity and (d) large incident angle reflectivity for different spherical radius

Figure 2.12 shows the simulated reflection for different particle sizes. Here the packing fraction is fixed, i.e., the ratio between radius R and lattice constant a is fixed at 0.4. Shown in Figure 2.12(a) and (b) are two examples with $R = 0.5\mu\text{m}$ and $R = 2\mu\text{m}$, respectively. The surface normal reflection and large incident angle reflection ($\theta = 75^\circ$) for different particle size is shown in Figure 2.12(c) and (d), respectively. Again, no significant difference in the simulated reflection is found, especially at small incident angles up to 60° . These results suggest large process windows in manufacturing the proposed structure for solar cell applications. However, for larger incident angle ($\theta = 75^\circ$), we see slightly reduced reflection with the increase of the particle size, which is due to the thicker transition layer at large incident angles. In all simulations shown in Figure 2.12, the thickness of h_1 layer ($1\mu\text{m}$) as shown in the inset of Figure 2.10(a) and the packing fraction (proportional to the ratio of $R/a = 0.4$), are kept the same. The fixed packing fraction for non-close-packed structure can lead to the actual open flat areas between the hemispheres to be increased with the increase of the particle sizes, which may be the cause of the more profound interference oscillation features observed for larger particles.

2.2.3 Pyramidal, Conical, versus Hemispherical Structures

Surface structures of different shapes were also investigated. Shown in Figure 2.13 are the structures and simulation results for three different shapes: (a) pyramids, (b) cones and (c) hemispheres. All the structures under simulation have similar structural parameters. The structure material is SiO_2 and the substrate is Si. The parameters for both loose packed case and close packed case are listed in Table 2.1.

Table 2.1 Parameters of pyramid, cone and hemisphere shaped microstructures

Microstructures	Parameters	Comments
Pyramid Shaped	Base: $2\mu\text{m} \times 2\mu\text{m}$ Height: $1\mu\text{m}$	$a=2.5\mu\text{m}$ (loose packed) $a=2\mu\text{m}$ (close packed) $n_1=1.45$ $h_1=1\mu\text{m}$
Cone Shaped	Base Radius: $1\mu\text{m}$ Height: $1\mu\text{m}$	
Hemisphere Shaped	Base Radius: $1\mu\text{m}$ Height: $1\mu\text{m}$	

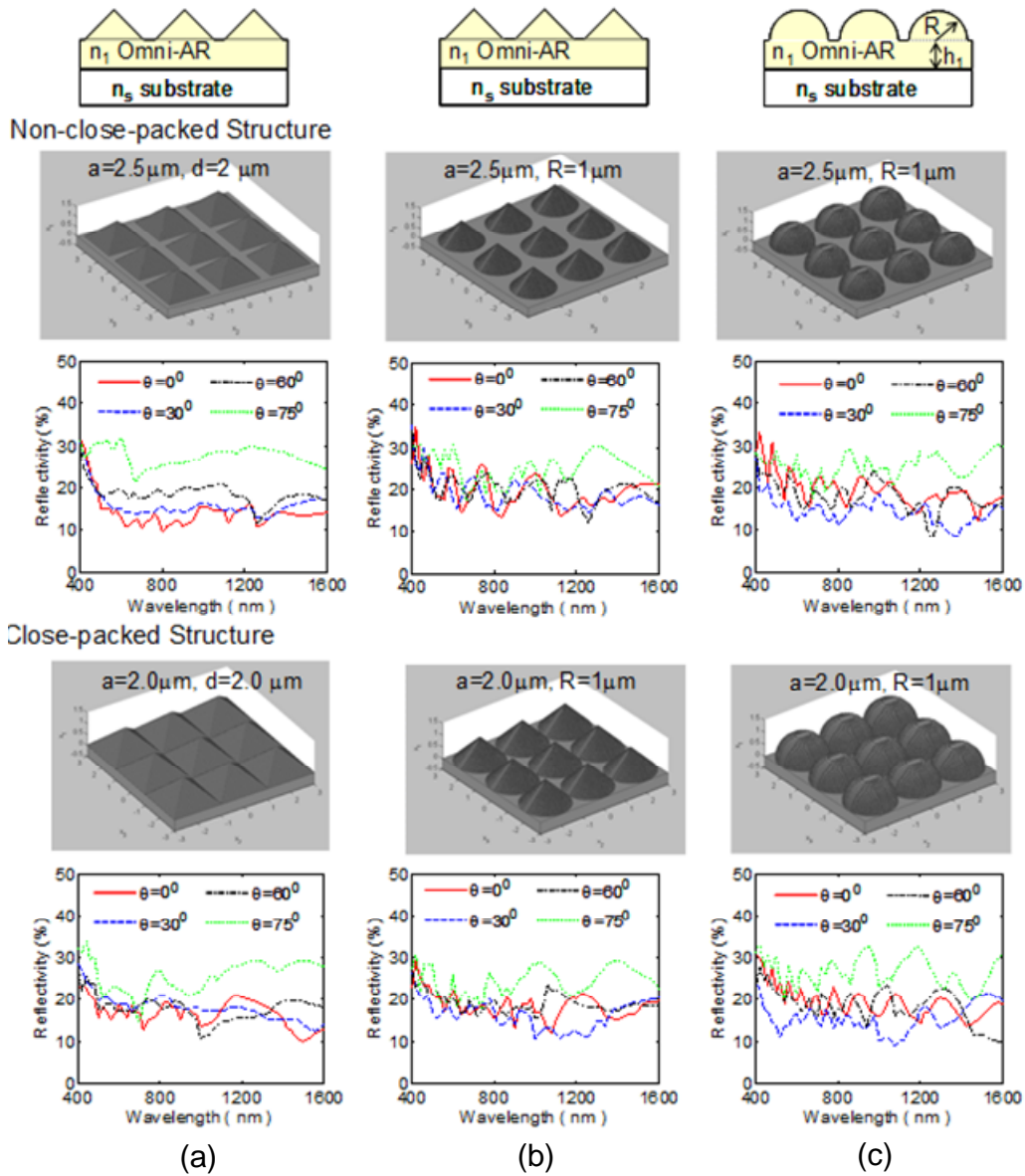


Figure 2.13 The structures and simulation results for three differently shaped structures: (a) pyramids, (b) cones and (c) hemispheres. Both non-close-packed structures and close-packed structures are simulated for comparison

As shown in Figure 2.13, the hemispherical structure has slightly better performance overall, especially at large incident angles, while the pyramid structure has slightly better performance at small incident angles and at shorter wavelength regime. This could be due to the enhanced second strike effect for pyramid structure at small incident angles, as compared

to the case for hemispherical structures. We can also argue that the packing density impact here is very small on the total reflection for all three different shapes for the two cases presented here. This further validates the discussions based on the results of density impact, which indicates the process flexibility and relatively large process tolerance windows for large area Omni-AR structure formation

2.2.4 Index Matching to Si Substrate

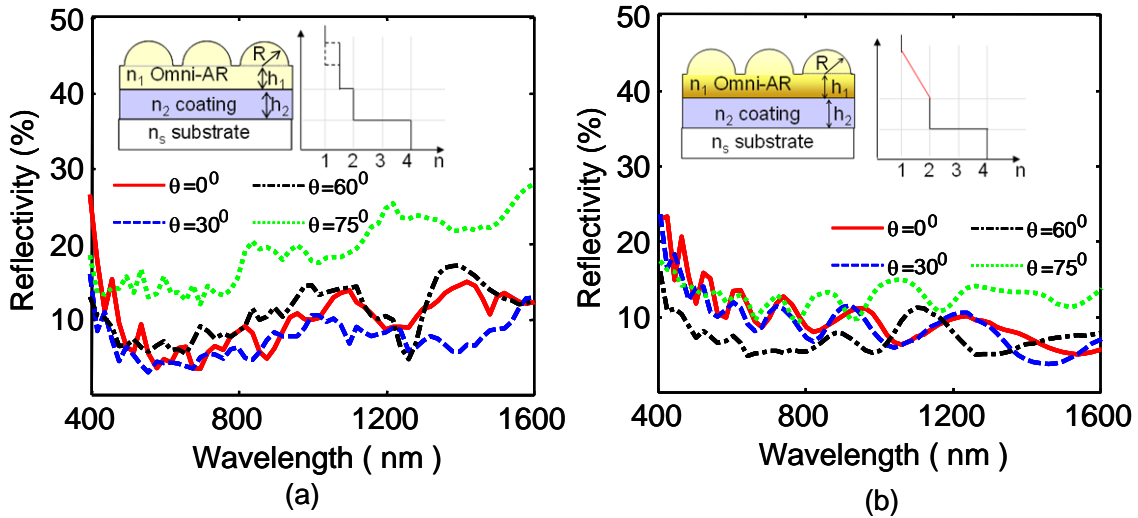


Figure 2.14 Reflectivity simulation results for index matching of silica Omni-AR to Si substrate: (a) SiNx film with a fixed index of 2.0 and (b) graded index film with index varying linearly from Omni-AR ($n = 1.5$) to substrate ($n = 4.0$)

The hemispherical structure in the proposed Omni-AR offers spectrally and directionally-independent reflection. Further reduction in reflection can be provided with index matching of the Omni-AR structure to substrates with different indices. Different graded index (GRIN) schemes are investigated. The standard SiO₂ Omni-AR structure is first considered. Compared to the reflection from a structure with step indices, i.e. SiO₂ Omni-AR on SiNx coated Si substrate (Figure 2.14(a)), the reflection is reduced from ~10% to ~2% for a structure with graded index (n_2 changes from 1.5 to 4.0) between Omni-AR and Si substrate for incident angles up to 60° (Figure 2.14(b)).

If the index profile of the Omni-AR structure can be adjusted, The effect of index profile on reflection is observed. Shown in Figure 2.15(a) is a case where the Omni-AR index varies from air to SiNx (n_1 changes from 1.0 to 2.0) with a fixed-index film below. We only see slight reduction in reflection over Figure 2.15(a). On the other hand, as shown in Figure 2.15(b) if the Omni-AR index varies from air to Si substrate (n_1 changes from 1.0 to 4.0) without the SiNx film in between, we see close to zero (<4%) reflection over the entire spectral region of simulation for light with incident angles less than 60° . Such an ideal Omni-AR structure offers significantly improved performance.

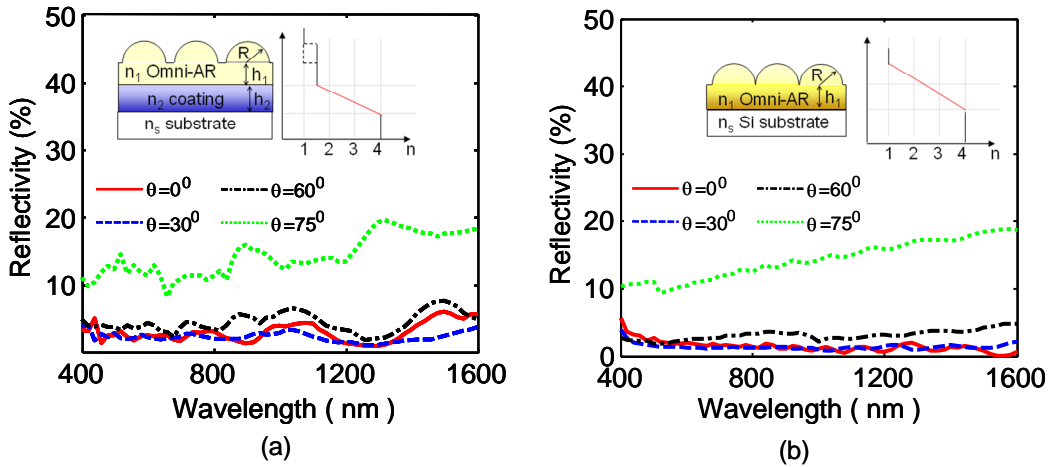


Figure 2.15 Reflectivity simulation results for graded index Omni-AR structures on high index Si substrate: (a) Index profile from air ($n = 1.0$) to SiNx film below ($n = 2.0$) and (b) ideal index matching from air to Si substrate (n varying from air $n = 1.0$ to Si $n = 4.0$)

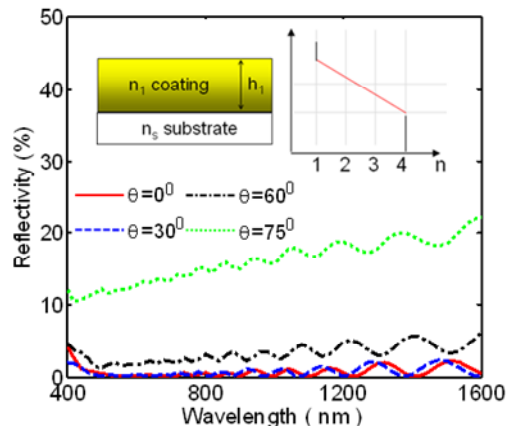


Figure 2.16 Reflectivity simulation result for ideal GRIN thin films on Si substrate, n varies from 1.0 to 4.0.

On the other hand if the planar thin film index varies from air to Si substrate (see Figure 2.16 n_1 changes from 1.0 to 4.0), the reflection is even lower than ideal Omni-AR case. The reason is that the refractive index contrast for ideal Omni-AR case is higher at the open region of hemisphere microstructures than planar thin film GRIN structure.

2.2.5 Solar Cell Performance

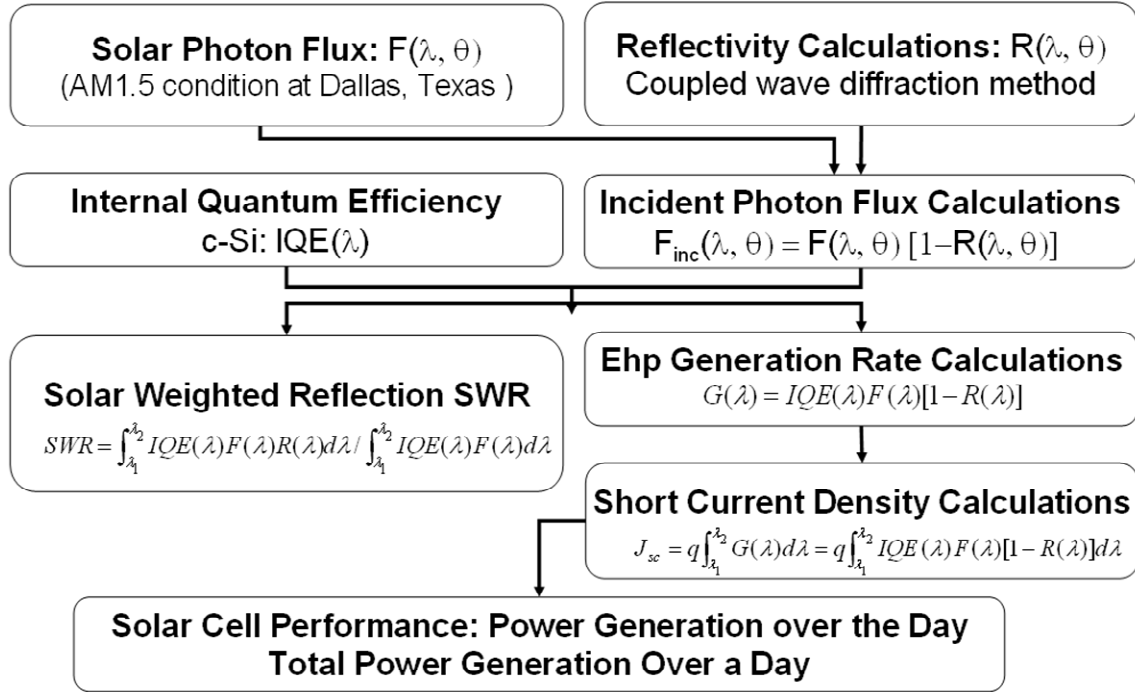


Figure 2.17 Simulation procedure for solar cell performance evaluation based on the optical characteristics of solar cell thin films

Solar cell performance was evaluated based on the simulated reflection characteristics. Assuming the bulk Si is thick enough to absorb all trapped light, the absorption equals 1-reflection (1-R). An outline of the simulation procedure is shown in Figure 2.17. The solar spectra $F(\lambda)$ obtained from solar radiation with AM1.5 condition at Dallas, Texas[63]. $R(\lambda)$ is the reflection spectrum based on RCWA simulation results. The internal quantum efficiency (IQE) of c-Si is obtained from experiment results. From $F(\lambda), R(\lambda)$ and $IQE(\lambda)$, so called solar weighted reflection (SWR) can be expressed as[64]

$$SWR = \int_{\lambda_1}^{\lambda_2} IQE(\lambda)F(\lambda)R(\lambda)d\lambda / \int_{\lambda_1}^{\lambda_2} IQE(\lambda)F(\lambda)d\lambda \quad (2.3)$$

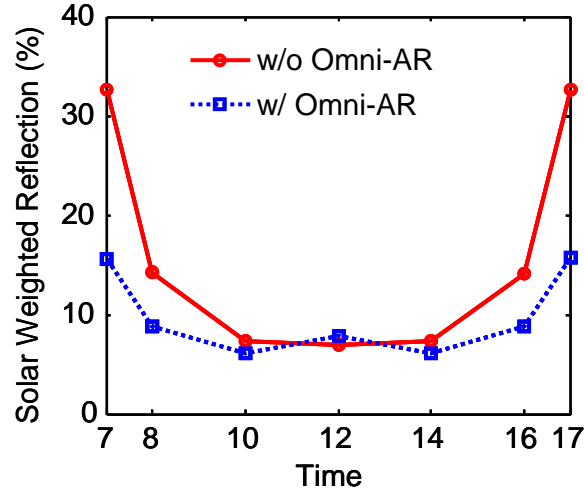


Figure 2.18 Solar weighted reflection (SWR) on Omni-AR w/ SiNx microstructure and reference SiNx on Si microstructure(both are shown in Figure 2.10)

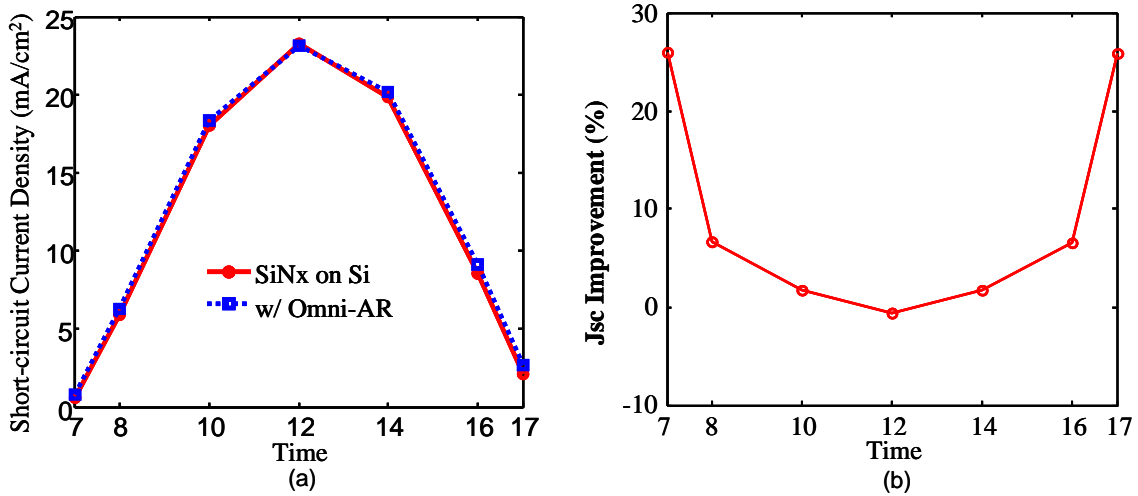


Figure 2.19 (a)Short-circuit current density(Jsc) of Omni-AR w/ SiNx and SiNx on Si (both are shown in Figure 2.10). (b) Jsc improvement with Omni-AR

The wavelength window for our modeling is between $\lambda_1 = 400$ nm and $\lambda_2 = 1150$ nm for Si. The incident angles of 0° , 30° , 60° and 75° correspond to real solar power at different time for example, 12pm, 10am/2pm, 8am/4pm and 7am/5pm, respectively. As shown in Figure 2.18, the SWR from Omni-AR microstructure is much lower than that of Si under SiNx microstructure except at 12pm, which is consistent with reflection spectra shown in Figure 2.10.

More important parameters of solar cells, short circuit current density, J_{sc} is defined as the current density when two contacts of solar cells are shorted. J_{sc} directly weights the light trapping efficiency of the solar cells and it can be derived by:

$$J_{sc} = q \int_{\lambda_1}^{\lambda_2} I_{QE}(\lambda) F(\lambda) (1 - R(\lambda)) d\lambda \quad (2.4)$$

Figure 2.19 (a) shows the J_{sc} of previous two cases and the improvements with Omni-AR in terms of J_{sc} is shown in Figure 2.19 (b). Omni-AR microstructure can generate higher current than planar SiNx on Si AR microstructure at most of time slots except a slight smaller (0.994) current at noon time.

From the J_{sc} , the total generated daily current (I_{da}) can be expressed by:

$$I_{da} = \int_{t_1}^{t_2} J_{sc}(t) dt \quad (2.5)$$

Nine different structures under investigation and their parameters are summarized in Table 2.2.

Table 2.2 Description and key parameters of nine different structures

Case #	Structure	Description
1	Bare Si	Si bulk only
2	Si under SiNx	75nm SiNx (n=2) on Si bulk
3	Si under SiO ₂	100nm SiO ₂ (n=1.45) on Si bulk
4	Omni-AR on Si (Figure 2.9 (b))	Omni-AR on Si bulk
5	Omni-AR w/ SiNx on Si (Figure 2.10)	Omni-AR w/ 75nm SiNx (n=2) on Si bulk
6	Omni-AR w/ GRIN thin film on Si (Figure 2.15 (a))	Omni-AR on 0.5μm GRIN 249 layers(n changes from 1.51 to 3.99) on Si bulk
7	GRIN Omni-AR on Si (Figure 2.15 (b))	GRIN Omni-AR 249 layers(n changes from 1.01-1.5 for hemisphere and n changes from 1.51-3.99 for thin film) on Si bulk
8	GRIN thin film on Si (Figure 2.16)	GRIN thin film 299 layers (n changes from 1.01 to 3.99) on Si bulk
9	Ideal case	100% absorption

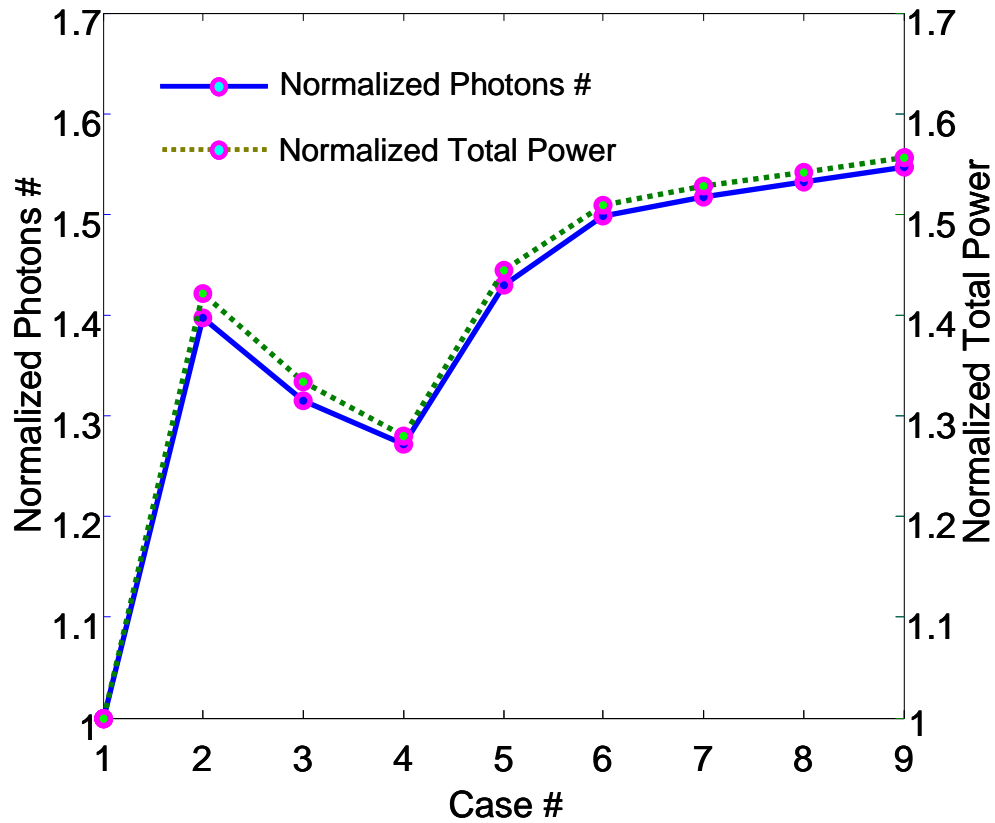


Figure 2.20 Normalized photons number and normalized total power in nine different structures

Assuming same fill factor (FF) and open circuit voltage (V_{oc}) are applied, the photon number and the power in each structure are normalized to those of reference bare Si structure. The normalized photons and normalized total power are shown in Figure 2.20. The Omni-AR with SiNx microstructure can achieve 1.43 time higher power compared to bare Si and also achieve 4% higher power than SiNx on Si structure. Only 10% efficiency gap as compared to ideal case (100% absorption) that indicates Omni-AR structure is very effective for light trapping

2.3 Omni-AR Coatings on Different Substrates

The Omni-AR microstructures are formed by partially immersing microscale spherical particles into a dielectric film of the same refractive index. Both the particle array and the dielectric film can be prepared from solutions containing microscale particles and precursors for

the dielectric film. The performance of the coating can be controlled by tuning the size and packing density of the dielectric particles and the thickness and refractive index of the dielectric film, as discussed in previous section in this chapter. Some coating approaches can be used for Omni-AR coating, like spinning coating, dip coating and convective coating. The advantages and disadvantages of each coating have been summarized[65].

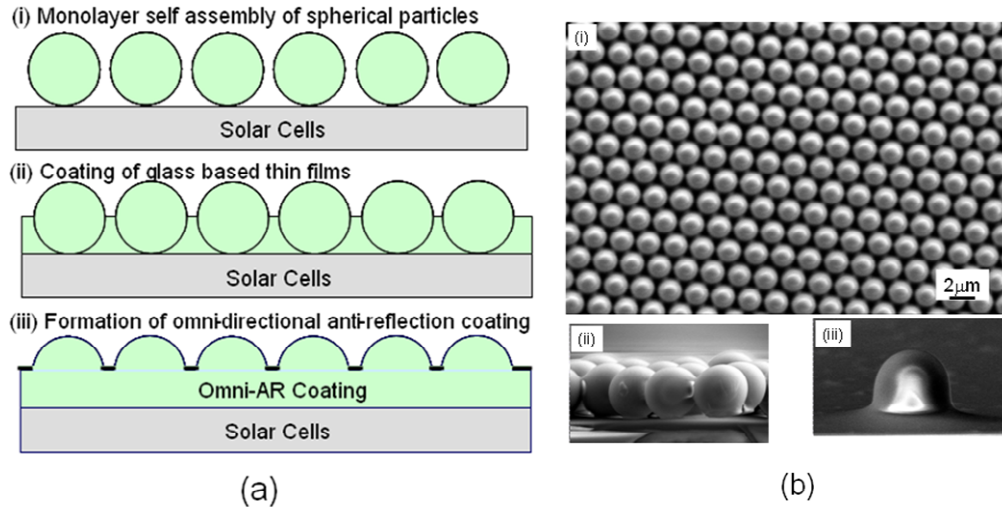


Figure 2.21 (a) Omni-AR coating based on monolayer of spherical particles and spin-on-glass (SOG) film; (b) Scanning electron micrographs of fabricated Omni-AR coatings: (i) top view; (ii) cross-sectional view before SOG film and (iii) cross-sectional view after SOG film.

Shown in Figure 2.21 (b) are scanning electron micrographs of processed Omni-AR structures on quartz substrates. A closely packed monolayer of 2 μm silica spheres were first deposited on the substrate, followed by coating of a spin-on-glass (SOG) film with a desired thickness, with Figure 2.21 (b) showing a 0.2 μm SOG film. Finally an Omni-AR structure is formed after baking to cure the SOG film. Detailed experimental conditions of spinning coating can be found in our reference[55].

Since the purpose of an anti-reflection coating is to maximize light transmission, total transmission of quartz wafers with various coatings has been measured using a JASCO V-570 spectrophotometer. The coating was done on one side of the quartz wafer based on the spin coating processes. An integrating sphere was used in the measurement, which collects

transmitted light through a sample from all directions. Total transmission measurements at different incident angles have also been performed using a home-built monochromator-based spectroscopic setup with an integrating sphere. The white light from a 100-W Oriel quartz tungsten halogen lamp was focused on the sample at different incident angles through a flexible liquid light guide. Care was taken to ensure the focused light can be coupled into the integrating sphere. Due to limitations in the setup, the maximum incident angle is limited to $\sim 30^\circ$.

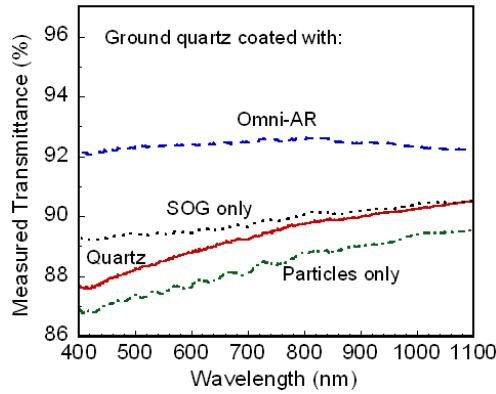


Figure 2.22 Total transmissivity under normal incidence of quartz wafers with various surface coatings.

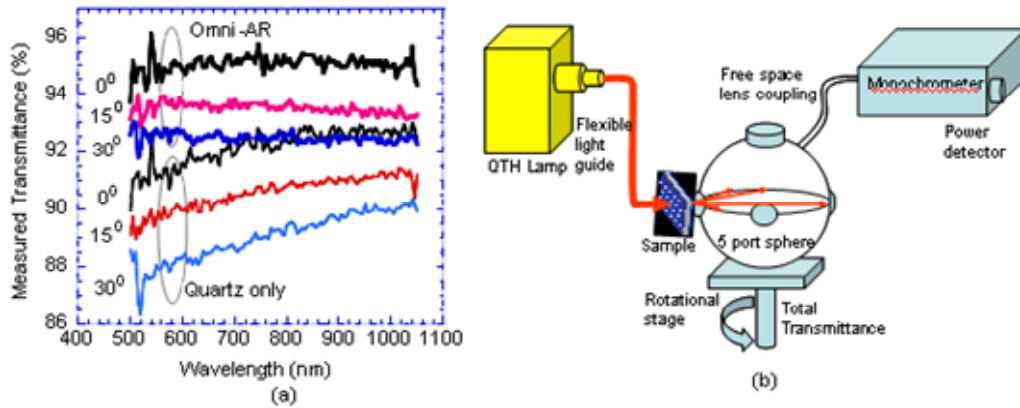


Figure 2.23 (a) Angle-dependent transmissivity of a quartz wafer before and after an Omni-AR coating; (b) Schematic of experimental setup for angle dependent total transmittance setup.

Figure 2.22 shows a normal-incidence total transmission measurement of a quartz with an Omni-AR coating, which comprises a monolayer of $2\mu\text{m}$ spherical silica particles immersed

in a SOG film of 0.2 μ m thick. For comparison, the total transmission of a quartz wafer without any coating, a quartz wafer coated with 0.2 μ m SOG only and a quartz wafer coated with a monolayer of 2 μ m spherical silica particles only were also measured. The Omni-AR coating improves the transmission from ~88% to ~92% at 400 nm and from ~90% to ~92% at 1,100 nm, demonstrating its broad-spectrum effect. Since the bare quartz wafer already has a high transmission above 88%, the improvement by the Omni-AR coating is tainted by the high background transmission. A 0.2 μ m SOG film alone slightly improves the transmission at short wavelengths by ~1%, possibly due to its smaller refractive index (~1.39), than that of quartz (~1.55). The reduced surface roughness could be another contributing factor here. A monolayer of 2 μ m silica spherical particles alone decreases the transmission by ~1% in the entire spectral range of interest. This is likely due to reflection from the multiple surfaces in the monolayer particle coating: the top surface of the particles, the bottom surface of the particles and the surface of the quartz wafer. Light was scattered away on these particles surfaces, which could lead to reduced transmission. Therefore, the SOG film not only serves as a glue to hold together the coating, but also reduces the number of internal surfaces which cause reflection.

An incident-angle dependent transmission measurement for the Omni-AR coating on quartz wafer, along with the schematic of experimental setup, is shown in Figure 2.23. Within the limited range of incident angle (~30°), the Omni-AR coating improves the total transmission from ~87% to ~92% at 500 nm and from ~89% to ~92% at 1,000 nm for an incident angle of 30°. Note under surface-normal incident light condition, the measured transmittances show similar spectral dependences for quartz and quartz with Omni-AR coating. However, the absolute transmittance values are different. It is mostly due to the different experimental setup we used and variations in the calibration processes.

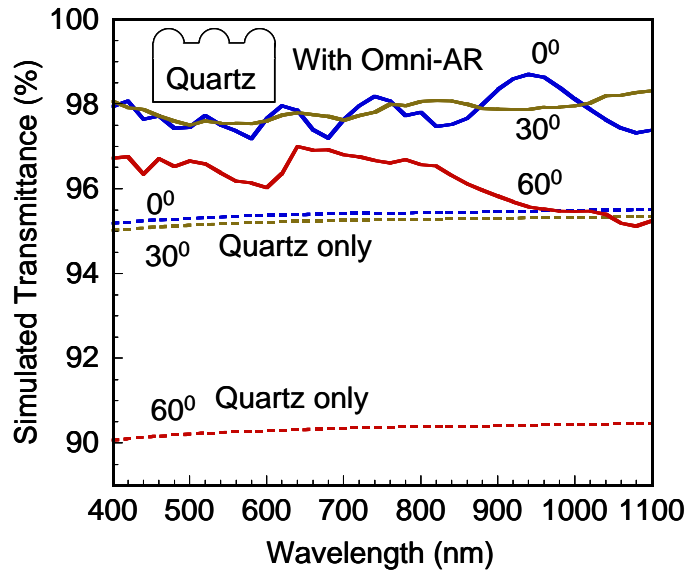


Figure 2.24 Simulated transmittance at different incident angles for quartz wafers with and without an Omni-AR coating.

Figure 2.24 is simulated transmission of quartz wafers with and without an Omni-AR coating at different incident angles. To match the experimental conditions, the coating in the simulation consists of a $0.2\mu\text{m}$ SOG film with $2\mu\text{m}$ hemispherical particles on top (particle radius $R=1\mu\text{m}$). The wavelength-dependent refractive index is assumed to be that of silica, as shown in Figure 2.8(b). However, the simulation did not take into account the reflection from the back surface of the quartz wafer, which could lead to a slight reduction in the actual transmitted power. The transmission increases from $\sim 95\%$ to $\sim 98\%$ with the coating at small incident angles of 0° and 30° . The results agree reasonably well with experiments in Figure 2.22 and Figure 2.23. The simulated results for large incident angle are also shown for completeness. With a large incident angle of 60° , the transmission increases from $\sim 90\%$ to $\sim 96\%$.

Omni-AR structures can be also easily assembled onto other materials as well. Figure 2.25(a) and (b) show $2\mu\text{m}$ silica nanoparticles self assembled on Si substrate by dip coating and convective coating respectively. Figure 2.26(a) shows uniform monolayer silica nanoparticles coated on $6''\times 6''$ glass slides with convective coating and Figure 2.26 (b) shows

Omni-AR structures formed on glass substrate. The detail method and setup of dip coating and convective coating has been well documented[66, 67].

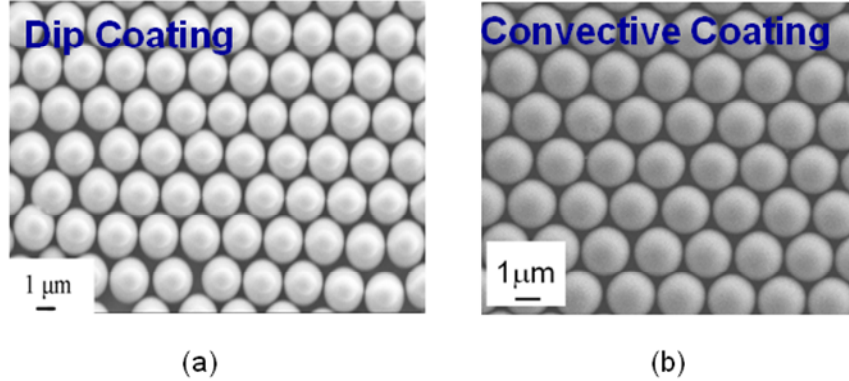


Figure 2.25 2 μ m nanoparticles self assembly on Si by (a) dip coating (b) convective coating

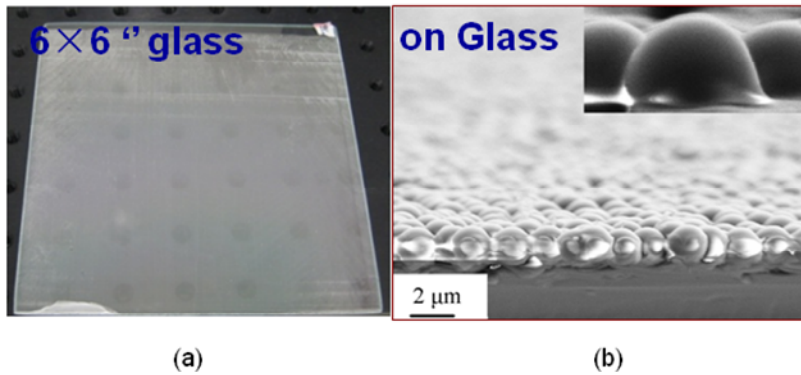


Figure 2.26 (a) Convective coating Omni-AR on 6x6" glass slide (b) SEM image of Omni-AR coating on glass

Here just briefly introduce the convective coating procedure which is also used for the commercial solar cells (will discuss in the next section). As shown in Figure 2.27, the nanoparticle containing solvent (typical ethanol for faster coating speed) is injected into the wedge formed by the plate and solar cells. Nanoparticle concentration in solvent, solvent volume, plate speed and the wedge angle are main factors to affect the quality of coating. To achieve uniform monolayer nanoparticle coating, two requirements are needed. First, the particle growth speed equals plate moving speed. Secondly, the evaporation flux of the solvent is equal to entering fluxes of particles and solvent. For 1 μ m Silica nanoparticle, 8% nanoparticle

concentration in 40 μ L solvent volume each injection is typically chosen to get faster coating without degrading the coating quality.

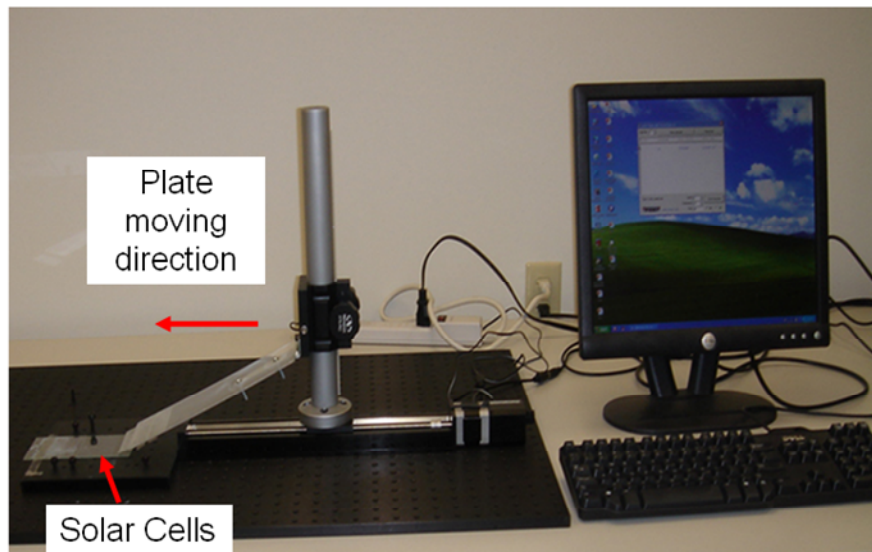


Figure 2.27 Convective coating setup

2.4 Omni-AR Coatings Integration with Commercial Solar Cells

The amorphous silicon solar cell, supplied by Microspheres-Nanospheres, a Corpuscular Co., contains ITO and two copper leads as negative and positive electrodes at each end as shown in Figure 2.28(a). The surface roughness is in the range of 0.2-0.3 μ m. The height of copper leads above the ITO film is around 8-10 μ m. The presence rough surface is a challenge to the formation mono layers of silica particles over the entire surface of the cell. Uniform and closely packed monolayer 1 μ m Silica nanoparticle were able to obtain with coating speed at around 0.22mm/s as shown in Figure 2.28(b). The Omni-AR coated be able uniformed coated on a-Si solar cells as shown in Figure 2.28 (c and d). The experimental reflection shown in Figure 2.29 is agreed well with simulation results. After Omni-AR coating, the reflection on the a-Si solar cell is much reduced and reflection oscillations is also significantly suppressed.

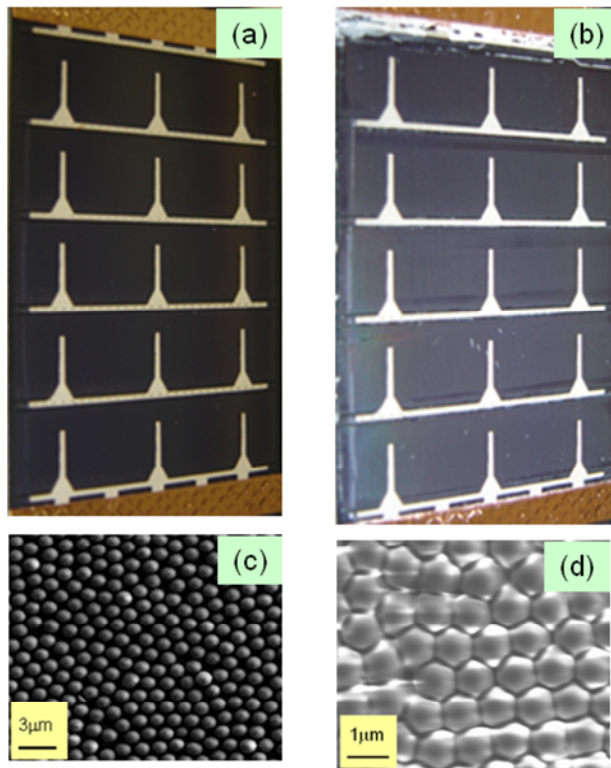


Figure 2.28 a-Si (a) w/o (b) w/ Omni-AR coating (c) SEM picture of $1\mu\text{m}$ Silica nanoparticles self assembly on a-Si solar cells (d) SEM picture after Omni-AR formed on a-Si solar cells

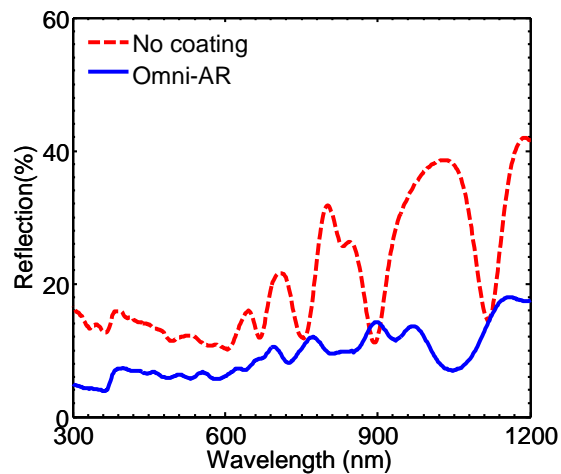


Figure 2.29 Reflection measurements on a-Si solar cells before and after Omni-AR coating under normal incident

As shown in Figure 2.30, the current–voltage (I-V) characterization was done under standard test conditions (STC, 25°C temperature and $100\text{mW}/\text{cm}^2$ irradiation) provided by

Newport solar simulator, with xenon lamp as the light source. The power supply is set at 300 W, 15 Amps and 20 volts. Rotatable stage can measure different incident angle I-V for solar cells. Two probe crocodile clips were used in case small electrode areas on solar cells which is shown in Figure 2.30 (b).

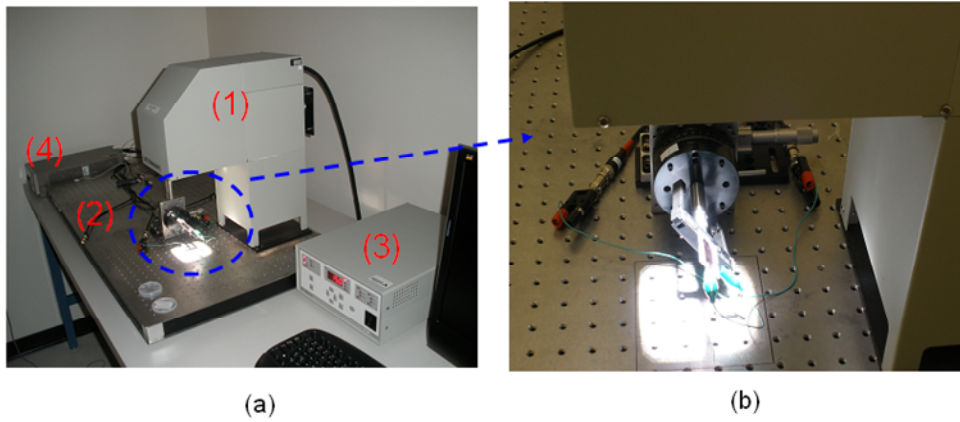


Figure 2.30 Solar Cell I-V characterization (a) setup (b) as example of 45° testing under AM 1.5 illumination

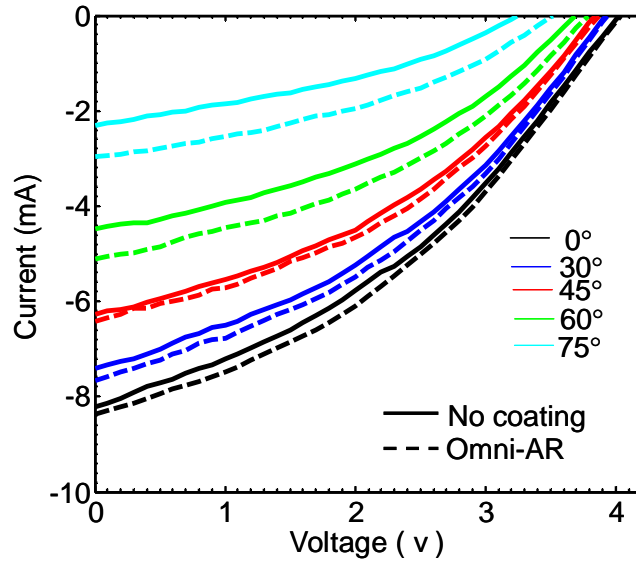


Figure 2.31 I-V measurement results for a-Si solar cells before (solid lines) and after (dash lines) Omni-AR coating under incident angle from 0 ° to 75°

Under this setup, I-V test is executed for a-Si solar cells and result is shown in Figure 2.31. I_{sc} is improved due to more light coupling into a-Si solar cells by Omni-AR coating. The larger incident angle, the more I_{sc} increase. This result is encouraging because it indicates that our Omni-AR not only works for the first generation wafer level solar cells, but also improves the efficiency for thin film solar cells.

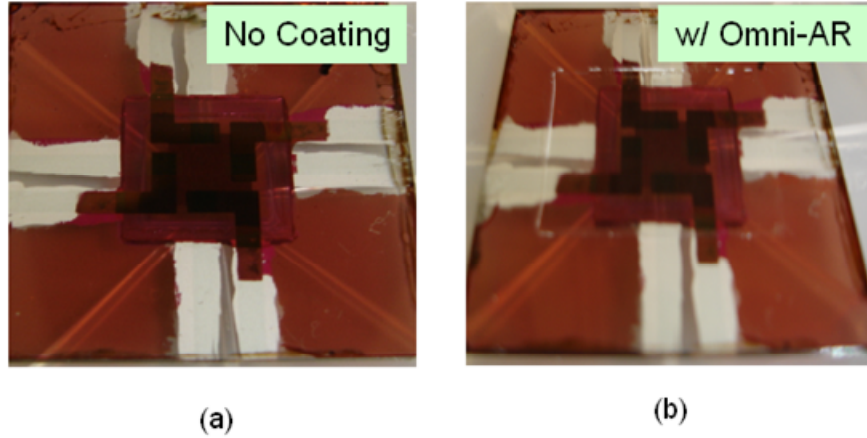


Figure 2.32 Organic Solar Cells (a) before and (b) after Omni-AR coating

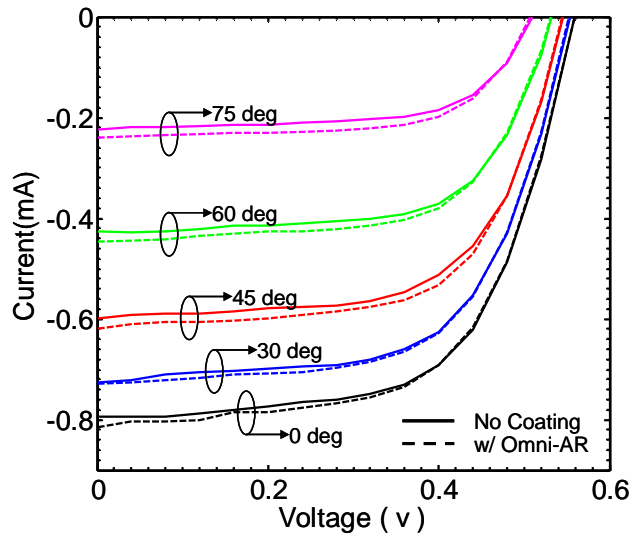


Figure 2.33 I-V measurement results for organic solar cells before (solid lines) and after (dash lines) Omni-AR coating under incident angle from 0° to 75°

The other measurement is executed on organic solar cells from Plextronics company. Due to smooth surface, the uniform and closely packed 1 μ m Silica nanoparticle coating is fulfilled with a reduced speed (0.142mm/s). Shown in Figure 2.32 (a) and (b) are images of organic solar cells before and after Omni-AR coating respectively. We see similar Isc increase under different incident angles shown in Figure 2.33. The Isc and efficiency of Omni-AR coated solar cells are increased 7% and 9% respectively at large incident angle ($\theta=75^\circ$) respectively (Figure 2.34).

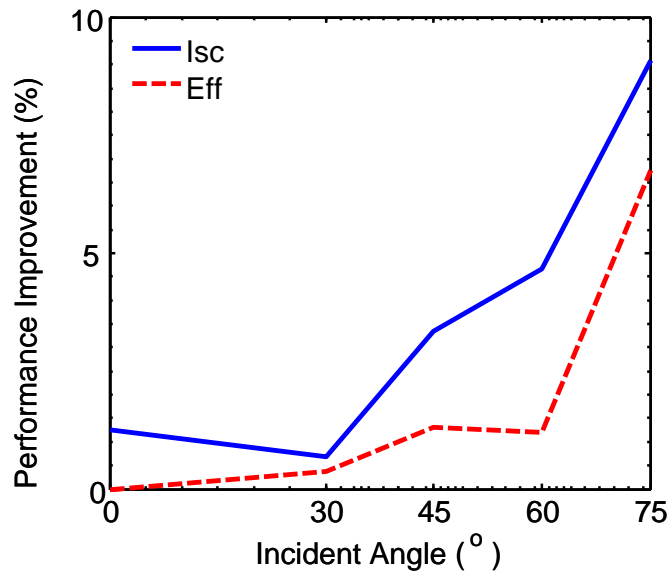


Figure 2.34 Performance improvement after Omni-AR coating in Isc(in solid blue) and efficiency (in dash red) with incident angle from 0° to 75°

Based on both simulation and experiment results from this chapter, Omni-AR coating is demonstrated to be a cost effective and material independent light trapping approach for solar cells.

CHAPTER 3
 INFRARED ABSORPTION ENHANCEMENT IN ONE-DIMENSIONAL (1D) PHOTONIC
 CRYSTAL (PC)

Photonic crystals can engineer photonic density of states(DOS) and therefore alter absorption[68]. Because light can not exist or pass through the photonic band gap (PBG) region, absorption is dramatically reduced. Introduce a defect cavity in PC, photonic DOS is only concentrated at defect mode. The enhanced absorption can be expected. On the other hand, high photonic DOS and very low group velocity at bandedge region will increase light matter interaction. As a result, enhanced absorption can be also expected in defect free PC cavities[31].

3.1 Simulation Approach for 1DPC

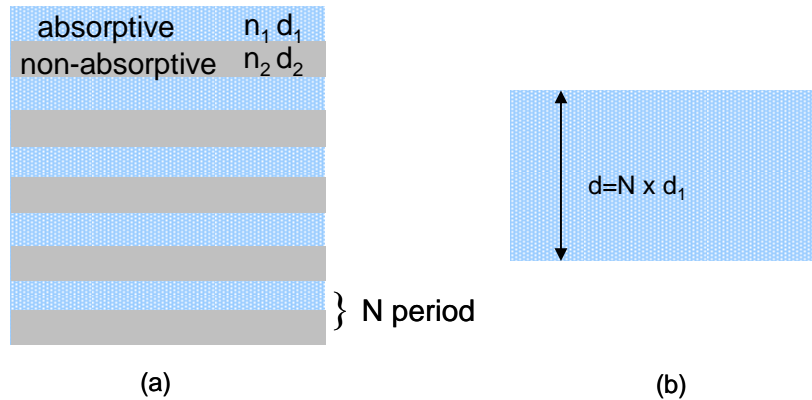


Figure 3.1 Structures under simulation: (a) 1D PC structure with absorptive layers; (b) Reference bulk absorptive material with equivalent absorption thickness.

As shown in Figure 3.1(a), one-dimensional photonic crystals (1D PC) consists of absorptive and non-absorptive layers arranged alternately, with refractive index and layer thickness of n_1 , d_1 , and n_2 , d_2 , respectively. The bulk material with equivalent absorptive thickness is also used as the reference (Figure 3.1(b)), with refractive index n_1 and thickness d . For N period 1D PC, the equivalent absorptive bulk material thickness d equals to Nd_1 .

The simulation is based on Transfer Matrix Method (TMM) theory which has been widely used[69, 70] The main ideal of TMM is using the scattering matrix (S matrix) of the entire system relates the outgoing wave amplitude (reflection coefficient) to the incoming wave amplitude (transmission coefficient) on either side of the whole structure. In order to calculate the S matrix, The whole structure is divided into N segments perpendicular to the surface. The S matrix for each segment is determined by solving Maxwell's equations directly inside the segment. Within each segment, the solution of the S matrix becomes relatively simple when the size of the segment is sufficiently small. The total S matrix (including transmission and reflection) is then constructed by cascading the S matrix from each segment, using the multiple scattering formula.

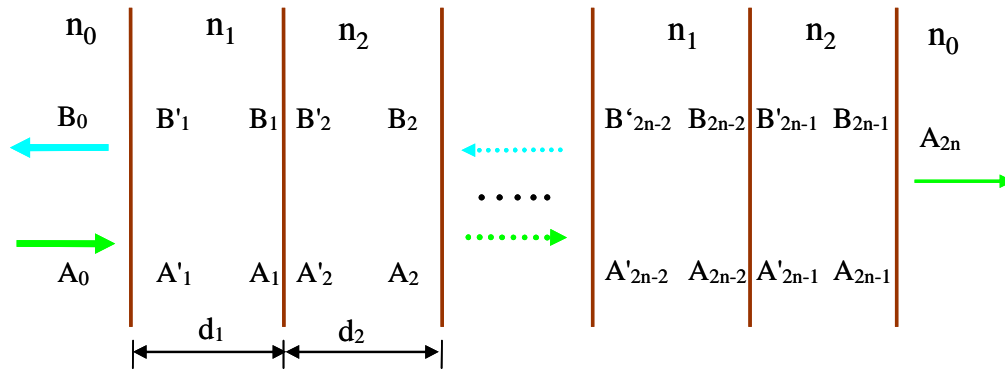


Figure 3.2 Schematic of the transfer matrix method (TMM) theory

According to this approach, as shown in Figure 3.2, whole 1D PC structure is divided into unit cells each of which contains two transfer matrices: P_n and Q_n , The former is applied on the field propagation in a uniform medium and the later is used for the interface between two media, i.e.

$$\begin{pmatrix} A_1 \\ B_1 \end{pmatrix} = P_1 \begin{pmatrix} A'_1 \\ B'_1 \end{pmatrix} \quad \text{and} \quad \begin{pmatrix} A'_1 \\ B'_1 \end{pmatrix} = Q_1 \begin{pmatrix} A_0 \\ B_0 \end{pmatrix} \quad (3.1)$$

The overall transfer matrix M is expressed as the following equation, where 1,2,3...indicate the number of the unit cell counting from the incident direction:

$$\begin{pmatrix} A_{2n} \\ 0 \end{pmatrix} = M \begin{pmatrix} A_0 \\ B_0 \end{pmatrix} \quad (3.2)$$

where

$$M = Q_{2n+1} \prod_{L=2n}^1 P_L Q_L \quad (3.3)$$

The final transmission (T) and reflection (R) can be obtained from the M as:

$$T = |M_{11} - M_{12}M_{21}/M_{22}|^2, \quad (3.4)$$

$$R = |M_{21}/M_{22}|^2 \quad (3.5)$$

As a result, absorption can be obtained from the relation: $A=1-T-R$ [71], assuming other losses are negligible.

3.2 Absorption Enhancement at Photonic Bandedge

The simulation results are shown in Figure 3.3, for two different structures. Significant suppression in absorption, as compared to the bulk, is evident for the frequencies within the photonic PBG. On the other hand, enhanced absorption occurs at either higher or lower bandedges of the PBG, depending on the relative refractive index differences for these two structures. Due to the energy concentration in the high-index region[72], the enhancement occurs at the lower frequency bandedge when the absorptive layer refractive index is higher.

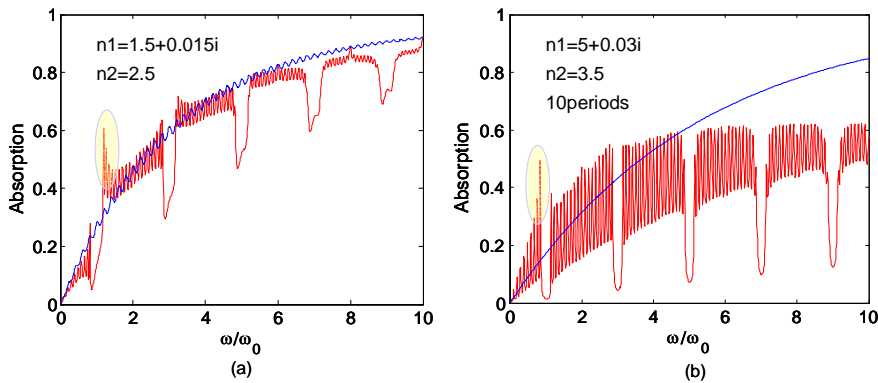


Figure 3.3 Simulated absorptance for 1D PCs, with the refractive index of the absorptive layer to be either (a) lower or (b) higher than that of the non-absorptive layer. The absorptance for the reference bulk material is also shown as the reference.

As shown in Figure 3.4, the normalized absorption for i.e. in the PbSe and Si consisting PC structure is plotted for a small frequency (wavelength) range near the lower frequency bandedge. The spectral selectivity increases with the increase of the period. Additionally we found the ratio of the absorption enhancement at bandedge and the absorption suppression within PBG was more than 40 for the case with 10 periods.

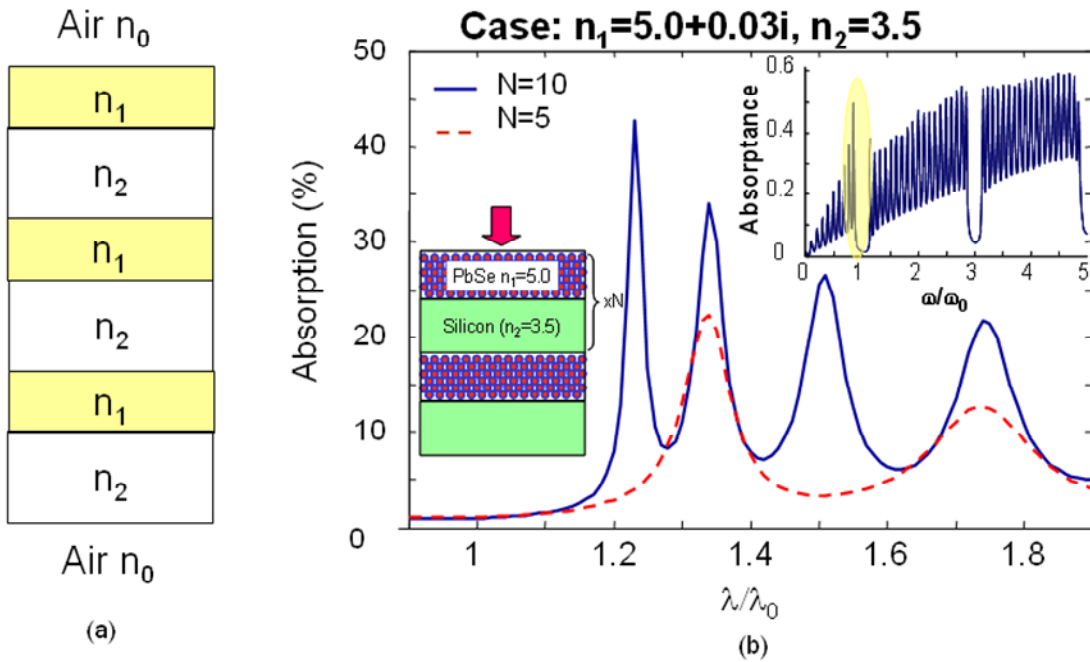


Figure 3.4 (a) Schematically show the 1D PC (b) Enhanced absorption in wavelength domain at bandedge with periods $N=5,10$ for 1D PC consists by PbSe and Si. Inset shows the absorbance at frequency domain

3.3 Defect Cavity versus Resonance Cavity

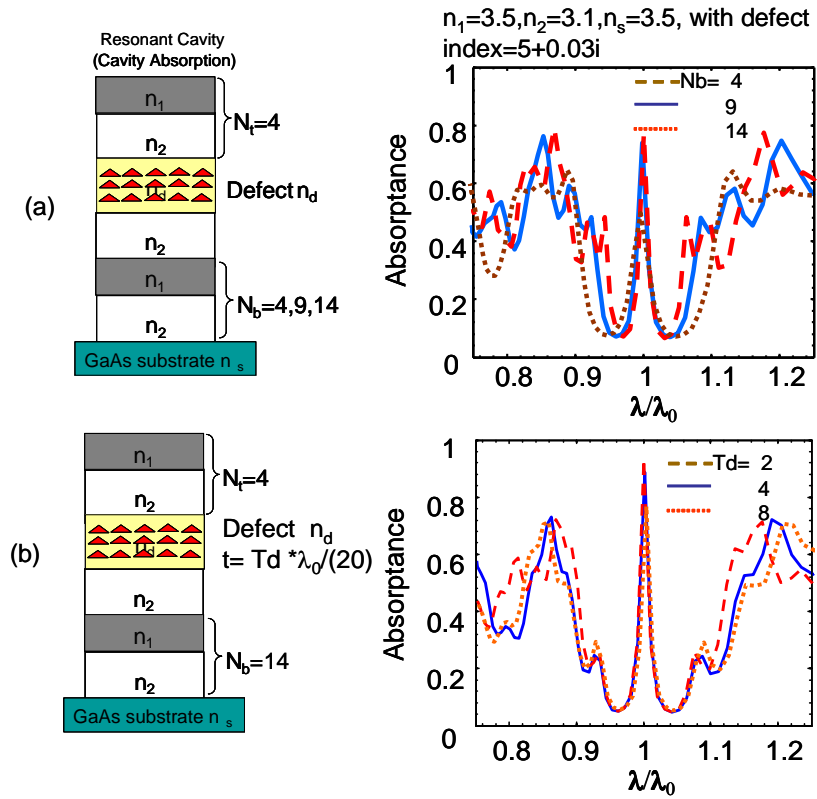


Figure 3.5 (a) PC with defect: distributed absorption at defect level with $n_1 = 3.6 + 0.028i, n_2 = 3.0, n_s = 3.5$. (b) Resonant cavity: cavity absorption at defect level with $n_1 = 3.5, n_2 = 3.1, n_s = 3.5$, and $n_d = 5 + 0.03i$

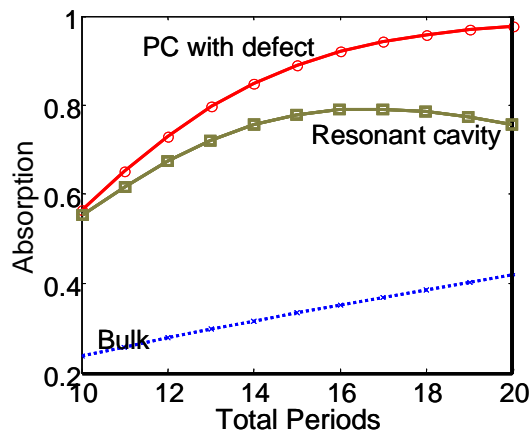


Figure 3.6 Absorption comparison of Figure 3.5(a), (b) and bulk with periods from 10 to 20.

To tune the absorption peak position, single defect and resonant cavity were introduced into the otherwise defect-free PC. In the single defect structure, PC is consisted with one absorptive material and one non-absorptive material (Figure 3.5(a)) and the defect layer is also made of that absorptive material (Figure 3.5(b)). On the other hand, the resonant cavity PC structure is consisted with two different non absorptive materials with foreign absorptive material to create cavity region. Due to the existence of the strong localized mode, much stronger enhancement in the absorption was observed in the defect level, with close to 100% absorption while absorption saturation was observed in the conventional resonant cavity, as shown in Figure 3.6. Compared to the bulk structure with the same absorption layer thickness, 2-fold enhancement factor is evident for the single-defect PC cavity.

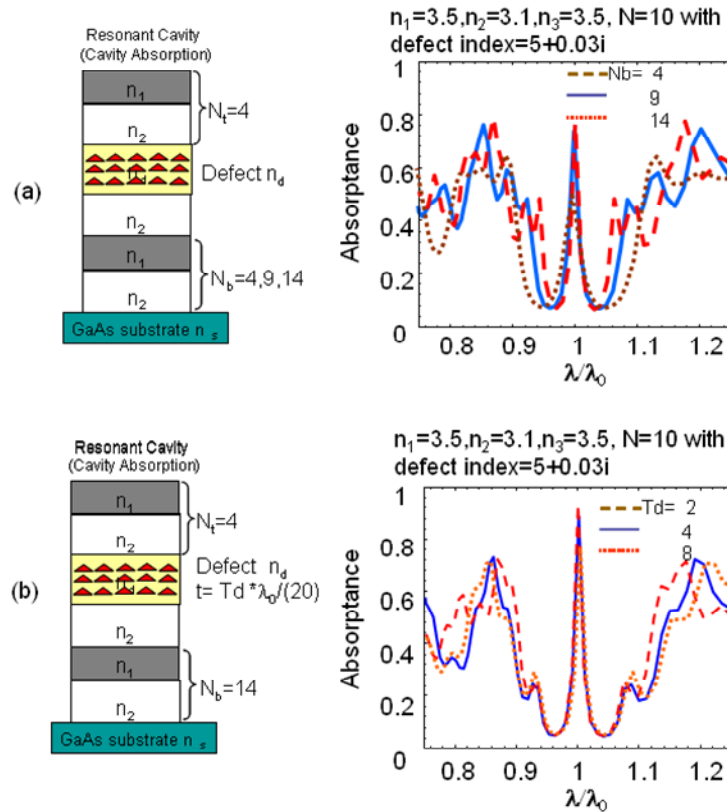


Figure 3.7 Absorbance peak optimization by (a) tuning bottom DBR period (b) by tuning defect absorptive layer thickness

To improve the absorptance, we further optimize resonant cavity configurations. Only increase the bottom DBR periods can not improve the absorptance as shown Figure 3.7(a). With large period of bottom DBR and further increase the cavity thickness t will quickly improve absorptance. As shown in Figure 3.7 (b), 93.4% absorption is achieved with 14 periods of bottom DBR ($N_b = 14$) and 8 times quart wavelength thick resonant cavity ($T_d = 8$). In this case, the total absorptive thickness is only half as similar absorption obtained in defect cavities with 16 periods.

CHAPTER 4

TWO DIMENSIONAL (2D) ABSORPTIVE PHOTONIC CRYSTAL SLAB (PCS) SIMULATION

Simultaneous inhibition and redistribution of spontaneous emission in PC has been demonstrated theoretically and experimentally in a lossless dielectric PCS structure[33]. The introduction of an absorption layer in a two dimensional (2D) dielectric PCS structure (e.g. quantum well, quantum dots) can lead to the modification of the absorption characteristics, due to the spectrally-selective light-matter interaction in the cavity. In this chapter, photonic crystal infrared photodetectors (PCIP) configuration is proposed, where the photonic crystal defect cavity was integrated with the quantum dot infrared photodetectors (QDIPs).

4.1 In Plane Source in 2D PCS

4.1.1. 2D PCS Configuration

A 2D PCS under investigation, where a triangular air hole PC cavity in three layers, in which an absorptive layer sandwiched by two non-absorptive layers, as schematically shown in Figure 4.1(a) for top view for single defect cavity (H_1) and (b) for cross-section view of H_1, H_0 and reference bulk. The parameters are listed in Table 4.1.

Table 4.1 2D absorptive photonic crystal slab parameters

Parameter	Value
Photonic Crystals with triangular lattice	10 periods
Lattice Constant a	$0.38\mu\text{m}$
Air hole Radius r	$0.25a$
Thickness of non-absorptive layer h_1	$0.3a$
Refractive index of h_1 layer	3.5
Thickness of absorptive layer h_2	$0.2a$
Refractive index of h_2 layer	$3.6+k_a*i$

Note: k_a is the extinction coefficient

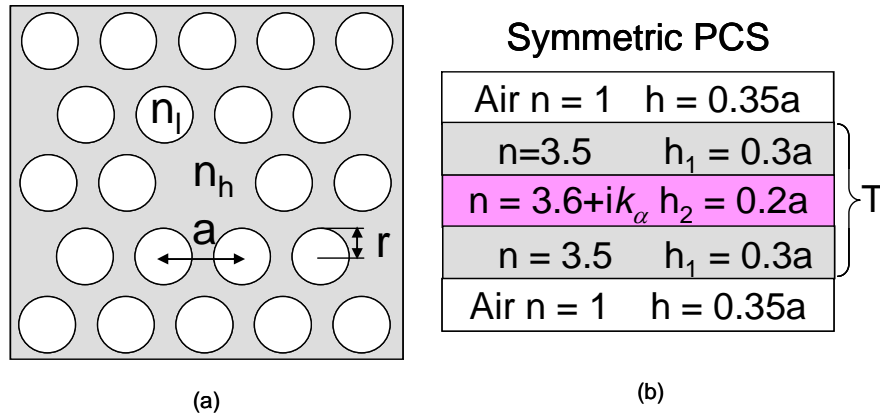


Figure 4.1 2D absorptive PCS (a) top view of H_1 defect cavity (b) cross-section for H_1 H_0 and reference bulk

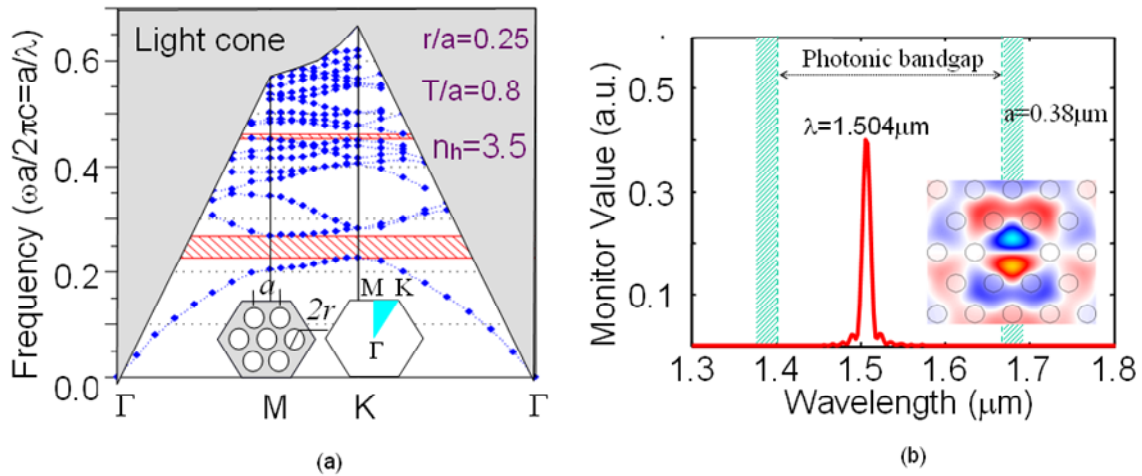


Figure 4.2 (a) PBG dispersion plot for 2D PCS (b) Simulated PBG and the defect mode characteristics in the single defect H_1 PC cavity. The defect level was confirmed to be a dipole mode (inset) with center wavelength ($1.504 \mu\text{m}$) close to the center of the PBG (1.41 to $1.67 \mu\text{m}$)

The band structure of 2D PCS is shown Figure 4.2, where the primary photonic bandgap is from 1.41 to $1.67 \mu\text{m}$ as the bottom red region shown in Figure 4.2(a). The single defect (H_1) PCS cavity was confirmed to be a dipole mode (inset of Figure 4.2(b)) with center wavelength ($1.504 \mu\text{m}$) close to the center of the photonic bandgap (PBG). The absorption layer extinction coefficient k_a , i.e., the imaginary part of the refractive index, was tuned for different absorption coefficient α ($k_a = \alpha \lambda / 4\pi$).

4.1.2. 3D FDTD Simulation Setup

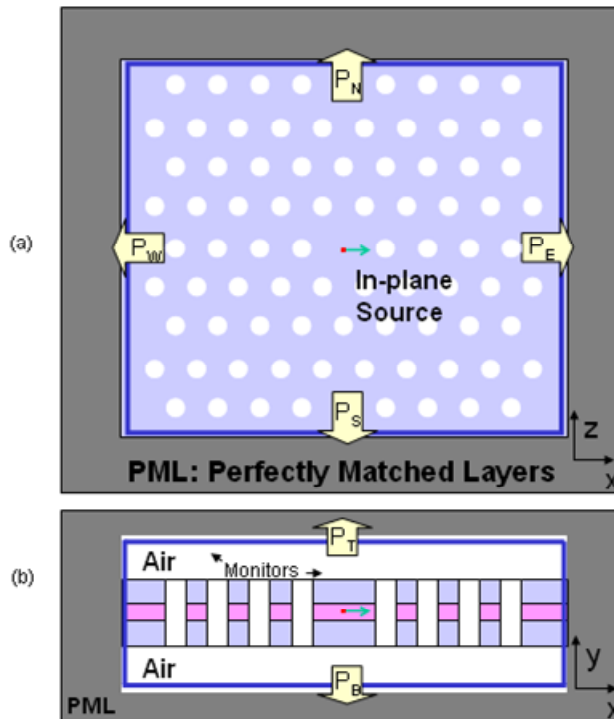


Figure 4.3 (a) Top view (b) Cross-section view of 3D FDTD simulation setup with perfectly matched layers as the boundary. An in-plane dipole source was placed at the center of the slab (red square) with monitors (blue lines) surrounding the simulation domain for both vertical and in-plane power monitoring

Three-dimensional (3D) finite-difference time-domain (FDTD) [73] simulation was carried out on 2D PCS. Perfectly matched layers (PMLs) were incorporated at the boundaries of the computational domain to avoid unnecessary reflections of light at the boundaries. Typically the PMLs should be set about half wavelength away from the structure under simulation in order to separate the vertical and in-plane components (e.g., for the quality factor calculations). In our case, by placing monitors close to the dielectric slab structure, Little change is found in the total power monitored for each monitors when the thickness of the air section shown in Figure 4.3(a) and Figure 4.3(b) changed from $2a$ (\sim half wavelength) to $0.35a$, where a is the lattice constant. To save the computational resources (memory and time), we focused our work here with air region set to be $0.35a$. A dipole source was introduced in the center of the cavity launching to

the +x direction, with a Gaussian profile to cover the desired wavelength region of interest. Total of six power monitors were placed at the boundaries to collect the transmitted spectral power density after Fourier transformation from the average of the Poynting vectors, for both in-plane power change (labeled as east (P_E), west (P_W), north (P_N) and south (P_S), respectively, as shown in Figure 4.3(a)), and vertical power change (top (P_T) and bottom (P_B) as shown in Figure 4.3 (b)). Small spatial grating size ($g_s=a/16$) along three direction is chosen, which is much smaller than the required value of $a/10$. The time step (t_s) of $0.5g_s$ (in unit of a/c , where a is the lattice constant, $0.38\mu\text{m}$ and c is light speed in the vacuum) is chosen for the total computation time t_s*2^{14} to obtain stable results. The same simulation setup was performed for the slab waveguide without photonic crystals as the reference. The key parameters of FDTD setup for 2D PCS with in-plane light source are summarized in Table 4.2

Table 4.2 3D FDTD simulation setup for 2D PCS with in-plane light source

Category	Parameters	Characterization
Globe	Computation Domain	-1.9 μm – 1.9 μm in x -0.75a – 0.75a in y -1.5 μm – 1.5 μm in z
	Grid Size	a/16
	Time Step	Grid Size/2 (in unit of a/c)
	Computation Time	Time Step* 2^{14}
Source	Source Type	Gaussian
	Source Size	0.12a x 0.1a
	Source Location	Center at (0,0,0)
Monitor	In-plane Monitor1 Size	3.7 μm x (0.8a+0.12) μm
	In-plane Monitor1 Location	Center at (0,0,1.45)
	In-plane Monitor2 Size	3.7 μm x (0.8a+0.12) μm
	In-plane Monitor2 Location	Center at (0,0,-1.45)
	In-plane Monitor3 Size	2.9 μm x (0.8a+0.12) μm
	In-plane Monitor3 Location	Center at (1.85, 0,0)
	In-plane Monitor4 Size	2.9 μm x (0.8a+0.12) μm
	In-plane Monitor4 Location	Center at (-1.85, 0,0)
	Top Monitor Size	3.7 μm x 2.9 μm
	Top Monitor Location	Center at (0, 0.4a+0.06,0)
	Bottom Monitor Size	3.7 μm x 2.9 μm
Bottom Monitor Location	Center at (0, -0.4a-0.06,0)	
Monitor Time	Time Step*10	
PML	PML Size/Location	Enclose the whole computation domain
	PML Thickness	Grid Size *10

4.1.3. Absorption Enhancement

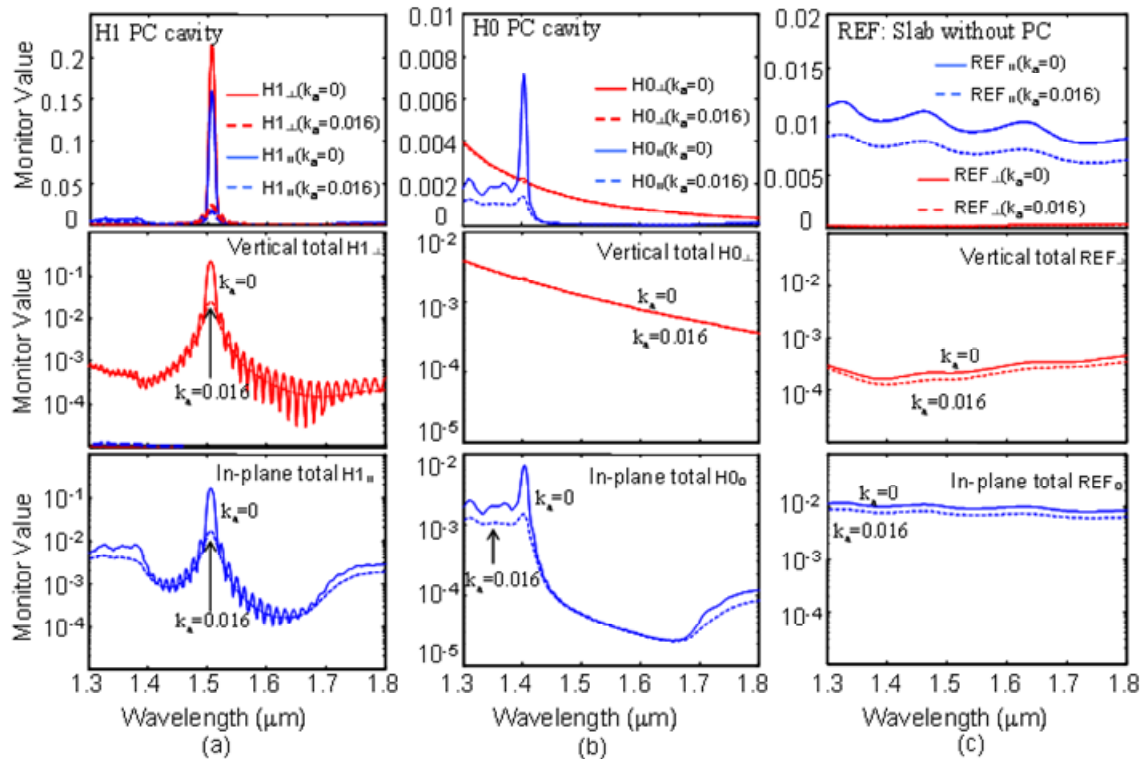


Figure 4.4 In-plane light source simulation on detected power densities from all monitors. Spectral power density based on the vertical and in-plane monitors in (a) single defect H_1 PC cavity; (b) defect-free H_0 PC cavity; and (c) reference slab without PC structure. To show the fine spectral features and relative transmitted power spectra density, the monitored values were plotted in both linear scale (top) and log-scale for both vertical monitor ($H_{1\perp}$, middle panel) and in-plane monitor ($H_{1\parallel}$, bottom panel), respectively.

The monitor power (transmitted spectral density) is shown in Figure 4.4 with $k_a = 0.016$ (dash curves) and $k_a = 0$ (solid curves), in three different cavities: (a) single defect H_1 cavity; (b) defect-free H_0 cavity; and (c) a conventional slab structure without photonic crystals (reference, slab w/o PC). The top panel shows both in-plane monitor power (subscripted as \parallel) and vertical monitor powers (subscripted as \perp) in linear scale. The middle and bottom panel show the vertical monitor and in-plane monitor in log scale respectively. It is evident that a significantly enhanced transmission at the defect level was obtained, mainly in the vertical direction. Reduced transmission with the incorporation of an absorption layer was also seen in Figure 4.4. It is worth mentioning that the dominant transmission at defect level is along vertical direction,

may due to the coupling of guided resonant cavity mode to the vertical leaky/radiation mode[34]. On the other hand, in the defect-free PC cavity (H_0 , Figure 4.4(b)), there is a significant suppression in the transmitted power within the photonic bandgap (PBG) region. At a much reduced signal level (transmitted power), there is a peak near the bandedge ($1.41\mu\text{m}$). This could be due to the bandedge effect associated with the group velocity anomaly. The transmitted power for the reference sample (no PC case) is also shown in Figure 4.4(c).

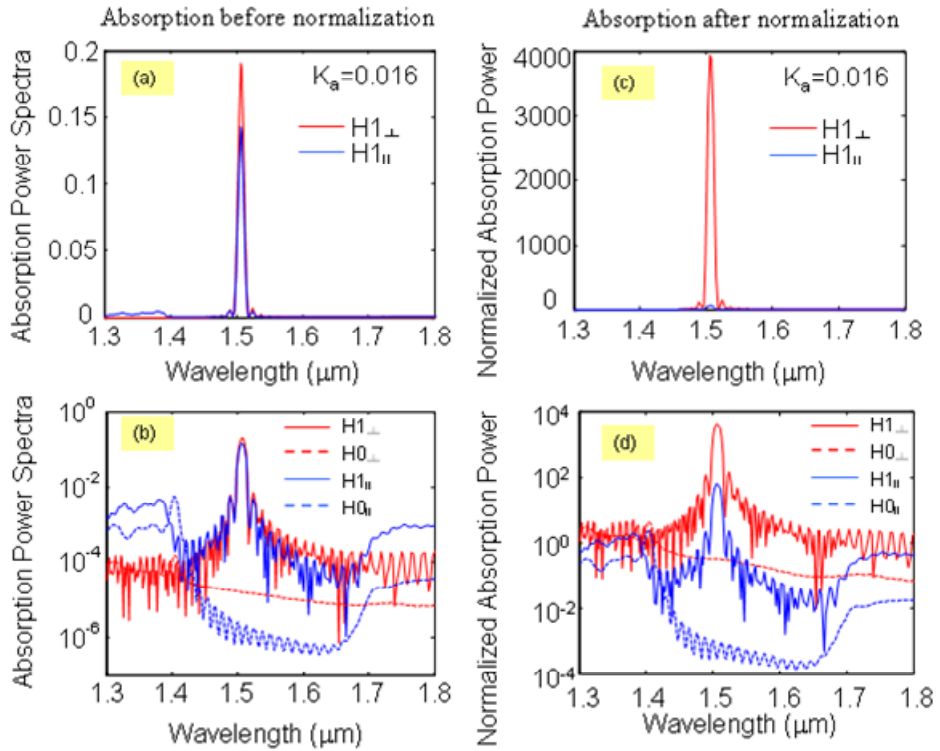


Figure 4.5 (a) Linear scale absorption of H_1 cavity (b) Log-scale absorption power spectra of both H_1 and H_0 (c) and (d) are value after normalization with respect to the reference sample (slab without PC) correspond to (a) and (b) respectively. $k_a = 0.016$ for all cases.

The absorption power was extracted from the monitored power difference at different absorption coefficients (varying k_a values) as shown in Figure 4.5(a) and (b). The normalized absorption, defined to be the ratio of the absorption in PC cavities to that value in reference slab without PC structures, were plotted in Figure 4.5(c) and (d), with both linear (c) for single defect (H_1) and log-scale (d), for single defect (H_1) and defect-free (H_0) PC cavities. It is also worth mentioning

that the defect mode quality factor Q is far from optimal. Defect mode cavity Q optimization[74, 75] is essential with much higher Q for the desired spectral selectivity for hyper-spectral imaging, or even ultra-spectral ($0.1\text{-}0.3\text{cm}^{-1}$ resolution) imaging applications.

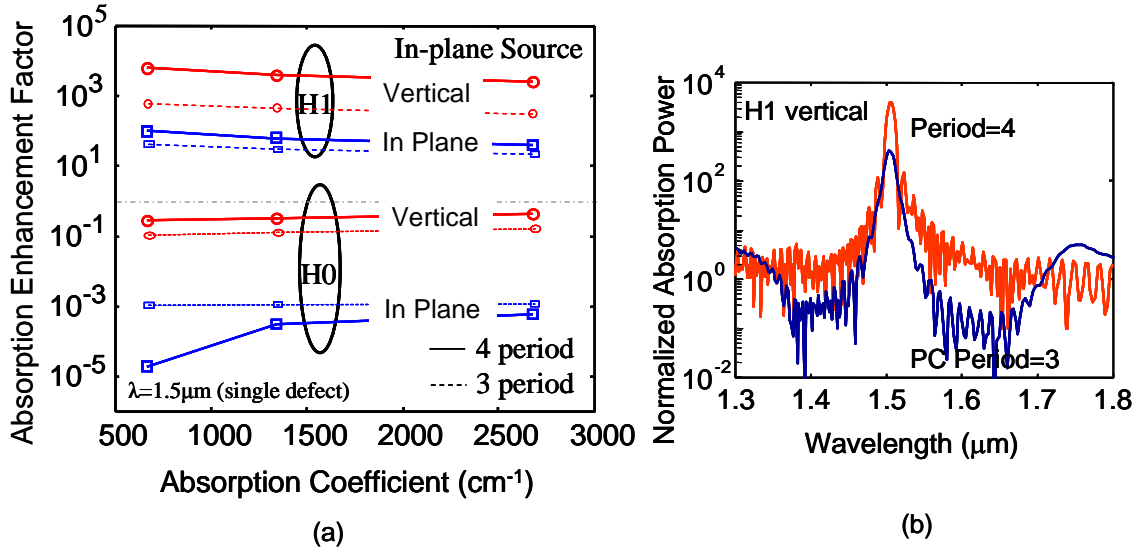


Figure 4.6 (a) Absorption enhancement factor for H_1 and H_0 cavity for different absorption coefficients and different surrounding air hole periods. Note the dominant absorption occurs along the vertical direction (top). (b) The impact of air hole period: normalized absorption power spectra for air hole periods of 4 and 3 in single defect H_1 cavity. Note the change in the enhancement factor (peak value) and corresponding reduction in the cavity Q .

The absorption enhancement factor, defined as the relative absorption power spectral density compared to that obtained from the reference slab (without PC) with the same absorption coefficient, can be derived from the normalized absorption power spectral density. The absorption change (absorption enhancement factor) due to the presence of the PC cavity is shown in Figure 4.6, at the defect-level wavelength ($1.5\mu\text{m}$), for different absorption coefficients. Enhanced absorption can be obtained with the enhancement factor around 6000 with $k_a=0.008$. The high enhancement factor can be obtained for a large range of absorption coefficients. The effect of air hole period surrounding the defect cavity was also investigated. As shown in Figure 4.6(b), with the reduction in the air hole period from 4 to 3, the enhancement factor also reduces

accordingly by a factor of 10 for vertical absorption in H_1 cavity, due to the corresponding reduction in the cavity quality factor Q which is defined as

$$Q = \lambda / \delta\lambda \quad (4.1)$$

Where λ and $\delta\lambda$ are the center resonant wavelength and the corresponding linewidth, respectively.

Shown in Figure 4.7 is the total cavity quality factor Q for this single defect cavity mode, which is derived from the simulated defect mode linewidth (e.g. Figure 4.5(a)), using equation 4.1, and reduction in Q was seen, as a result of increased absorption coefficient. Note the total Q relates to the in-plane $Q_{//}$ and vertical Q_{\perp} with this equation: $Q^{-1} = Q_{//}^{-1} + Q_{\perp}^{-1}$. Similar values were obtained for the total cavity Q based on both vertical and in-plane defect mode linewidths ($H1_{\perp}$, $H1_{//}$). It is also anticipated that much higher Q can be achieved with higher enhancement factor by increasing the surrounding air hole period and defect engineering (increasing $Q_{//}$), and/or heterostructure slab engineering for optical vertical confinement (increasing Q_{\perp}) [74, 75].

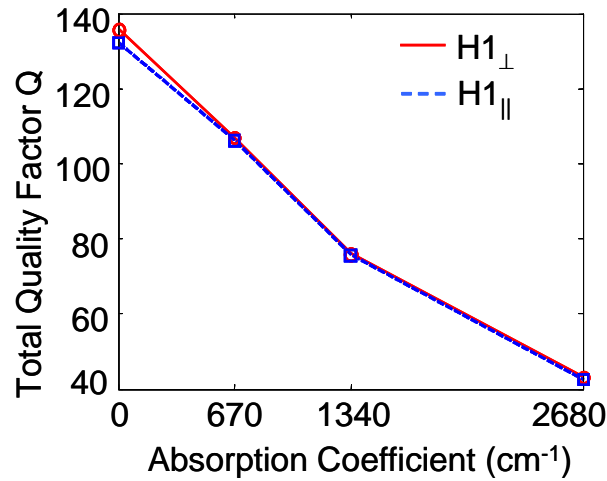


Figure 4.7 Total quality factor Q for the single defect cavity $H1$ ($H1_{\perp}$, $H1_{//}$) at different absorption coefficients

Further design optimization can lead to the shift in defect levels for desired absorption spectral selectivity with different absorption coefficients in single defect PC cavities (H_1). Shown

in Figure 4.8 are the absorption power spectra before and after normalization with respect to the reference sample (slab without PC) for different absorption coefficients. An increase in the absolute absorption was seen with the increase of the absorption coefficient. However, for the normalized absorption, the enhanced absorption was reduced with the increase of absorption coefficient. It could be due to high absorption also degrade the quality factor of PC defect cavity.

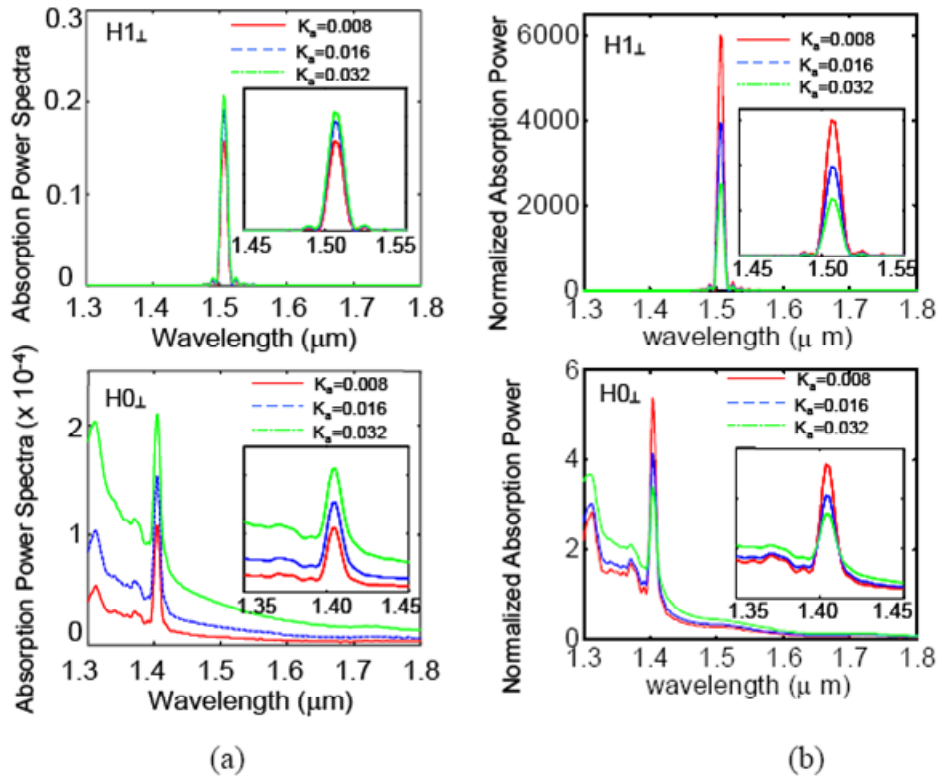


Figure 4.8 Absorption power spectra (a) before and (b) after normalization with respect to the reference sample (slab without PC) for different absorption coefficients. Note a reduction in normalized absorption at peak wavelength with the increase of absorption coefficient.

4.2 Vertical Source above 2D PCS

4.2.1. Simulation Setup

Following the similar procedure, the absorption characteristics were also investigated with a vertical source. The setup is shown in Figure 4.9. A small source was placed on top of the slab with excitation direction surface normal into the slab. The PCS structural parameters

kept the same as before. But the computation domain changed slightly to accommodate the memory requirement. The in-plane domain size was reduced from $10a$ to $8a$, where a is the PC lattice constant. The vertical direction was extended to $4a$, by increasing the air section thickness on both sides of the PCS from $0.35a$ to $1.6a$, to separate the vertical component from in-plane component. The vertical monitors (P_T , P_B) are placed further away from the slab accordingly. In this case, the transmitted power collected by the vertical monitor is less sensitive to the monitor location. Spatial grating size, $g_s=a/15$, is set along three direction. It is slight larger than grating size for in-plane source but still much smaller than the required value of $a/10$.

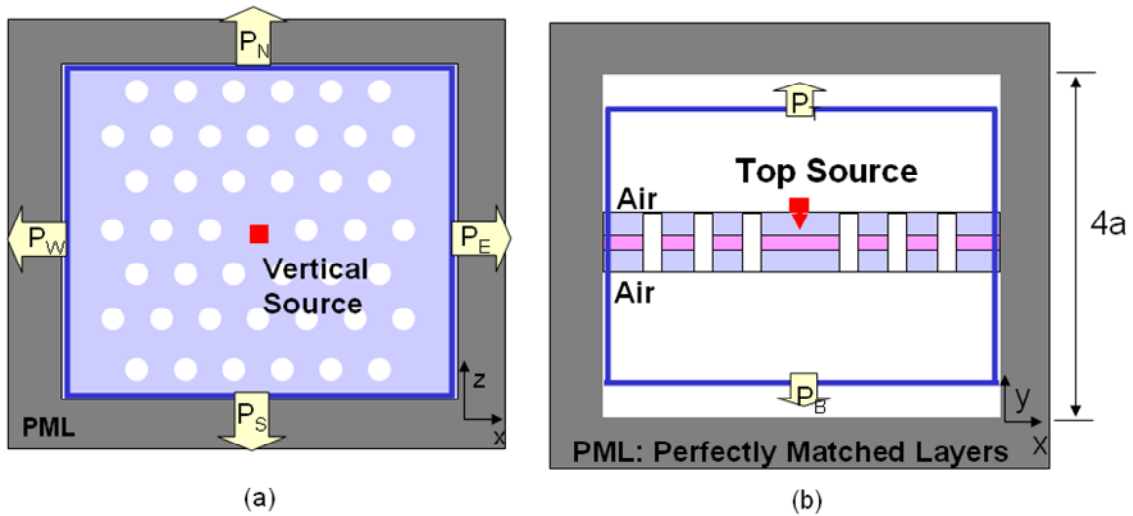


Figure 4.9 3D FDTD simulation setup with vertical dipole source location and launch direction shown. The relative locations for the vertical and in-plane monitors enclosing the entire simulation domain are also shown with blue lines, more details can be found in Table 4.3

Table 4.3 3D FDTD simulation setup for 2D PCS with vertical light source

Category	Parameter	Characterization
Globe	Computation Domain	$-1.35\mu\text{m} - 1.35\mu\text{m}$ in x $-2a - 2a$ in y $-1.15\mu\text{m} - 1.15\mu\text{m}$ in z
	Grid Size	$a/15$
	Time Step	Grid Size/2 (in unit of a/c)
	Computation Time	Time Step* 2^{14}
Source	Source Type	Gaussian
	Source Size	$0.12a \times 0.1a$
	Source Location	Center at $(0, 0.4a + 0.035, 0)$
Monitor	In-plane Monitor1 Size	$2.5\mu\text{m} \times (0.8a + 0.12) \mu\text{m}$

Table 4.3 – *Continued*

	In-plane Monitor1 Location	Center at (0,0,1.1)
	In-plane Monitor2 Size	2.5 μm x (0.8a+0.12) μm
	In-plane Monitor2 Location	Center at (0,0,-1.1)
	In-plane Monitor3 Size	2.2 μm x (0.8a+0.12) μm
	In-plane Monitor3 Location	Center at (1.25,0,0)
	In-plane Monitor4 Size	2.2 μm x (0.8a+0.12) μm
	In-plane Monitor4 Location	Center at (-1.25,0,0)
	Top Monitor Size	2.5 μm x 2.2 μm
	Top Monitor Location	Center at (0, 0.4a+0.06,0)
	Bottom Monitor Size	2.5 μm x 2.2 μm
	Bottom Monitor Location	Center at (0, -0.4a-0.06,0)
	Monitor Time	Time Step*10
PML	PML Size/Location	Enclose the whole computation domain
	PML Thickness	Grid Size *10

4.2.2. Absorption Enhancement

Following the similar procedure as the in-plane source case, the absorption characteristics were extracted for vertical source simulation. The monitor power (transmitted spectral density) was shown in Figure 4.10 (a), (b), (c), with $k_a = 0$ and 0.016, for single defect (H_1) PC cavity, defect free (H_0) PC cavity, and reference sample (REF: slab without PC), respectively. In the vertical source case, the dominant transmitted power was collected by in-plane power monitors (middle panel), as expected. This further confirms that the dominant absorption occurs along in-plane direction for the surface normal incident light, due to the waveguide coupling. For the single defect H_1 cavity, a distinctive peak also occurs at the defect mode level (1.5 μm). This behavior was also widely seen in microwave frequency region, as the frequency selective surface (FSS)[76]. Further exploration of these characteristics at optical frequency region can lead to novel device concepts, such as optical filters, switches and modulators.

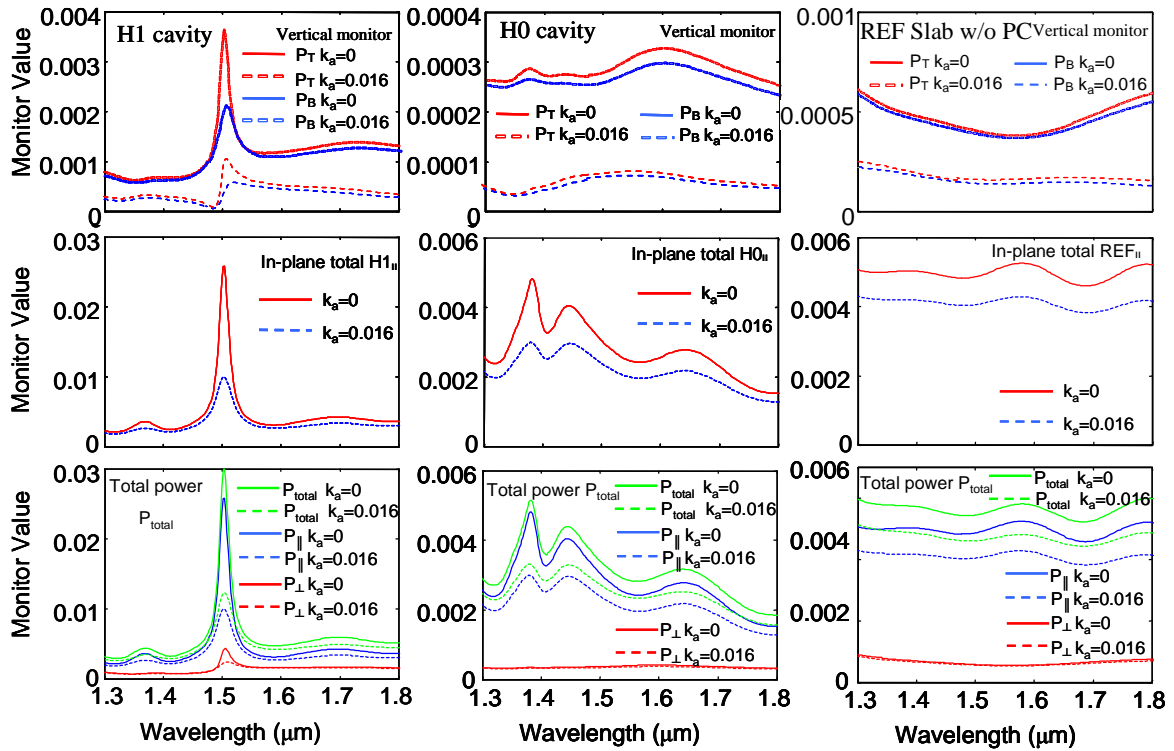


Figure 4.10 Vertical light source simulation on detected power densities from all monitors. Spectral power density based on the vertical and in-plane monitors in (a) single defect H_1 PC cavity; (b) defect-free H_0 PC cavity; and (c) reference slab without PC structure. Top panel shows vertical power middle panel shows in-plane power and bottom panel shows total power

Similar as the in-plane light source, the total transmitted power was obtained by adding up the values of the six monitors, which enclose the source and the entire simulation domain (including the PCS). The absorbed power was extracted by the subtraction of the total collection power (P_{total}) at $k_a=0$ and $k_a=0.016$ (shown in the bottom panel of Figure 4.10). The results were shown in Figure 4.11, for the total absorbed power at $k_a=0.016$, before and after normalization. Compared to the results obtained from in-plane source (shown in Figure 4.5), the enhancement in the absorption for the vertical source in H_1 cavity is significantly reduced by a factor of two orders. One of the major reasons could be due to the relatively small source we used here and the monitor power we are collecting, which includes the power both from the defect region as well as from the defect-free section from the entire PCS under simulation. Further work are needed to comprehensive understand this finding. The actual enhancement due to the single

defect section can be much higher, if we can separate out the results for the defect region and from the defect-free section, by the following three approaches: (a) Varying the source size; (b) Varying the monitor size; (c) Varying the defect configuration. Another feature worth to mention is that we do not see a significant suppression in the photonic bandgap region for defect-free PC cavity. For the 2D PCS it is well known that the photonic bandgap only exists in the in-plane direction, not in the vertical direction. However, we should anticipate a profound reduction in the PBG region due to the coupling and interaction of vertical source with the in-plane mode. This is another question to be answered.

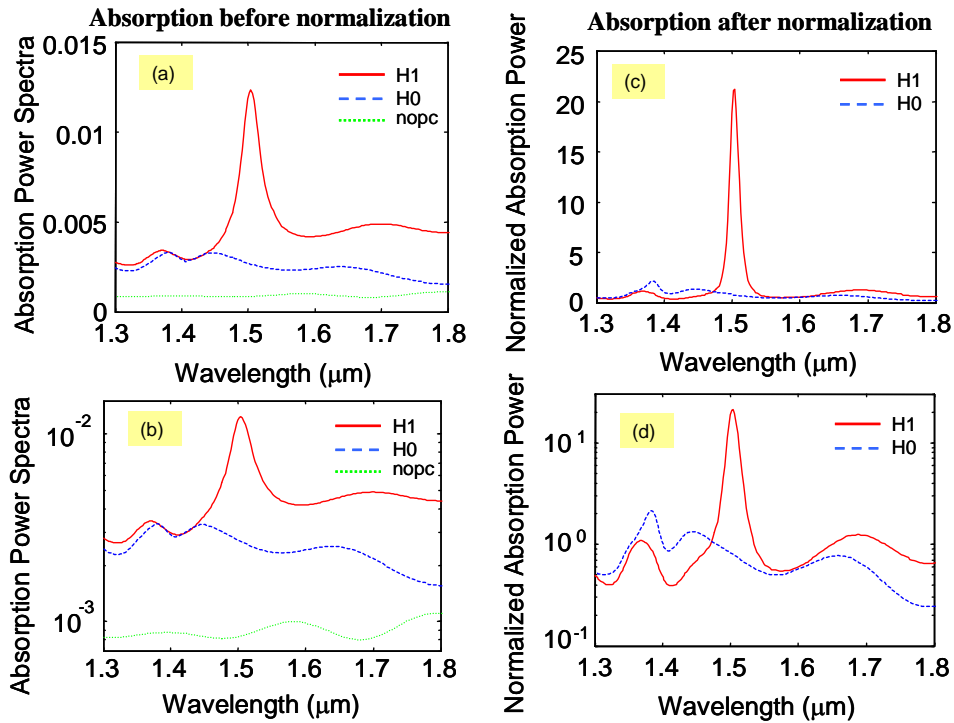


Figure 4.11 Absorption power spectra before normalization (a) (linear scale) and (b) (log scale) and after normalization (c) (linear scale) and (d) (log scale) with respect to the reference sample (slab without PC) for $ka=0.016$.

Shown in Figure 4.12 are the absorption power spectra before and after normalization with respect to the reference sample (slab without PC) for different absorption coefficient. Similar to the in-plane source case, a saturation/slight reduction in the enhanced absorption was found with the increase of absorption coefficient which could be due to poor quality factor of

PC cavity with high absorption as shown in Figure 4.13(a). The enhancement factor for different absorption coefficients was also plotted in Figure 4.13(b). Further work is needed to understand these unique features and to optimize the PC defect cavity for optimal performance.

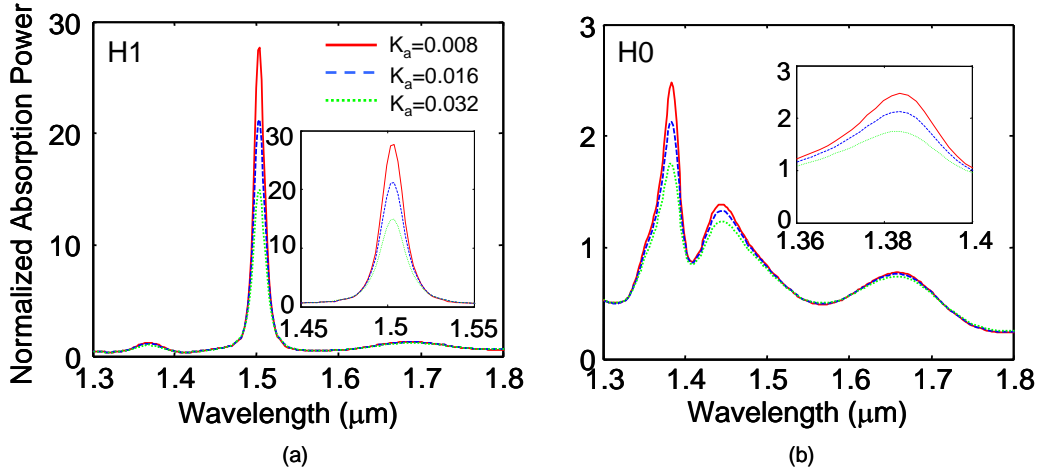


Figure 4.12 Absorption power spectra (a) before and (b) after normalization with respect to the reference sample (slab without PC) for different absorption coefficient. Note a reduction in normalized absorption at peak wavelength with the increase of absorption coefficient.

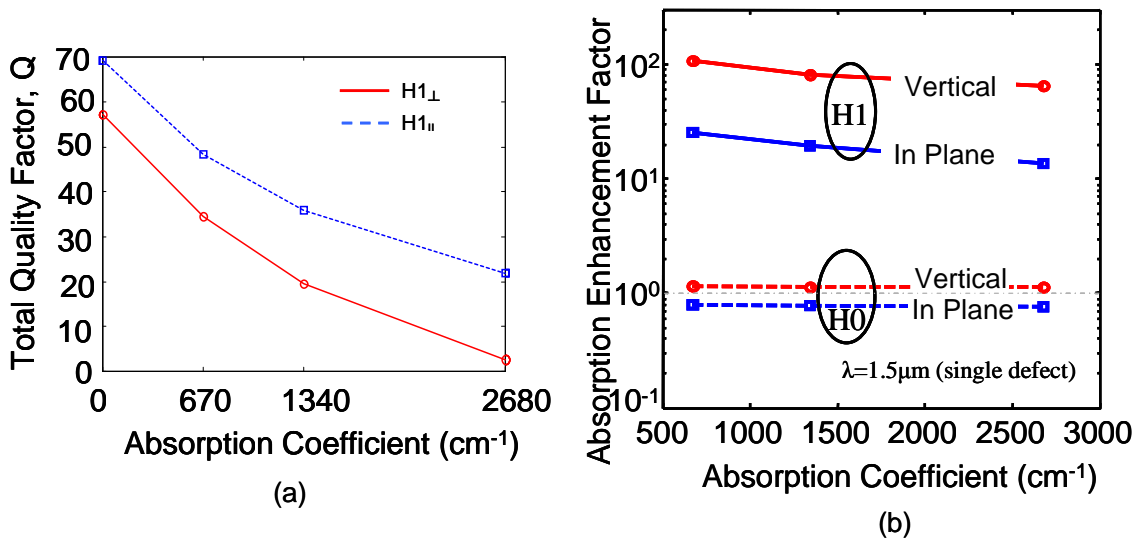


Figure 4.13 Vertical light source (a) total quality factor Q for $H1_{\perp}$ and $H1_{\parallel}$ (b) absorption enhancement and suppression factor result for H_1 and H_0 cavity for different absorption coefficients

In conclusion, theoretical investigation has been carried out on the spectrally selective absorption properties in 2D PCS cavities. The work is based on 3D FDTD technique. For 2D symmetric air hole triangular lattice PCS structures, enhanced absorption at defect level was obtained for both in-plane and vertical sources, with the enhancement factor largely dependent upon the source type and size. Complete absorption suppression within photonic bandgap region was observed in defect-free cavities and in single defect cavities when the absorption spectral band has no overlap with the photonic bandgap. The findings here can aid the cavity design in the infrared (IR) photodetectors with the incorporation of PC cavities. The incorporation of PC into IR photodetectors (e.g. quantum well and quantum dot infrared photodetectors) can potentially lead to IR photodetectors with higher operation temperature due to enhanced spectrally selective absorption. The spectral resolution and tunability can be accomplished through PC defect engineering. Further simulation on band edge and modeling multi-defects cavities is underway to help us further insight the absorption theory in photonic crystal slabs.

CHAPTER 5
INFRARED ABSORPTION WITH FANO RESONANCE

5.1 Fano Resonance in PCS

As briefly described in the chapter 1, Fano resonance has attracted great attention on photonic device applications. This Fano resonance effect has been investigated, both theoretically and experimentally, in PCS for filters[77-81], modulators[82, 83], sensors[84, 85], thermal radiation spectral and spatial control[86], broadband reflectors[87, 88], surface emitting lasers[89], bitable and other nonlinear optical devices[90, 91]. This chapter will first presents design and fabrication of Fano filter, then discusses transmission properties of transferred Fano filter. Finally investigates absorption characteristics for PbSe colloidal quantum dots in defect-free photonic crystal cavities, via Fano resonances.

5.2 Design and Fabrication of Fano Filters on Transparent Substrates

Fano Filter is designed with Rigorous coupled-wave analysis (RCWA) for target Fano resonance at 1550 nm, with square lattice air hole array distributed on the Si nanomembrances (SiNMs). The designed parameters of Fano filter are shown in Table 5.1.

Table 5.1 1550nm Fano filter design parameters

Parameter	Value
Lattice Constant a	0.6 μm
Air hole Radius r	0.19a
Thickness of Fano filter	260nm
Refractive index of Si	3.48
Refractive index of transparent substrate	1.5

The dotted blue curve shown in Figure 5.1(a) is the simulated transmission response of such a structure under surface-normal condition, which agrees very well with the measured

transmission spectra, with slight 3nm blue shift in the resonance locations. Care was taken to ensure that the fabricated device has the same lattice parameters (air hole radius r and lattice constant a). In order to fit the measured resonance locations, SiNM thickness was adjusted from the design value of 260 nm to the fit value of 250nm, within the thickness variation specifications from Soitec wafer datasheet. Excellent agreement was obtained between simulation and experiment. For all the simulations carried out in this work. All these structural parameters kept the same for the same device. Notice that strong oscillations in the simulated transmission spectra are due to the Fabry-Perot interferences caused by the truncated finite thickness of glass substrate during simulation.

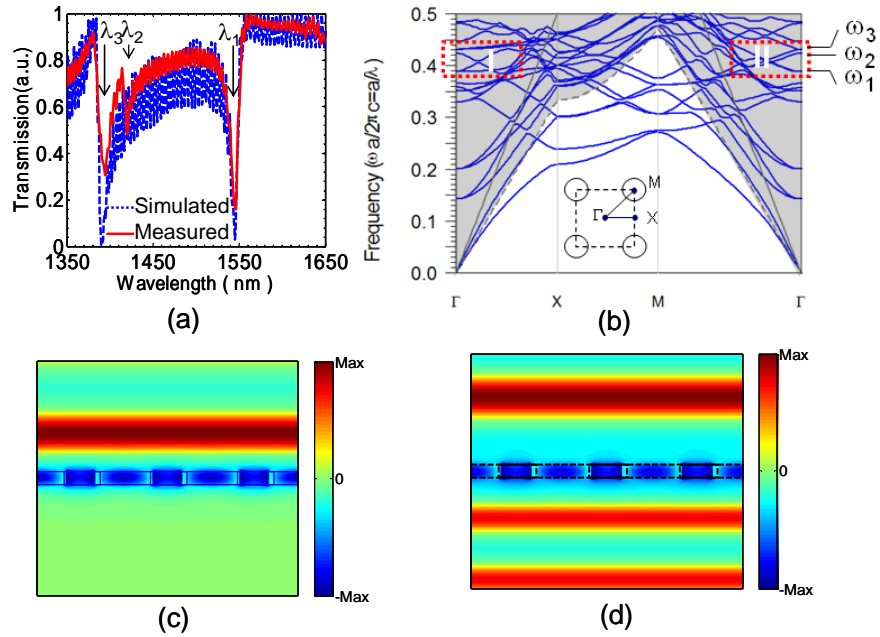


Figure 5.1 (a) Measured and simulated surface normal transmission spectra for the fabricated patterned SiNM Fano filters on glass substrates; (b) Simulated dispersion plot for Fano filters on glass substrates, where $r/a=0.19$, $t/a=0.25/0.6-0.417$. The refractive indices of silicon and glass are 3.48 and 1.5, respectively. Note the surface-normal transmission dips/peaks at all three wavelength points (λ_1 , λ_2 , λ_3) agree well with the dispersion plot ω_1 , ω_2 , ω_3 at Γ point. (c) and (d) The simulated snapshots of electrical field intensity profiles for on-resonance wavelength (λ_1) and off-resonances, respectively.

Comparing simulation and experiment, the differences in the quality factor and thus the Bloch mode lifetime[92] are small (<10%) as shown in Table 5.2. However, the transmission

contrast ratio seems to be large (4dB difference for spectra shown in Figure 5.1(a)). This could be due to our measurement error, as well as fabrication imperfections. Additionally, these three resonance modes can be correlated to the bandedge mode at the zone center (Γ point) for the surface-normal incident beams. Shown in Figure 5.1(b) is the simulated dispersion plot for the square lattice structure under testing, based on a plane wave expansion (PWE) technique. All the three dips obtained in the transmission spectra (λ_1 , λ_2 , and λ_3) agree well with the three modes obtained from the simulated dispersion plot, labeled as ω_1 , ω_2 , and ω_3 , respectively.

Table 5.2 Variation of bandwidth, quality factor and lifetime between simulation and fabrication

	Bandwidth(nm)	Quality Factor	Lifetime (ps)
Simulation	10.5	147.3	0.12
Experiment	11.5	134.5	0.11

The relationship between quality factor (Q) and Bloch mode lifetime (τ) is give by equation:

$$Q = \frac{2\pi c}{\lambda} \tau \quad (5.1)$$

The resonance modes were further verified with three dimensional finite difference time domain (3D FDTD) simulations. The snapshots of field propagation for both on- and off-resonance modes are shown in Figure 5.1(c) and (d), respectively. Note that, for the on-resonance mode (λ_1), the surface-normal incident light is bounced back from the patterned SiNM structure due to the coherence (in-phase) reflection, which leads to the dip in the transmission spectra. On the other hand, light at other spectra locations (off-resonance) can pass through the patterned SiNM Fano filter with its maximum transmission efficiency.

The spectral bandwidth and quality factor of the filter resonance can be further optimized to have either very high Q (>1,000), or very low Q (broadband), by design optimization, control of modal symmetry, choice of lattice configurations, and choice of lattice parameters. The choice in the fill factor, i.e., r/a ratio, can significantly alter the device

characteristics. As Shown in Figure 5.2, increase r/a value will shift the Fano resonance towards short wavelength region, degrade the quality factor Q , and therefore reduce the lifetime of Fano resonance modes τ . Typically, small fill factor can lead to high- Q narrow band filters, and larger fill factor can lead to broadband filters/reflectors[34].

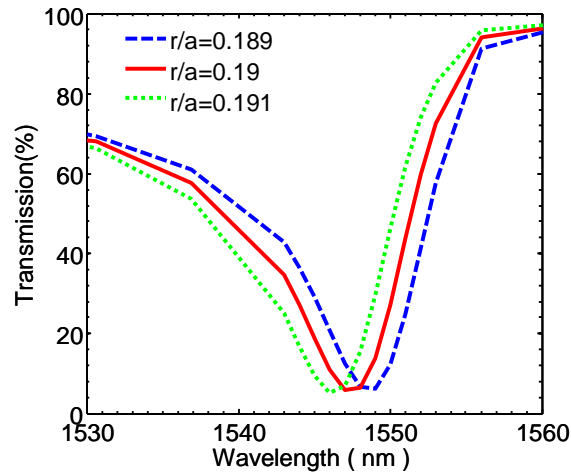


Figure 5.2 Fano resonance change from small variation of air holes

The whole fabrication and transfer procedure of Fano filter has been presented [93-95]. Here just briefly introduce as shown in Figure 5.3. The PC is first fabricated on the SOI wafer using a standard ZEP520A e-beam lithography technique and an HBr/Cl₂ chemistry based reactive-ion etching (RIE) process. Shown in Figure 5.3(a) are the scanning electron micrographs (SEM) of the fabricated PC patterns. The structure is immersed in aqueous diluted HF solution (49% HF: DI water ¼ 1:4) for several hours to etch away the BOX layer selectively (Figure 5.3(b)). Once the top patterned PC SiNM is completely released, it is rinsed in DI water and transferred onto a glass or a polyethylene terephthalate (PET) substrate, based on a modified wet transfer process. Shown in Figure 5.3(c) are the final micrograph of a 5mm x 5mm patterned SiNM piece transferred onto a 1"x1" glass slide and PET substrate. It is worth noting that an optional SU8 coating on the glass may be used for improved adhesion and mechanical stability for the final device structure.

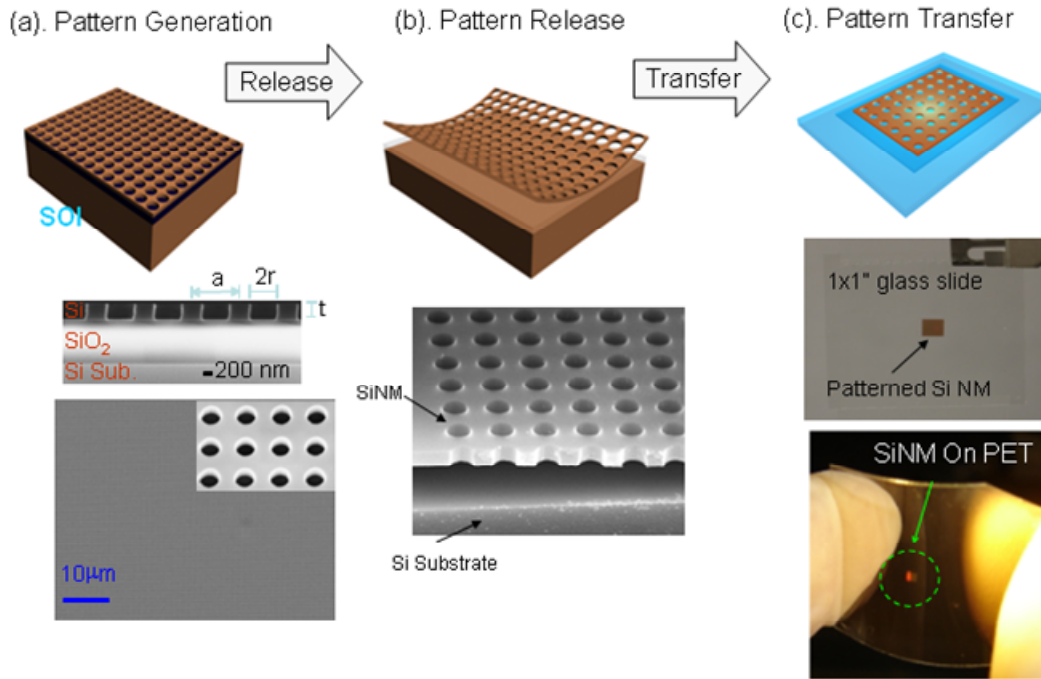


Figure 5.3 Fano filter fabrication procedure (a) pattern generation by e-beam lithography and RIE (b) pattern release by BHF etching (c) wet pattern transferring to obtain Fano filter on transparent substrates

5.3 Angular and Polarization Dependent Transmission on Transferred Fano Filters

The experiment is conducted with an unpolarized and focused broadband QTH (quartz tungsten halogen) lamp source (the transmission setup will be shown in Figure 5.14 (b) in the next section). The focused beam size is $\sim 150 \mu\text{m}$ in diameter, much smaller than the 2-5 mm patterned device area, but sufficiently larger than the lattice constant a of $0.6 \mu\text{m}$. The measured transmission spectrum of SiNM was obtained by normalizing the measured transmission spectral intensity data for Fano filters to the data for the glass substrate (reference). At certain spectral locations, close to 100% transmission was obtained. A dominant dip was observed at the target wavelength of 1547 nm (denoted as λ_1) and other two dips were observed at around 1417 nm (λ_2) and 1393 nm (λ_3), respectively.

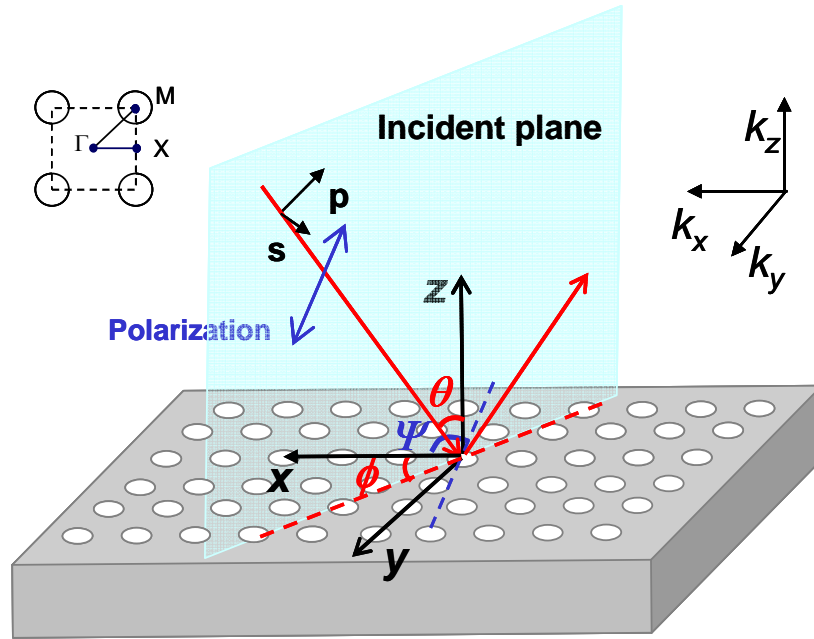


Figure 5.4 Angle and polarization definition for incident light beam onto patterned SiNM Fano filters. The PC lattice and Brillouin zone symmetric points (Γ , X and M) in the k -space are also shown in the inset.

Detailed investigations were carried out on the angular- and polarization-dependent transmission characteristics for this type of Fano filters on glass substrates. As shown in Figure 5.4, the light incident direction is defined by two polar angles, the colatitude angle θ (angle from the surface-normal direction) and the azimuth angle $\phi_{||}$ (angle from the positive x -axis to the orthogonal projection of the incident beam in the x - y plane). The incident polarization (E-vector) angle Ψ is defined as the angle from the positive x -axis to the projection of polarization direction in the x - y plane. Following a conventional definition, typical s- or p-polarizations are defined as the beam with E-vector perpendicular or parallel to the incident plane formed by the incident light and reflected light, i.e., $\Psi = \phi$ for p- (TM-like) polarization and $\Psi = \phi + 90$ for s- (TE-like) polarization. Also shown in Figure 5.4 are the conventional definition of wavevector directions and the corresponding Brillouin zone in k -space with high symmetric points defined with Γ , X and M , respectively. Due to the high symmetric properties of the square lattice in the device, only three special cases are needed to consider: (5.3.1) Surface-normal without and

with polarizations ($\theta = 0^\circ$, varying ϕ , at Γ point in k -space); (5.3.2) With incident beam plane parallel to x - z plane ($\phi = 0^\circ$, varying θ , along Γ - X direction in k -space); and (5.3.3) With incident beam plane 45 degree off x - z plane ($\phi = 45^\circ$, varying θ , along Γ - M direction in k -space).

5.3.1. Surface-Normal Incidence

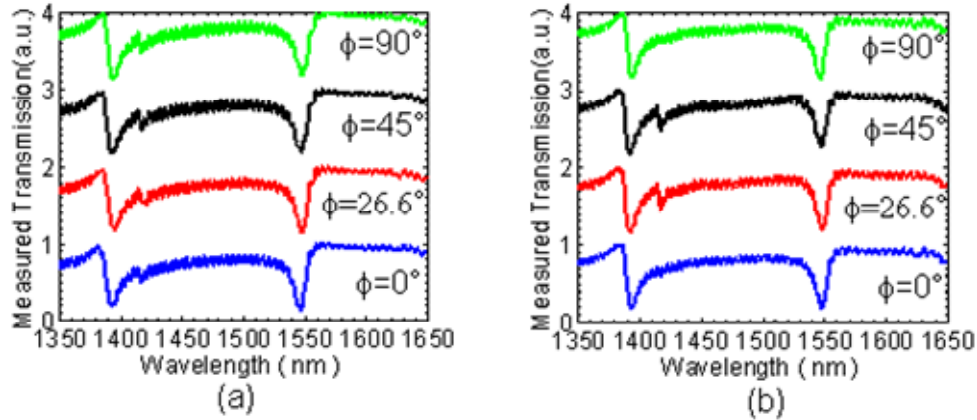


Figure 5.5 Measured surface-normal transmission spectra at different angles ϕ for the incident beam either (a) without polarizer; or (b) with polarizer fixed at $\psi = 0$

First, the transmission properties for surface-normal incident conditions is investigated, with $\theta = 0^\circ$. The measurement results are shown in Figure 5.5, for different angles ϕ , as defined in Figure 5.4. The polarization of incident beam is controlled by inserting a linear polarizer between the broadband light source and the objective lens in front of the test sample.

The results shown in Figure 5.5(a) and Figure 5.5(b) are for two cases without polarizer and with polarizer, respectively. Similar to the work reported earlier on free-standing filters and on flexible plastic PET substrate, very little spectral shifts were observed on the transmission spectra for all the three Fano resonant modes. The angle (ϕ) and polarization (Ψ) independent transmission characteristics at $\theta = 0^\circ$ are the results of the high symmetry of the circular-air-hole square lattice. Again the small variations on the measured transmission efficiencies could be related to the measurement error associated with fabrication imperfection of the lattice during the SiNM transfer processes.

5.3.2. Incident Beam Plane Parallel with x-z Plane (Γ -X direction)

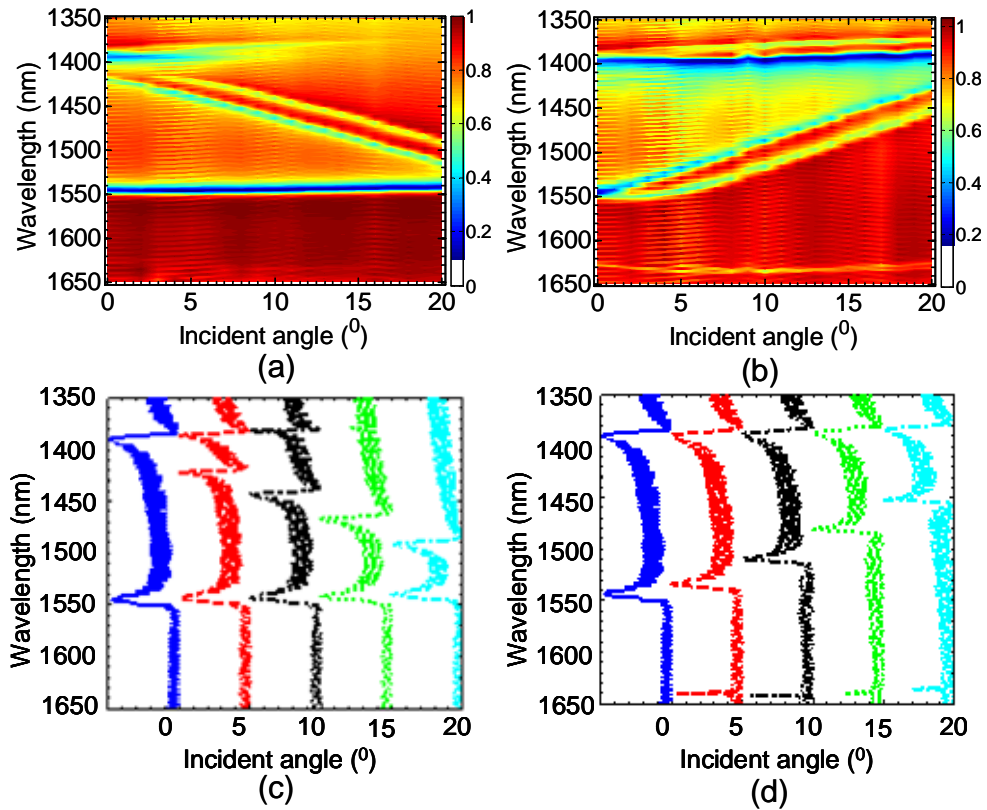


Figure 5.6 Measured transmission intensity contour plots under different polarization conditions (a) Γ -X direction with p -polarization light (b) Γ -X direction with s -polarization light; (c, d) Simulated transmission spectra under p - and s -polarizations, respectively.

In this case, the incident beam is restricted to be within the plane in parallel with the x-z plane, i.e., kept at $\phi = 0^\circ$. This corresponds to the Γ -X direction in the k-space. The measured transmission spectra intensity contour plots for different incident angles (θ) are shown in Figure 5.6(a) and Figure 5.6(b) for the p - and the s -polarized incident beams, respectively. The simulated transmission spectra, based on the RCWA technique, are shown in Figure 5.6(c) and Figure 5.6(d), with the simulation parameters and test conditions matching with the measurement results shown in Figure 5.6(a) and Figure 5.6(b), respectively. Notice that the plots for the simulated spectra are rotated in order to have a better visual comparison between the experimental results and the simulation results.

When the incident beam is p-polarized (TM-like), i.e., the electrical vector direction lies in the plane that is in parallel with the incident beam plane, the dominant Fano resonant mode ($\lambda_1 = 1547$ nm transmission dip at $\theta = 0^\circ$) has very little spectral shift over the range of angles measured (from 0° to 20°). On the other hand, the other two modes show strong angle dependent behavior. The mode at λ_2 shifted towards longer wavelengths, from 1420 nm at $\theta = 0^\circ$ to 1500 nm at $\theta = 20^\circ$, at a constant rate of 4 nm/degree. The mode at λ_3 (1394 nm at $\theta = 0^\circ$) shows very small angle dependence for small incident angles (from 0° to 10°). But it is completely suppressed for larger incident angles ($\theta > 15^\circ$). The simulation results shown in Figure 5.6(c) also agree very well with the measurement results shown in Figure 5.6(a).

However, for s-polarized (TE-like) incident beam, the dominant Fano resonance mode (λ_1) shifted towards shorter wavelengths (Figure 5.6(b, d)), from 1547 nm at $\theta = 0^\circ$ to 1448 nm at $\theta = 20^\circ$, at a constant rate of 5 nm/degree. But the mode at the short wavelength (λ_3) has very weak angle dependence, with a small blue-shift less than 10nm, or 0.5 nm/degree when increases the incident angle $\lambda_{||}$ from 0° to 20° . Also notice that there is no dip observed at the λ_2 location in this case.

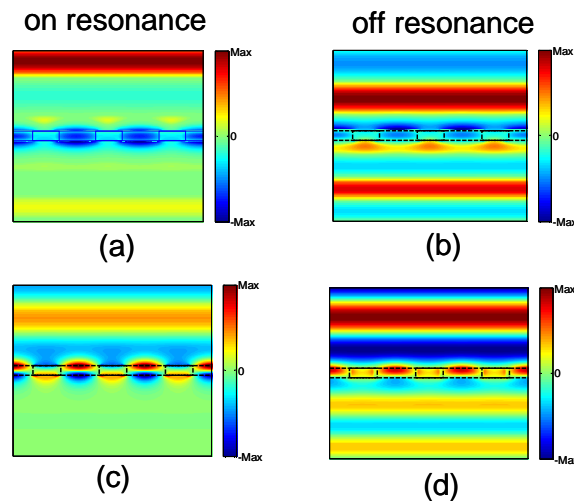


Figure 5.7 Snapshots of electric field distributions of Fano filters at large incident angle ($\theta=20^\circ$ and $\theta = 0^\circ$): (a) p-polarization, on-resonance; (b) p-polarization, off-resonance; (c) s-polarization, on-resonance; and (d) s-polarization, off-resonance.

The polarization dependent behavior for Fano resonances was further investigated with the modal propagation simulation based on a 3D FDTD technique. The simulated snapshots of the propagating electrical fields for the dominant Fano resonance (λ_1) are shown in Figure 5.7 for the p- and s-polarized incident beams, with angled incident beam $\theta=20^\circ$ and $\theta=0^\circ$. From Figure 5.7(a), the guided resonant mode within the patterned SiNM slab region is an even mode (symmetric) with respect to the propagating (-z) direction, similar to the field shown in Figure 5.7 (c) under the surface-normal incident beam condition. These modes (λ_1) seem to have less angle-dependent transmission properties, most likely related to the relatively-unchanged phase-matching conditions for on-resonance, associated with the relatively flat modal dispersion properties. On the other hand, for the s-polarized incident beam, as shown in Figure 5.7 (c), the guided resonance mode is an odd mode (asymmetric) with respect to the propagating (-z) direction. Changes in the incident angle (θ) may lead to large changes in the spectral location of resonance due to the change in phase matching conditions.

In addition to p- and s-polarizations, incident beams with hybrid polarization ($\Psi=45^\circ$) was also considered. The measured transmission intensity contour is shown in Figure 5.8(a). The dominant Fano resonant mode with $\lambda_1 = 1547$ nm at $\theta=0^\circ$ splits into two separate degenerate modes for larger incident angles, with one mode remaining at the same spectral location (p-polarization, Figure 5.6(a), also confirmed later) and the other shifting towards shorter wavelengths (s-polarization, Figure 5.6(b)). This result agrees very well with the data shown in Figure 5.6 for both the p- and s-polarized modes. In addition, with the increase of the incident angle, the resonant mode at λ_2 shifts towards longer wavelengths, and the resonant mode at λ_3 remains almost unchanged.

It is worth pointing out that such a diagonal polarization light should have both s- and p-polarization components. Therefore, in theory, it is expected that similar transmission results should be generated even from an unpolarized incident beam. This is indeed the case, as shown in Figure 5.8(b), which exhibits very similar characteristics as the one shown in Figure

5.8(a). The results match very well with the simulated transmission spectra based on the RCWA technique, as shown in Figure 5.8(c).

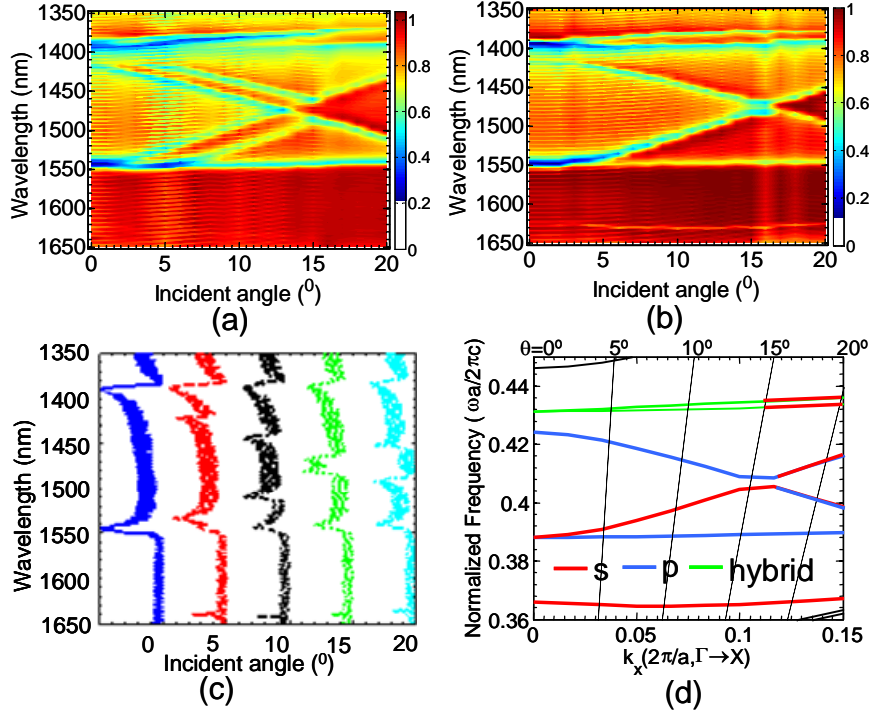


Figure 5.8 Measured transmission intensity plots for incident beam lies within x-z plane (along Γ -X direction) with (a) hybrid polarization ($\psi=45^\circ$) and (b) without polarization. (c) Simulated transmission with the same conditions shown in (a). (d) Dispersion plot along Γ -X shown the p- and s-polarization states.

Further analysis was carried out to correlate the measured transmission spectra with the Fano resonant mode based on dispersion plot shown in Figure 5.1(b). Following a similar process reported earlier, a correlation was found between the incident angle θ and the wavevector k , with $k_{\Gamma-X} = (\frac{a}{\lambda}) \sin \theta$. The corresponding dispersion plot is shown in Figure 5.8(d), which is the zoom-in plot of the region I shown in Figure 5.1(b). The corresponding p-, s- and hybrid polarized modes are shown with different colors. An excellent agreement between the measurement data and the simulation results has been obtained, which also confirms the earlier analysis on the transmission spectra.

5.3.3. Incident Beam Plane 45 Degree off x-z Plane (Γ -M direction)

Finally, Transmission characteristics for the incident beam 45 degree off the x-z plane, i.e. $\phi = 45^\circ$ is measured. This is another high symmetry direction, which corresponds to the Γ -M direction in the k-space. The measured transmission intensity contours, along with the simulated transmission spectra, for both the p- and the s-polarized beams, are shown in Figure 5.9. Again, the simulation results agree very well with the measured transmission results. For the dominant resonant mode at λ_1 , the transmission spectra shift towards shorter wavelengths for both the p- and the s-polarized beams. For the other mode at λ_2 , shift is only seen with s-polarized beam, differing from the results shown in Figure 5.6, where shift is only seen with p-polarized beam. In both cases, the transmission spectra shift towards longer wavelengths. For the mode at λ_3 , it shifts towards shorter wavelengths or longer wavelengths for p- or s-polarized beams, respectively.

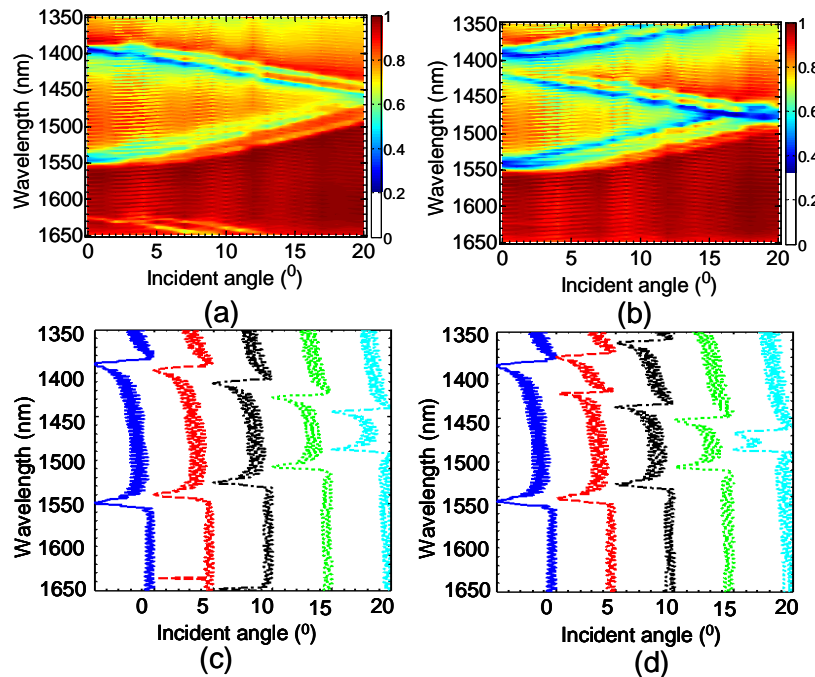


Figure 5.9 Measured transmission intensity contour plots under different polarizations (a) Γ -M direction with p-polarization light (b) Γ -M direction with s-polarization light; (c) Simulated transmission spectra with p-polarizations; and (d) (c) Simulated transmission spectra with s-polarizations.

Following a similar procedure, the measured transmission intensity contour for the hybrid polarization with ($\psi = 45^\circ$) is shown in Figure 5.10(a), along with the simulated transmission spectra shown in Figure 5.10 (b). The two sets of results agree very well with each other. The specific modal properties can be further explained with the dispersion plot, as shown in Figure 5.10 (c), for the wave vector along the Γ -M direction, which corresponds to the Region II shown in Figure 5.10 (b). Again, different polarization modes can be identified, by correlating the measured transmission spectra with the simulated dispersion curves.

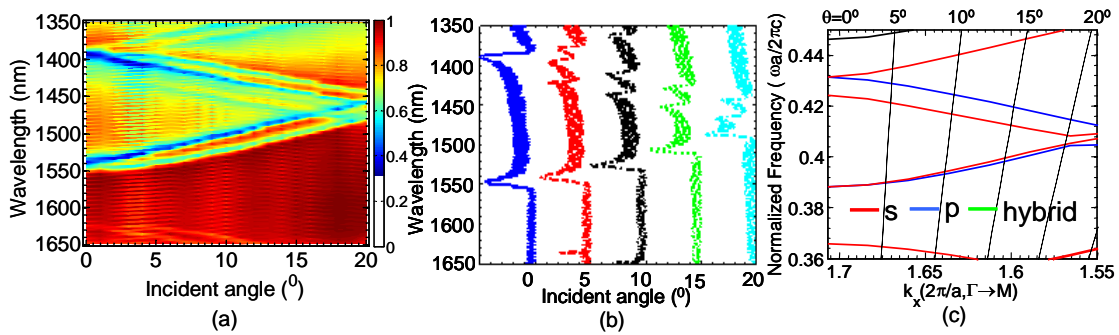


Figure 5.10 (a) Measured transmission intensity contour plots for incident beam lies at 45 degree off x - z plane (Γ - M direction) with hybrid polarization ($\psi=45^\circ$). (b) Simulated transmission spectra for different incident angles with the same incident beam orientation and polarization shown in (a). (c) Dispersion plot along Γ - M direction shown both p - and s -polarization states.

5.3.4. Filter Transmission Contrast Ratio

One of the key parameters in the filter design is the filter transmission contrast ratio, which is defined as the ratio of transmission intensities at pass and block (resonance dip) bands. Summarized both simulation and experimental results are shown in Figure 5.11, based on the data presented in Figure 5.6, Figure 5.8, Figure 5.9, and Figure 5.10 before. The simulated transmission contrast ratio varies from 14dB to 38dB, for both s - and p -polarizations. However, for the hybrid or unpolarized beams, the simulated transmission contrast ratio is substantially reduced to 4-20dB, despite an excellent agreement was observed in the spectral location and spectral shift behaviors shown earlier. These results suggest that these filters are better suited for polarized incident beam applications, with high transmission contrast ratios. It

can be designed for unpolarized or hybrid-polarized beams, provided the lower transmission contrast ratio is acceptable.

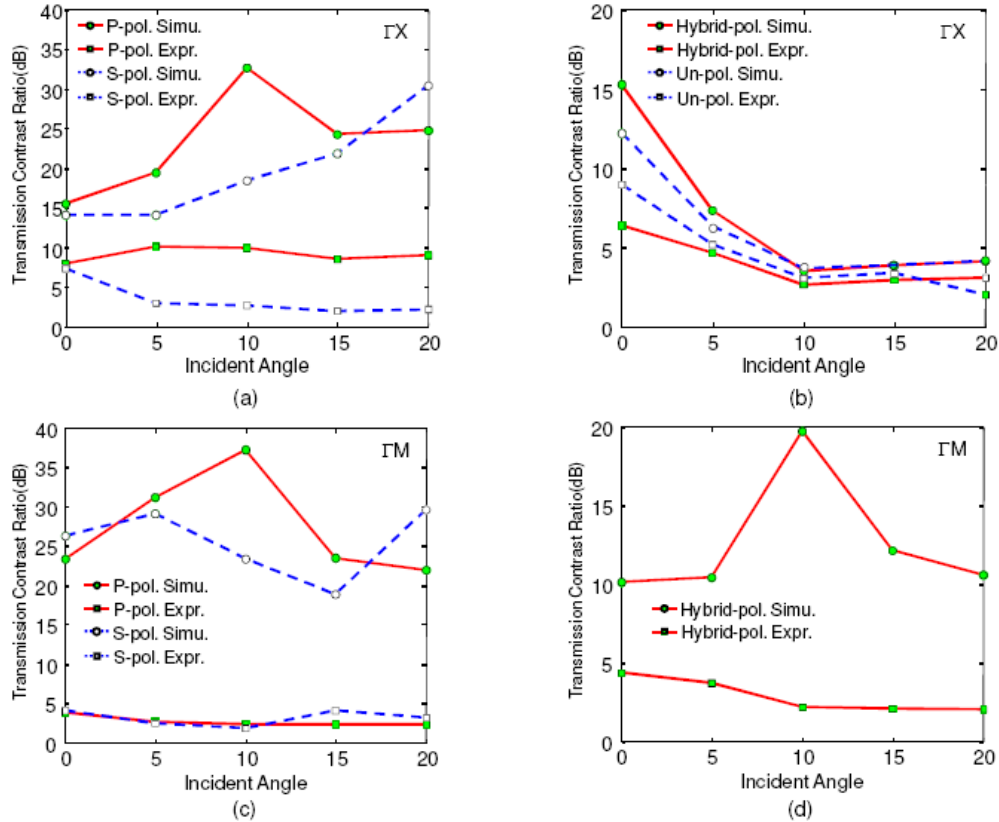


Figure 5.11 Comparison of the simulated (Simu.) and experimental (Expr.) transmission contrast ratios for the dominant resonant modes for beam along: (a) ΓX direction for p- and s-polarizations (Figure 5.6); (b) ΓX direction for hybrid-polarization and un-polarized beams (Figure 5.8); (c) ΓM direction for p- and s-polarizations (Figure 5.9); and (d) ΓM direction for hybrid-polarizations (Figure 5.10)

Also notice that the measured contrast ratio is constantly much smaller than the simulated one. Such performance degradation could be contributed both to the device imperfections in the structures fabricated, as well as to some test limitations/variations associated with the experimental setup. Notice a broadband white light source (QTH lamp) and a focus objective lens are used here to obtain the desired small beam size for testing. In this case, the focused beam size on the device area is relatively large, $\sim 150 \mu\text{m}$ in diameter (i.e. ~ 150 periods of air hole area of filters) for device pattern area of $1000 \mu\text{m}$ or above. It is

anticipated that the real device size will be in the order of 10-100 μm . With a wideband tunable laser source, a much smaller beam size (e.g. 10-50 μm) can be obtained, which can measure the actual cavity Q for a device area of 10-100 periods of air holes. A better agreement between the measurement and the simulation may be obtained due to potentially smaller lattice variations. The measured transmission contrast ratio can approach the simulated one.

5.3.5. Spectral Engineer from Bending

Another Fano filter sample with Fano resonance located at 1560nm were used for bending test. Keeping the sample along ΓX direction and bending the sample to different curvature, k . Couple of nanometer blue shift is found in Fano resonance for p-, s- and hybrid-polarization as shown in Figure 5.12 (a)-(c). It is worth to note that in our experiment, the curvature of bended Fano filter sample is very small ($k=0.0017$ and 0.0034), much large tunable spectra shift can be expected from more bending forces on transferred Fano filters.

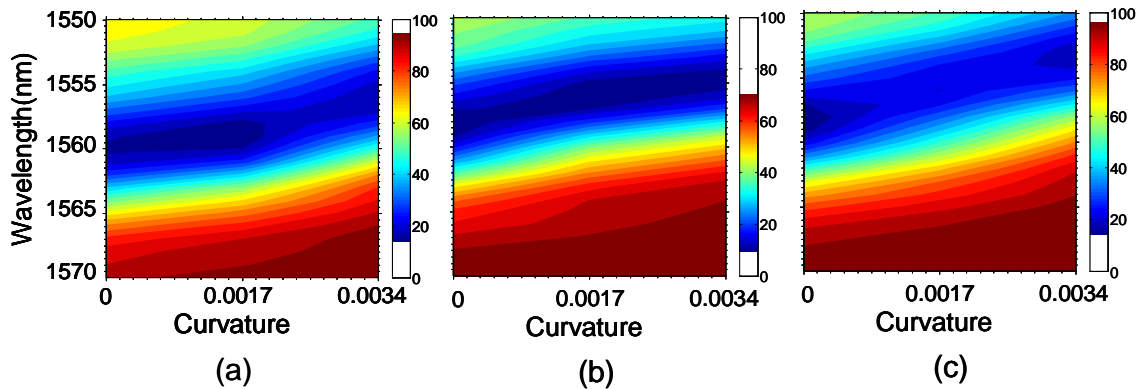


Figure 5.12 Measured transmission intensity map of Fano filter with dominant Fano resonance at 1560nm under different bending curvature with (a) p-polarization (b) s-polarization and (c) hybrid-polarization.

5.4 Absorption of PbSe/PbS Colloidal Quantum Dots (CQDs) in Fano Filters

5.4.1. Direct Absorption Measurement

By incorporating dispersive medium inside Fano resonance cavities, it is feasible to realize ultra-compact infrared photodetectors with spectrally-selective absorption enhancement

properties on any substrates for any wavelengths. This section discusses direct absorption measurements on colloidal QDs in Fano filters that are transferred to transparent substrates.

The Fano resonance filter structure was designed and fabricated on a silicon-on-insulator (SOI) substrate as described in the previous section. Shown in Figure 5.13(a) and Figure 5.13 (b) are the top view scanning electron micrographs (SEM) without and with CQDs, respectively, for the fabricated PC structures on the SOI. The thickness of the top Si NM PC layer (t) is 250 nm. The square-lattice air-hole PC structure has a period (a) of 600 nm, and the air hole radius (r) of 114 nm. Shown in inset of Figure 5.13 (b) is a transmission electron micrograph (TEM) image of nanocrystal PbSe CQDs used here. PbSe CQDs were synthesized with a noncoordinating solvent technique[96], with the target wavelengths covering different Fano resonance regions, ranging from 1450 nm to 1600 nm which is shown in Fig (c).

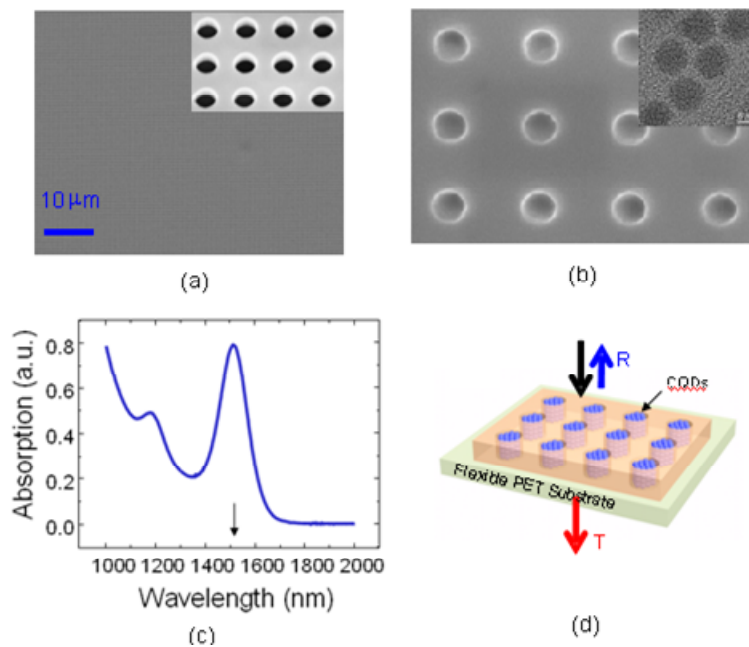


Figure 5.13 SEM of Fano filter (a) Before (b) After PbSe CQDs deposition by drop casting. TEM of QDs is shown in inset (c) Typical absorption spectrum of PbSe QDs (d) Schematic of SiNM based Fano filters filled with CQDs on flexible substrates. Surface normal optical measurement is also shown for both transmissions (T) and reflection (R).

Optical measurement on Fano filter filled with CQDs is schematically shown in Figure 5.13(d), where transmission/reflection measurements are carried out along the surface-normal direction.

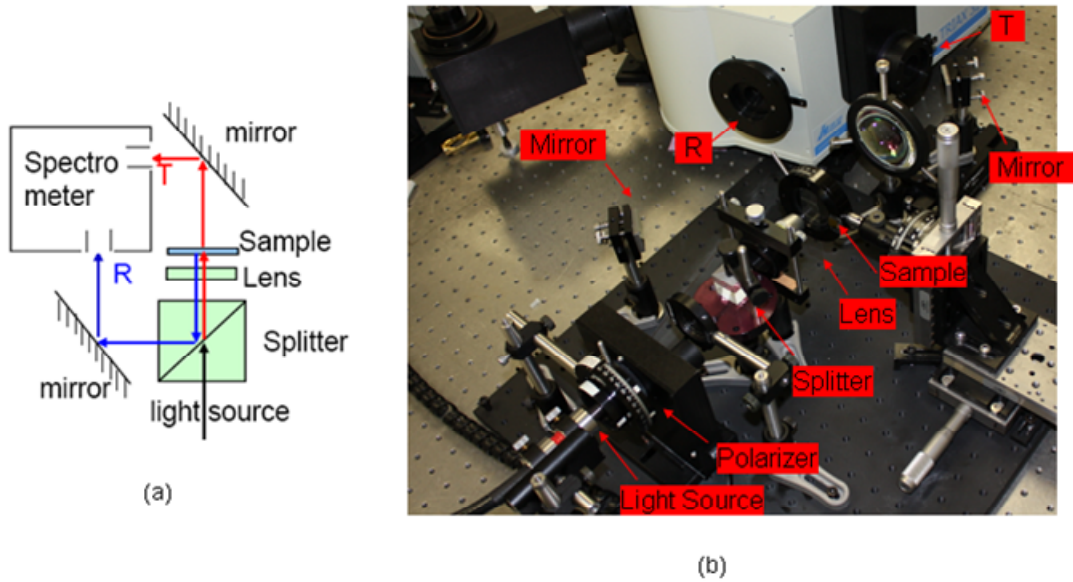


Figure 5.14 (a) Schematically show (b) Real image of simultaneous transmission and reflection experimental setup for Fano filter.

As shown in Figure 5.14(b). A focused broadband light source was generated from a quartz tungsten halogen (QTH) lamp. The beam transmitted through the Fano filter sample was collected by one entrance slit of a spectrometer, and the beam reflected from the sample was sent to the other entrance slit via a beam splitter. The measured transmission spectrum (T) was obtained by normalizing the measured transmission spectral intensity data for the Fano filters to that for the background (air). The measured reflection spectrum (R) was obtained by normalizing the measured reflection spectral intensity data for the Fano filters to that for the reference mirror (gold coated), which has a reflection around 97% at interested region. Care was taken to ensure the simultaneous measurements of the absolute transmission and the reflection spectra for the sample, under exactly the same conditions. In this case, the absolute absorption (A) can be derived based on the equation $A=1-T-R$.

5.4.2. Principle of Absorption Enhancement

Shown in Figure 5.15 are a set of measured transmission/reflection spectra for the Fano filters without and with CQDs. At the spectral regime of interest (around 1550 nm), the absorption due to Si is negligible, i.e., $A=0$. So all measured absorption is largely associated with the absorption of the incorporated CQD. A distinctive feature shown in Figure 5.15 is the spectral red-shift when incorporating CQDs, with the peak resonance shifted from 1547 nm to 1550 nm. This is due to the increase of the effective index in the air hole region of the patterned Fano filters. Based on the RCWA simulations, the effective index within air holes (n_h) of the patterned SiNMs was determined to be 1.09, corresponding to a 4% fill factor of CQDs.

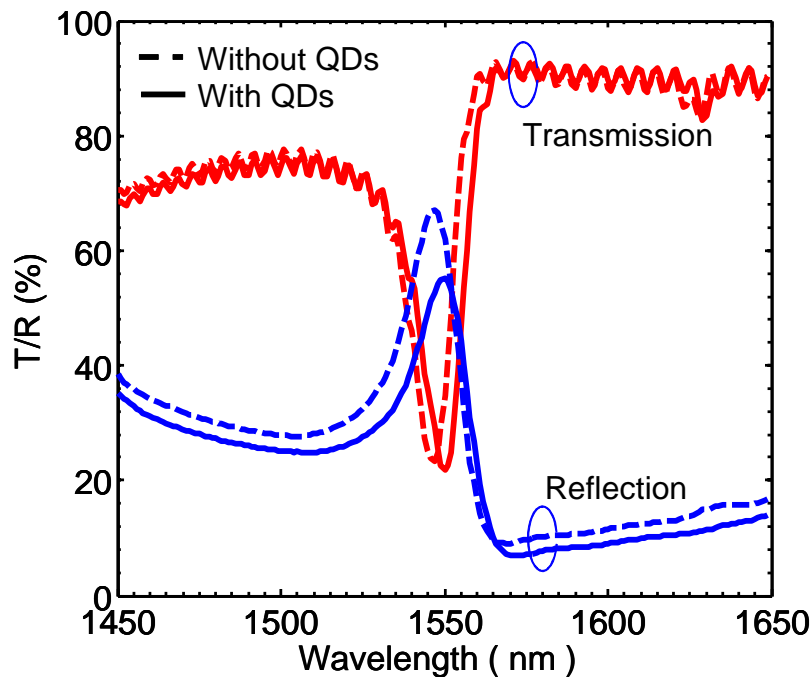


Figure 5.15 Measured transmission and reflection spectra for Fano filter without and with PbSe CQDs

After CQDs deposition, the measured transmission intensity of the resonance mode was reduced by 6.2% and the quality factor (Q) of the Fano resonance was degraded by 8.6%. This also agrees well with the RCWA simulated Q -factor degradation of 5.1%. On the other hand, the measured reflected intensity at Fano resonance was significantly reduced by 18%.

The Q-factor was significantly degraded by 17%. Both of these distinctive features in the measured transmission/reflection spectra agree well with the simulation results.

The absorption data for the Fano filter was directly extracted from the transmission and the reflection based on the equation $A=1-T-R$, where A, T and R are absorption, transmission and reflection, respectively. The measured absorption spectrum was shown as the dash line in Figure 5.16, where we found a sharp peak at the shifted Fano resonance regime (1550 nm). The simulated absorption spectrum was also shown in Figure 5.16 (solid line), with the fitting extinction coefficient (k) shown in the inset of Figure 5.16. The measured and the simulated spectra match very well with each other.

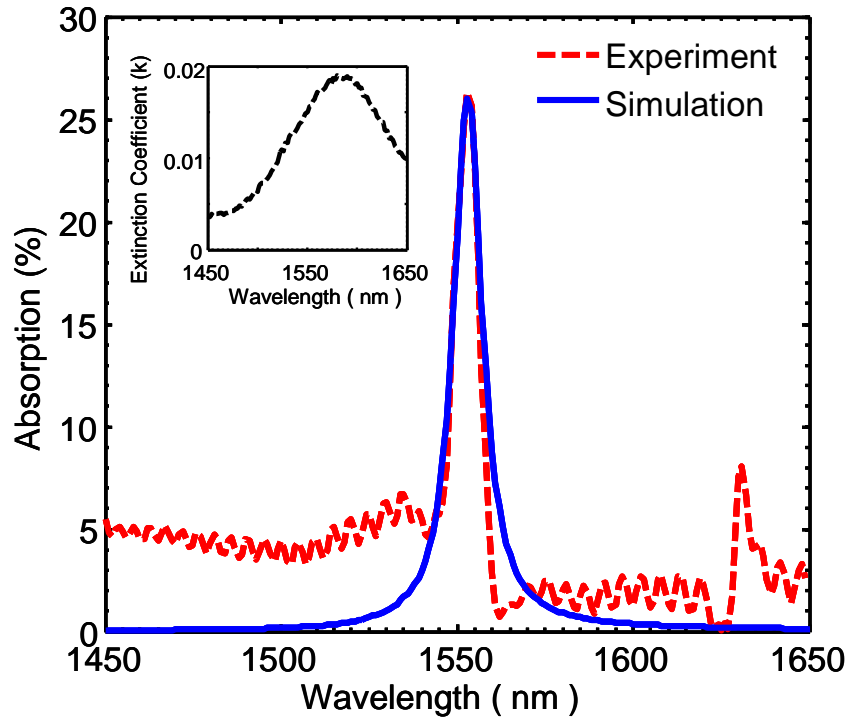


Figure 5.16 Experimental and simulated absorption characteristics for the Fano filter filled with CQDs. Shown in the inset is the spectra of CQD extinction coefficient, k.

To further illustrate the interactions between the Fano filters and the CQDs, and also to quantify the changes in the absorption due to the interactions, the absorption enhancement factor was carried out. Similar as the enhancement factor used for 2D PCS in Chapter 4,

absorption enhancement is defined as the ratio of the absorption of the CQDs inside Fano filters to that of the CQDs on glass substrate.

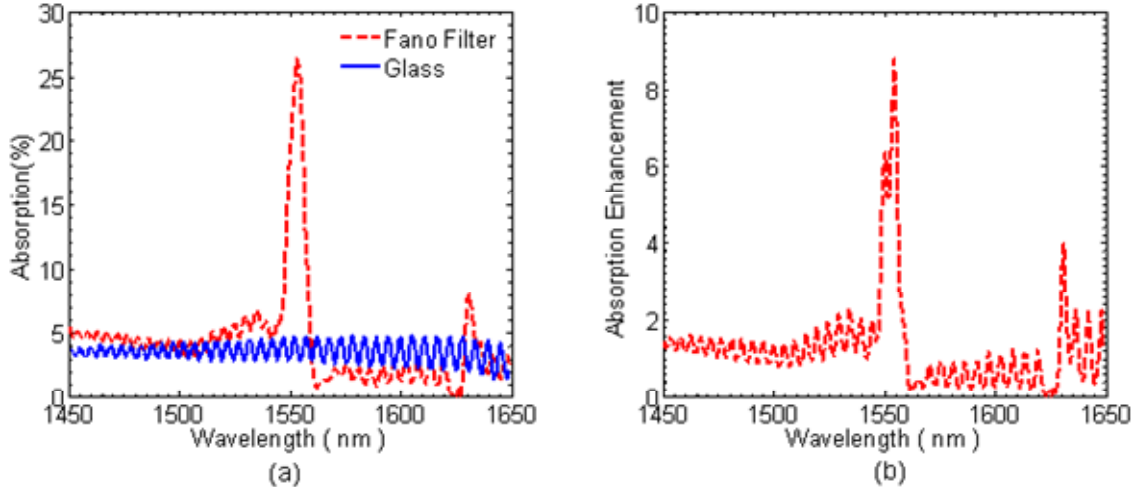


Figure 5.17 (a) Absorption of Fano filter and glass substrate (b) Absorption enhancement for Fano filter

Figure 5.17(a) show the absorption spectra of Fano filter and glass substrate. A profound absorption peak is found for Fano filter at Fano resonance region. While absorption of Fano filter in other spectrum region is comparable to glass substrate. The oscillation of glass absorption is due to interference. Figure 5.17(b) shows the absorption enhancement at Fano resonance region. There is a very good spectral overlap between this Filter resonance peak (shown in Figure 5.18(b) Filter1) and the PbSe QD high absorption region (Figure 5.18(a) QD₁). This overlap leads to an absorption enhancement factor of 9 at the resonance location of this Filter

In order to validate the origin of absorption in Fano resonance, two more sets of Fano filters samples and CQDs were investigated. In the second set, a Fano filter sample (Filter2 in Figure 5.18) was fabricated with Fano resonance at 1468 nm, by increasing the air hole radius (r) to 149 nm. This sample was filled with another spectrally-matched PbSe CQDs with the absorption peak at around 1450nm (QD₂ in Figure 5.18) . Following the same procedure, the absorption enhancement factor was derived and the data were plotted in Figure 5.18 (c). An

absorption enhancement factor of 18 for this sample was obtained, which may be due to the combined effects of a larger air fill factor, a higher quality factor of Fano resonance as well as a higher quantum efficiency of CQDs in this case.

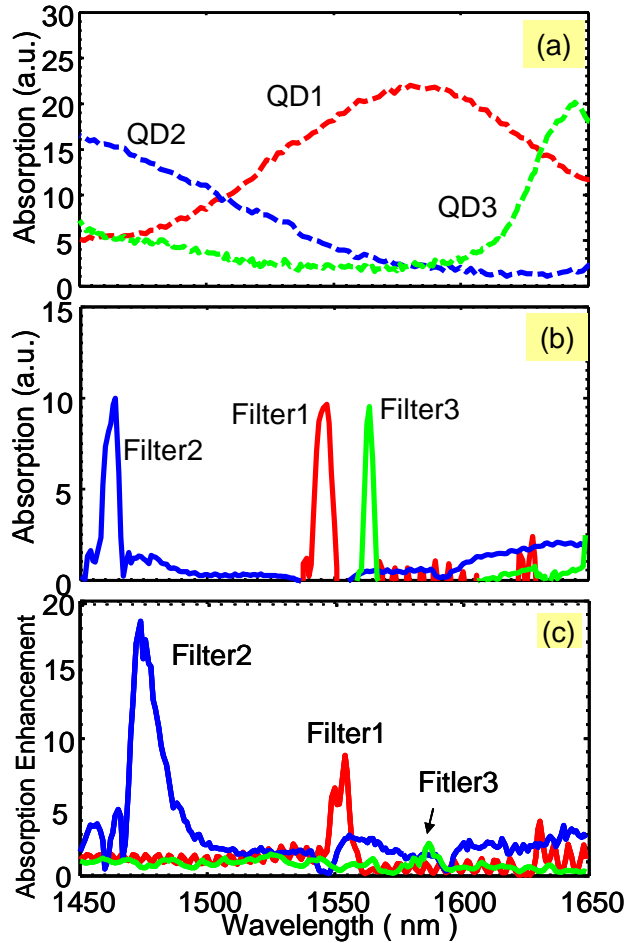


Figure 5.18 (a) Three sets of CQDs with different absorption peak locations; (b) Three different Fano filters with different resonance locations; and (c) Absorption enhancement factors for these three sets of samples.

Finally, another set of Fano filters (Filter 3) was fabricated with Fano resonance of 1564 nm, by reducing the air hole size to 103 nm in radius. CQDs with absorption peak at 1640nm (QD₃) were used here, which have no absorption at 1564 nm. In this case, there was no absorption observed around 1564 nm spectral regime. By comparing these three cases, it clearly indicates that the enhanced absorptions at different Fano resonance locations were

originated from the strong interactions between the absorptive medium (CQDs in this case) and the spectrally matched Fano resonances. Table 5.3 summarizes those three sets of absorption experiments

Table 5.3 Three set of Fano filter absorption experiments with different colloidal quantum dots

Parameters	First Set	Second Set	Third Set
Fano filter parameters	a=600nm r =114nm t=250nm	a=600nm r =149nm t=250nm	a=600nm r =103nm t=250nm
Fano resonance	1547nm	1468nm	1565nm
QDs absorption at Fano resonance	strong	strong	poor
Estimated effective hole index	1.09	1.09	1.20
Absorption Enhancement	8.76	18.55	2.52

It is also worth noting that the quality factors of Fano resonance in our experiments are far from optimal. According to our earlier theoretical work, one or two orders of absorption enhancements can be expected for the Fano filters with optimized quality factors. In addition, the fill factor of CQDs into the air holes of PC cavities can also be further increased.

The first set of sample on PET substrate was also used for CQDs angle dependent transmission investigation. Measured transmission spectra with incident angle θ varying from 0° to 20° were shown in Figure 5.19 under p-polarization light and ΓX sample orientation. Red-shifted spectra after CQDs backfilling were observed for the whole incident angle range, mostly due to high effective index in the air hole region, as explained earlier. The dip intensity, however, was related to the absorptions and reflection at different incident angles.

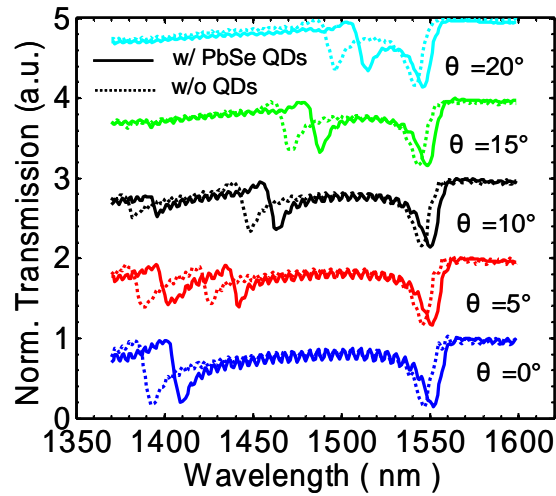


Figure 5.19 Measured incident angle θ dependent p-polarization transmission along with $\psi=0^\circ$, $\phi=0^\circ$ for Fano filter on PET substrate; solid and dash curves accounts for with and without PbSe QDs respectively.

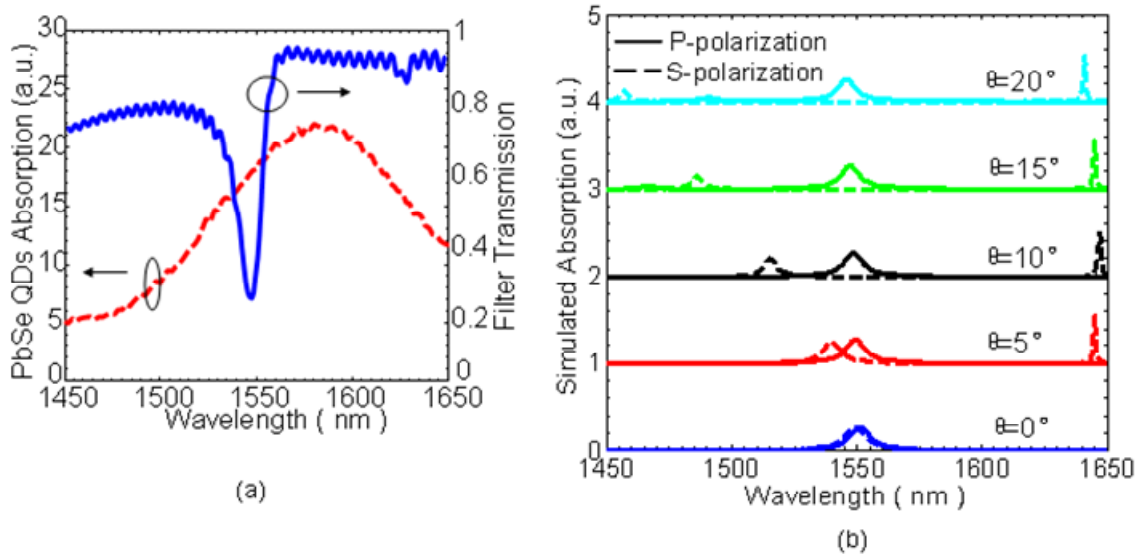


Figure 5.20 (a) Shows Fano filter transmission (solid blue) and PbSe quantum dots absorption (red dash) used for this simulation (b) Corresponding simulated absorption in this Fano filter on PET substrate with p-polarization (solid curves) and s-polarization light (dash curves)

Simulated angle dependent absorptions with p- and s- polarization light were also carried out on the first set of Fano filter as shown in Figure 5.20(b). With p-polarization light, the absorption at Fano resonance has little spectral shift and little intensity variation. On the other

hand, with s-polarization light, absorption of Fano filter will be reduced at blue shift Fano resonance region due to mismatched Fano resonance and CQD absorption. The simulation result here not only was consistent with the angle and polarization dependent transmission properties of Fano resonance, as discussed in chapter 4, but more importantly, it was also consistent with the absorption properties shown for three sets of Fano filter samples. All These findings confirm the feasibility of incorporation of PbSe QDs in SiNM Fano filters for angle, polarization, and spectral-dependent infrared photodetector design.

CHAPTER 6

INFRARED PHOTODETECTORS DESIGN BASED ON FANO FILTERS

Colloidal Quantum Dots(CQD) based infrared photodetectors have been developed by some groups[97, 98]. Compared to epitaxial grow QDs, solution-process infrared photodetectors offer low cost, large device area, physical flexibility and convenient materials integration. Previous chapter presents that absorption enhancement can be achieved by integrating PbSe CQDs with Fano filters. Here, more absorption characterization is carried out according to designed CQD infrared photodetectors.

6.1 Schottky Photodetectors Design

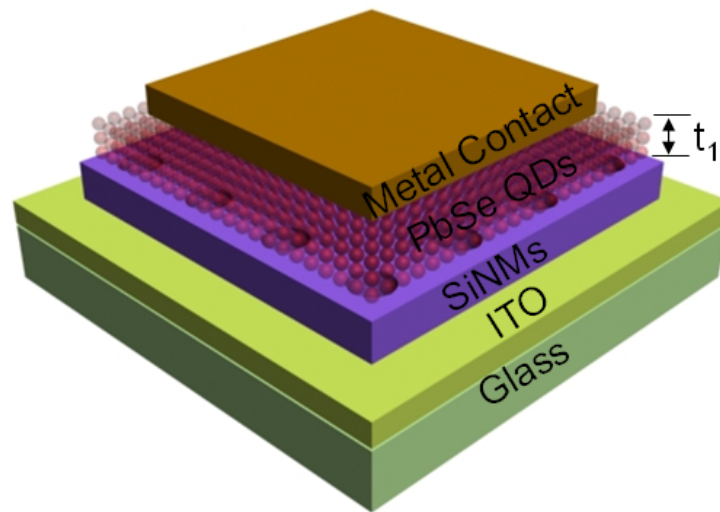


Figure 6.1 Schematically show the Schottky junction photodetector model

The first infrared photodetector model is shown in Figure 6.1 where the schottky junction is formed between p type PbSe or PbS CQDs layer and top metal contact. PbSe/PbS QD is typically synthesized with capped oleic acid which is electrically insulating due to 2.5-nm-long ligands. Exchanging long oleic acid ligands with short ligands is therefore needed to improve carrier mobility for infrared photodetectors. Some solutions have been proposed for ligand

exchange including 1,2-ethanedithiol (EDT) solution in acetonitrile[99], n-butylamine[98] and 1,4-benzenedithiol in anhydrous acetonitrile[100]. In order to make good contact and high junction potential for carrier extraction, some metals have been used such as Al[101], Ca/Al[99, 102], Al/Ag[103], Ag[104] and Au[98, 105] for CQD based optoelectronic devices. ITO used as two electrodes has been also reported[106].

Thickness of CQDs also plays the critical role for carrier collection. High absorption needs thick CQDs layer. However, too thick CQD layer reduces voltage output due to carrier recombination, and degrades EQE because of the dead region close to the bottom ITO contact. Here, we investigate absorption properties in this Schottky photodetectors model.

In real QDs deposition, due to small size of air hole ($r \sim 100-150\text{nm}$) and low air hole fill factor ($\sim 10\%$) in the Fano filter, only some of QDs fill into air holes but most of them could be just attached on the surface. The impact of QDs location on absorption was first investigated. The parameters of schottky photodetector model based on one possible Fano filter are summarized in Table 6.1. It is kept the same for the same Fano filter and QDs

Table 6.1 Some parameters in Schottky junction photodetector

Parameters	Value
Fano filter parameters	$a=600\text{nm}$ $r =109\text{nm}$ $t=256\text{nm}$
Fano resonance	$\lambda_1=1560\text{nm}$ $\lambda_2=1409\text{nm}$
QDs absorption peak	1562nm
Estimated effective hole index	1.1
Estimated effective index of QDs layer	1.5
Thickness of top QD layer	$t_1 \sim 26\text{ nm}$

Figure 6.2(a) shows PbSe QDs extinction coefficient used for simulation. The real part of refractive index of PbSe QDs solution is assumed to be 1.5. In this set of simulation, a 26nm thick QD layer on top or bottom of 256nm thick Fano filter are compared to ideal QDs filling

case in which the QDs are all injected into the air holes. As shown in Figure 6.2(b), the highest (34%) absorption is found in ideal 100% QDs filling case. While the absorption of top coating and bottom coating are slightly different and both of them are around 14%. So the real absorption could be between above two values. The absorption enhancement factor of 130 can be achieved in the ideal case as shown in Figure 6.3.

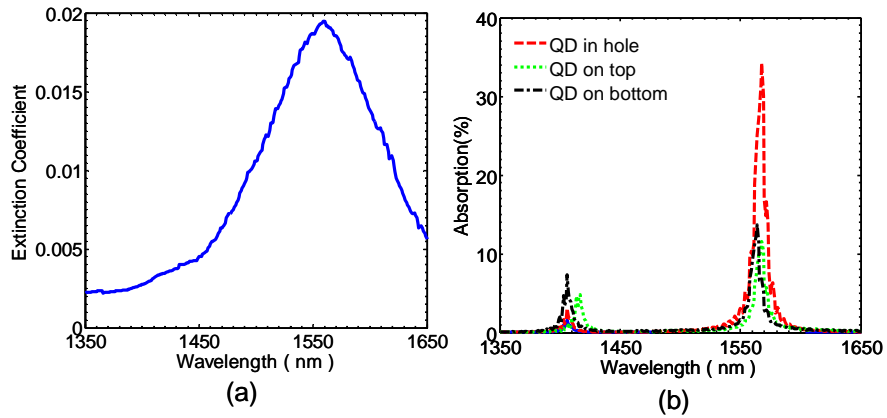


Figure 6.2 (a) The extinction coefficient of PbSe QDs used for the simulation (b) Absorption based on different QD locations on the Fano filters.

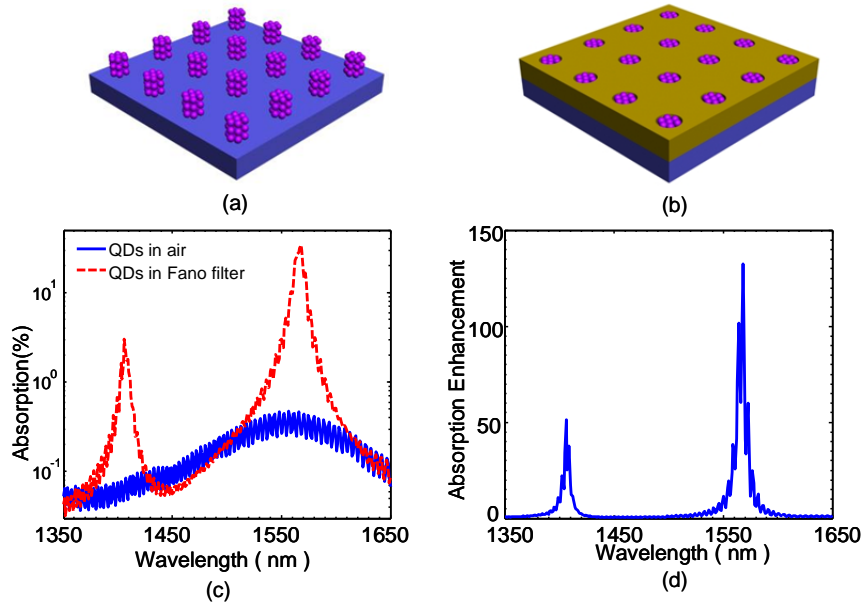


Figure 6.3 Schematically show (a)the QDs pillow on the glass substrate (b) QDs filled in the Fano filter (c) The absorption in case(a) and (b) (d) The absorption enhancement

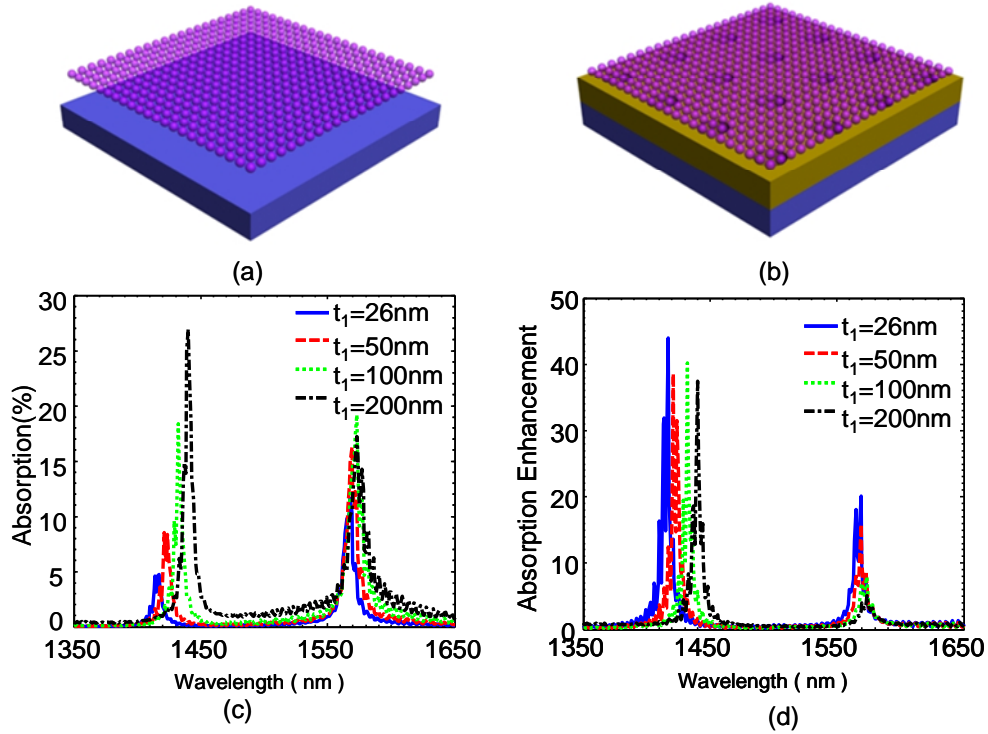


Figure 6.4 (a) The QDs layer above the glass substrate (b) The QDs layers coated on the Fano filter (c) The absorption in case(a) and (b) with different QD layer thickness (d) The absorption enhancement of different thick QD layers

The top QDs layer thickness (t_1 as shown in Figure 6.1) impact on absorption is also investigated. First, the absorption from Fano filter structure and from the reference structure (the same slab without air hole PC Fano filter pattern) are simulated. The results are shown in the Figure 6.4(c). The absorption peak around the primary Fano resonance region ($\lambda_1=1560\text{nm}$) is increased with the increase of QD thickness (t_1), and saturated at around $t_1=100\text{nm}$. Little spectral shift is found with the increase of t_1 up to 200nm. On the other hand, the absorption peak at a secondary Fano resonance region ($\lambda_2=1409\text{nm}$) shows different behavior. First, the absorption increases very quick with the increase of QD thickness t_1 . It could be due to the increased spectral overlap between Fano resonance and QD higher absorption region. Secondly, the absorption peak shifts quickly towards longer wavelengths (red-shift). For t_1 varying from 26 to 200nm, a 30nm spectral shift is found. It is worth to note that this multicolor

detection capability is very desirable for infrared photodetectors. Based on above findings, we found the optimal thickness of QD thin film layer should be 50-100 nm. Further optimization work could be done by better match of the QDs absorption peak with Fano resonance peak.

6.2 PN Photodetectors Design

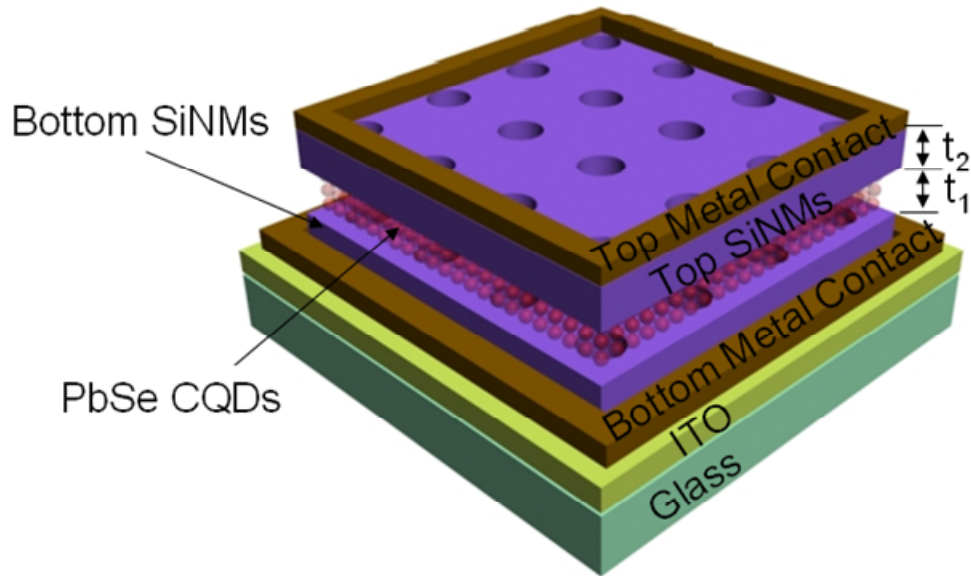


Figure 6.5 Schematically show the PN junction photodetector model

The second photodetector model is shown in Figure 6.5 where the QD layer is sandwiched by top p type Fano filter and bottom n type Fano filter. Too thick of Fano filter will generate more Fano resonance modes and degrade the quality factor of each mode. So, in this case, the thickness of both top and bottom Fano filter (t_2) should be thinner than that of the first Schottky photodetector model. As shown in Figure 6.6, the optimal t_2 is around 150nm.

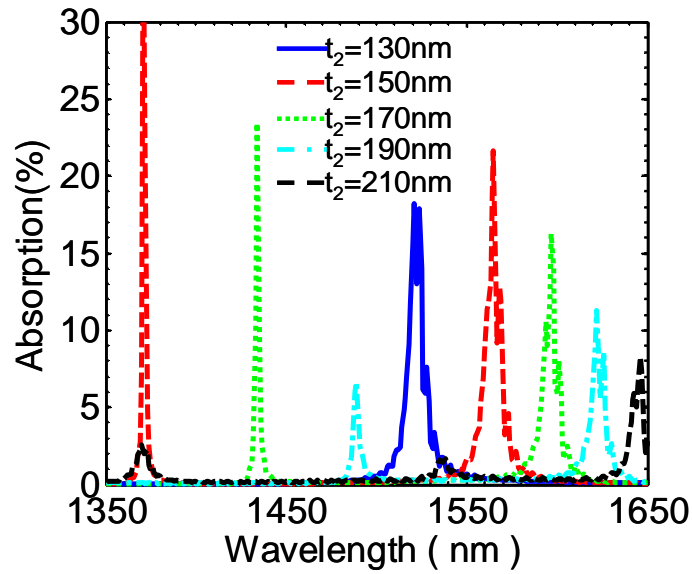


Figure 6.6 The thickness of top and bottom Fano filter impact on absorption

So the possible parameter design of pn photodetectors is summarized in the table below.

Table 6.2 Design parameters for pn junction photodetectors

Parameters	Value
Fano filter parameters	a=600nm r =109nm t ₂ =150nm
Fano resonance	λ=1542nm
QDs absorption peak	1562nm
Estimated effective hole index	1.1
Estimated effective index of QDs layer	1.5
Thickness of top QD layer	t ₁ =26 nm

It is worth to note that above two sets of photodetector designs mainly depend on optical absorption investigation. Other electrical factors should be considered as well in order to achieve high performance infrared photodetectors.

CHAPTER 7

CONCLUSIONS AND FUTURE WORK

7.1 Conclusions

The work presented here is quite multidisciplinary. Omni-AR coating is successfully designed for solar cells to effectively trap light on different solar cell material systems. Large angle independent and broadband spectra invariant low reflection is achieved by Omni-AR coating. Omni-AR coating can be fulfilled by cost-effect, simply solution process. The experimental transmission and reflection on different substrates agreed well with design value. More importantly, the measured short circuit currents and conversion efficiency on commercial organic or a-Si solar cells with Omni-AR coating are also increased.

The enhanced infrared absorption was investigated in detail for PC based structures. In 1D PC structure, optimal defect cavity and resonant cavity can achieve close to 98% and 93.4% absorption respectively. The infrared absorption enhancement factor in 2D PC defect cavity is more than 6000 under lateral illumination. By introduction of CQDs into Fano filter, the measured absorption enhancement is 18 as the Fano resonance is overlapped with CQDs absorption. Two photodetector designs based on the Fano resonance principle were finally proposed with fundamental absorption investigation.

7.2 Suggestion and Future Work

7.2.1. Light Trapping in Other Types of Solar Cells

In this dissertation, simulation of light trapping is limited on wafer level solar cells. However, Omni-AR should be also appropriate to many other type solar cells what has been proven experimentally at least for a-Si thin film and organic based solar cells. The corresponding simulation will be helpful.

7.2.2. 2D PCS Vertical Illumination Absorption

The absorption enhancement in this case is around 100. Although it is two orders lower than the lateral illumination case, it is close to the theoretical design value of Fano filters, and also much higher than that value in 1D PC structure. The impact of light illumination direction needs to be further investigated. Additionally, in practice, the real light source could be much larger than the simulated light source and the defect cavity region, so further optimizing the setup and 2D PCS could be considered.

7.2.3. Photodetector Design and Fabrication

PbSe/PbS CQDs involved photodetector devices is a challenging because of their instability chemical properties. Precise localizing QDs and EDT solution within the device area is critical to obtain good performance.

APPENDIX A
LIST OF PUBLICATIONS

Journal Publications

1. **Li Chen**, H. Yang, Z. Qiang, H. Pang, L. Sun, Z.Q. Ma, Ryan Pate, Adrienne Stiff-Roberts, S. Gao, J. Xu, Gail J. Brown and W. D. Zhou “Colloidal quantum dot absorption enhancement in flexible Fano filters”, Appl. Phys. Lett., 96 083111 (2010)
2. **Li Chen**, Z. Qiang, H. Yang, H. Pang, Z. Ma, and W. D. Zhou “Polarization and angular dependent transmissions on transferred nanomembrane Fano filters”, Optical. Express 17 8396 (2009)
3. W.D. Zhou, Z. Ma, H. Yang, Z. Qiang, G. Qin, H. Pang, **Li. Chen**, W. Yang, S. Chuwongin, and D. Zhao, “Flexible photonic-crystal Fano filters based on transferred semiconductor nanomembranes (review)”, J. Phys. D. in press (2009)
4. H. Yang, S. Chuwongin, Z. Qiang, **Li Chen**, H. Pang, Z. Ma, and W. D. Zhou “Resonance control of membrane reflectors with effective index engineering”, Appl. Phys. Lett., 95, 023110 (2009)
5. Y. Wang, R. Tummala, **Li Chen**, L. Q. Guo, W. D. Zhou and M. Tao, “Solution-processed omnidirectional antireflection coatings on amorphous silicon solar cells”, J. Appl. Phys. 105,103501 (2009).
6. Yuehui Wang, **Li Chen**, Hongjun Yang, Qing Guo, Weidong Zhou, Meng Tao “Spherical Antireflection Coatings by Large-Area Convective Assembly of Monolayer Silica Microspheres”, Solar Energy Materials and Solar Cells 93,85 (2009)
7. Zexuan Qiang, Hongjun Yang, **Li Chen**, Huiqing Pang, Zhenqiang Ma, and Weidong Zhou, “Fano filters based on transferred silicon nanomembranes on plastic substrates” Appl. Phys. Lett., 93, 061106 (2008)
8. M. Tao, W.D. Zhou, H. Yang and **Li Chen**, “Surface Texturing by Solution Deposition for Omni-Directional Anti-Reflection”, Appl. Phys. Lett., vol.91, 081118 (2007).

9. Weidong Zhou, Meng Tao, **Li Chen**, and Hongjun Yang "Microstructured surface design for omnidirectional antireflection coatings on solar cells", J. Appl. Phys. 102, 103105 (2007)
10. W. D. Zhou, **Li Chen**, Z. Qiang, G. J. Brown, "Spectrally selective infrared absorption in a single-defect photonic crystal slab", J. Nanophotonics, vol.1, 013515 (2007).
11. W. D. Zhou, Z. X. Qiang, **Li Chen**, "Photonic crystal defect mode cavity modelling: a phenomenological dimensional reduction approach (Invited)", J. Phys. D., vol. 40, pp. 2615-2623 (2007) (Special issue on photonic crystal devices).

Conference Proceedings

12. **Li Chen**, Hongjun Yang, Zexuan Qiang, Lei Sun, Zhenqiang Ma, Jian Xu, Ryan Pate, Adrienne Stiff-Roberts, Gail J. Brown, and Weidong Zhou "Direct measurement of spectrally selective absorption enhancement in Fano resonance photonic crystal cavities on plastic substrates" Proc. SPIE 7609, 76090E (2010)
13. Weidong Zhou, Zhenqiang Ma, Hongjun Yang, **Li Chen**, Weiquan Yang, Zexuan Qiang, Guoxuan Qin, Huiqing Pang, Santhad Chuwongin, and Deyin Zhao "Semiconductor nanomembranes for stacked and flexible photonics" Proc. SPIE 7606, 76060U (2010)
14. **Li Chen**, Hongjun Yang, Zexuan Qiang, Huiqing Pang, Zhenqiang Ma, Jian Xu, Gail Brown, Weidong Zhou Proc. SPIE Vol.7222 72220V-1-8 (2009)
15. **Li Chen**, Hongjun Yang, Meng Tao and Weidong Zhou "Microstructured anti-reflection surface design for the omni-directional solar cells" Proc. SPIE Vol.7046, 704608 (Sep. 11, 2008)
16. Zexuan Qiang, **Li Chen**, Hongjun Yang, Huiqing Pang, Zhenqiang Ma, and Weidong Zhou "Fano filter modal analysis based on transferred silicon nanomembranes on flexible substrates" Proc. SPIE Vol. 7031, 703109 (Aug. 29, 2008)

17. Weidong Zhou, Zexuan Qiang, **Li Chen**, Hongjun Yang, and Gail J. Brown "Spectrally selective infrared absorption enhancement in photonic crystal cavities" Proc. SPIE Vol. 7095, 709507 (Aug. 26, 2008)
18. H. Yang, **Li Chen**, Z. Qiang, W. D. Zhou, W. Zhang, A. D. Stiff-Roberts, S. Krishna, G. J. Brown, "Characteristics of photonic crystal cavity based infrared photodetectors", IEEE LEOS Annual Meeting, Oct. 17-21, (2007).
19. **Li Chen**, Z. X. Qiang, W. D. Zhou, G. J. Brown" Spectrally Selective Absorption Enhancement in Photonic Crystal Defect Cavities", Proc. SPIE, vol. 6480, 64801C, (2007).
20. W. D. Zhou, H. Yang, **Li Chen**, Z. Qiang, A. D. Stiff-Roberts, G. J. Brown, "Photonic crystals for spectrally selective infrared photonics (INVITED)", The 6th Asia-Pacific Conference on Near-Field Optics, Yellow Mountain, China, June 13-17, (2007).
21. H. J. Yang, **Li Chen**, Z.X. Qiang, W. D. Zhou, "Photonic Crystal Infrared Photodetector Design and Fabrication", The Best Little Nano Conference in Texas, April 4-5, (2007). Austin, TX.
22. W. D. Zhou, **Li Chen**, H.J. Yang, Z.X. Qiang, "Photonic crystals for spectrally selective infrared silicon photonics", Nano and Giga Challenges in Electronics and Photonics(Symposium and Spring School), March 12-16, (2007). Phoenix, Arizona.
23. H. J. Yang, **Li Chen**, Z. X. Qiang, M. Lu, W.D. Zhou, G. J. Brown, A. Stiff-Roberts, S. Krishna, "Photonic Crystal Infrared Photodetector Design and Fabrication (Invited)", Texas SRPING Conference IV, Feb. 6-7, (2007).
24. **Li Chen**, Z. X. Qiang, W. D. Zhou, G. J. Brown" Spectrally Selective Absorption Enhancement in Photonic Crystal Defect Cavities", Photonics West (PW'07), Jan. 21-26, (2007). San Jose, CA.
25. **Li Chen**, W.D. Zhou, Z. X. Qiang, G. Brown, "Spectral Selectivity of Photonic Crystal Infrared Photodetectors", Proc. SPIE, vol. 6370, 63701I, (2006).

26. **Li Chen**, W.D. Zhou, G. Brown, "Spectral Selectivity of Photonic Crystal Infrared Photodetectors", Optics East, Oct. 1-4, (2006), Boston, MA.
27. W. D. Zhou, **Li Chen**, G. Thiruvengadam, H. Yang, " Novel photonic crystal structures for active nanophotonic devices", ETIC'06, Aug. 10-12, (2006), Richardson, TX.

REFERENCES

- [1] I. E. Agency, "Key World Energy Statistics," 2009.
- [2] <http://www.eia.doe.gov/cneaf/solar.renewables/page/solarphotv/solarpv.html>.
- [3] M. I. Hoffert, K. Caldeira, A. K. Jain, E. F. Haites, L. D. D. Harvey, S. D. Potter, M. E. Schlesinger, S. H. Schneider, R. G. Watts, T. M. L. Wigley, and D. J. Wuebbles, "Energy implications of future stabilization of atmospheric CO₂ content," *Nature*, vol. 395, p. 881, 1998.
- [4] <http://nsl.caltech.edu>.
- [5] A. Rogalski, "Infrared detectors: an overview," *Infrared Physics & Technology*, vol. 43, p. 187, 2002.
- [6] B.F.Levine, "Quantum-well infrared photodetectors," *Journal of Applied Physics*, vol. 74, p. R1, 1993.
- [7] J. Piotrowski and A. Rogalski, *High-Operating-Temperature Infrared Photodetectors*: SPIE Publications; illustrated edition, 2007.
- [8] P. Martyniuk and A.Rogalski, "Review Quantum-dot infrared photodetectors: Status and outlook," *Progress in Quantum Electronics*, vol. 32, p. 89, 2008.
- [9] A. Luque and S.Hegedus, *Handbook of Photovoltaic Science and Engineering* New York: Wiley, 2003.
- [10] M. Hall, A. Roos, and B. r. Karlsson, "Reflector Materials for Two dimensional Low-concentrating Photovoltaic Systems: the Effect of Specular versus Diffuse Reflectance on the Module Efficiency," *Prog. Photovolt: Res. Appl.*, vol. 13, p. 217, 2005.
- [11] H. A, M. I, F. P, N. S, R. S, and B. TM., "A simplified process for isotropic texturing of mc-Si," Osaka, 2003, p. 1447.
- [12] I. Y, F. K, and S. K., "Surface texturing of large area multicrystalline silicon solar cells using reactive ion etching method," *Sol. Energ. Mater. Sol. Cells*, vol. 48, p. 237, 1997.
- [13] N. H, N. M, T. Y, M. S, T. T, and N. T. Machida T, "Polycrystalline silicon solar cells with V-grooved surface," *Sol. Energ. Mater. Sol. Cells*, vol. 34, p. 219, 1994.
- [14] S. MJ, C. AJ, and B. AW, "Texturing of polycrystalline silicon," *Sol. Energ. Mater. Sol. Cells*, vol. 40, p. 33, 1996.
- [15] O. Kluth, B. Recha, L. Houbena, S. Wiedera, G. Schöpea, C. Benekinga, H. Wagnera, A. Löfflb, and H. W. Schockb, "Texture etched ZnO:Al coated glass substrates for silicon based thin film solar cells," *Thin Solid Films*, vol. 351, p. 247, 1999.

- [16] M. Abbott and J. Cotter, "Optical and Electrical Properties of Laser Texturing for High-efficiency Solar Cells," *Prog. Photovolt: Res. Appl.*, vol. 14, p. 225, 2006.
- [17] J. Zhao, A. Wang, P. Campbell, and M. A. Green, "22.7% Efficient Silicon Photovoltaic Modules with Textured Front Surface," *IEEE Transaction on Electron Devices*, vol. 46, p. 1495, 1999.
- [18] J. Zhu, Z. Yu, G. F. Burkhard, C.-M. Hsu, S. T. Connor, Y. Xu, Q. Wang, M. McGehee, S. Fan, and Y. Cui, "Optical Absorption Enhancement in Amorphous Silicon Nanowire and Nanocone Arrays," *Nano Letters*, vol. 9, p. 279, 2009.
- [19] C.-H. Sun, P. Jiang, and B. Jiang, "Broadband moth-eye antireflection coatings on silicon," *Appl. Phys. Lett.*, vol. 92, p. 061112, 2008.
- [20] A. J. Nozik, "Quantum dot solar cells," *Physica E: Low-dimensional Systems and Nanostructures*, vol. 14, p. 115, 2002.
- [21] K. Bamham, I. Ballard, J. Barnes, J. Connolly, P. Griffin, B. Klufftinger, J. Nelson, E. Tsui, and A. Zachariou, "Quantum well solar cells," *Applied Surface Science*, vol. 113, p. 722, 1997.
- [22] N. S. Lewis, "Toward Cost-Effective Solar Energy Use," *Science*, vol. 315, p. 798, 2008.
- [23] B. Tian, X. Zheng, T. J. Kempa, Y. Fang, N. Yu, G. Yu, J. Huang, and C. M. Lieber, "Coaxial silicon nanowires as solar cells and nanoelectronic power sources," *Nature*, vol. 449, p. 885, 2007.
- [24] K. T. Posani, V. Tripathi, S. Annamalai, N. R. Weisse-Bernstein, and S. Krishna, "Nanoscale quantum dot infrared sensors with photonic crystal cavity," *Applied Physics Letters*, vol. 88, p. 151104, 2006.
- [25] G. Karunasiri, J. S. Park, J. Chen, R. Shih, J. F. Scheihing, and M. A. Dodd, "Normal incident InGaAs/GaAs multiple quantum well infrared detector using electron intersubband transitions," *Applied Physics Letters*, vol. 67, p. 2600, 1995.
- [26] B.-M. Nguyen, D. Hoffman, P.-Y. Delaunay, and a. M. Razeghi, "Dark current suppression in type II InAs/GaSb superlattice long wavelength infrared photodiodes with M-structure barrier," *Applied Physics Letters*, vol. 91, p. 163511, 2007.
- [27] H.C.Liu, "Quantum dot infrared photodetectors," *Opto-Electronics Review*, vol. 11, p. 1, 2003.
- [28] D. W. Prather, S. Shi, J. Murakowski, G. J. Schneider, Ahmed Sharkawy, C. Chen, and B. Miao, "Photonic Crystal Structures and Applications: Perspective, Overview, and Development," *IEEE Journal of Selected Topics in Quantum Electronics*, vol. 12, p. 1416, 2006.
- [29] S. Noda and T. Baba, *Roadmap on Photonic Crystals*: Springer, 2003.
- [30] S. Y. Lin, J. G. Fleming, Z. Y. Li, I. El-Kady, R. Biswas, and K. M. Ho, "Origin of absorption enhancement in a tungsten, three-dimensional photonic crystal," *J. Opt.Soc.Am.B*, vol. 20, p. 1538, 2003.

- [31] J. G. Fleming, S. Y. Lin, I. El-Kady, R. Biswas, and K.M. Ho, "All-metallic three-dimensional photonic crystals with a large infrared bandgap," *Nature*, vol. 417, p. 52, 2002.
- [32] L. Chen, W. Zhou, Z. Qiang, and G. J. Brown, "Spectral Selectivity of Photonic Crystal Infrared Photodetectors," in *SPIE*, 2006, pp. 637011-1.
- [33] M. Fujita, S. Takahashi, Y. Tanaka, T. Asano, and S. Noda, "Simultaneous inhibition and redistribution of spontaneous light emission in photonic crystals," *Science*, vol. 308, p. 1296, 2005.
- [34] S. Fan and J. D. Joannopoulos, "Analysis of guided resonances in photonic crystal slabs," *Phys.Rev.B*, vol. 65, p. 235112, 2002.
- [35] U. Fano, "Effects of Configuration Interaction on Intensities and Phase Shifts," *Phys. Rev.*, vol. 124, p. 1866, 1961.
- [36] R. Magnusson and S. S. Wang, "New principle for optical filters," *Appl. Phys. Lett.*, vol. 61, p. 1022, 1992.
- [37] S. T. Thurman and G. M. Morris, "Controlling the spectral response in guided-mode resonance filter design," *Appl. Opt.*, vol. 42, p. 3225, 2003.
- [38] A. Rosenberg, M. Carter, J. Casey, M. Kim, R. Holm, R. Henry, C. Eddy, V. Shamamian, K. Bussmann, S. Shi, and D. W. Prather, "Guided resonances in asymmetrical GaN photonic crystal slabs observed in the visible spectrum," *Opt. Express*, vol. 13, p. 6564, 2005.
- [39] C. Y. Chao, "Biochemical sensors based on polymer microrings with sharp asymmetrical resonance," *Appl. Phys. Lett.*, vol. 83, p. 1527, 2003.
- [40] W. Suh, O. Solgaard, and S. Fan, "Displacement sensing using evanescent tunneling between guided resonances in photonic crystal slabs," *Journal of Applied Physics*, vol. 98, p. 033102, 2005.
- [41] E. V. Kerschaver and G. Beaucarne, "Back-contact Solar Cells: A Review," *Prog. Photovolt: Res. Appl.*, vol. 14, p. 107, 2006.
- [42] J. A. Dobrowolski, D. Poitras, H. V. P. Ma, and M. Acree, "Toward Perfect Antireflection Coatings: Numerical Investigation," *Appl. Opt.*, vol. 41, p. 3075, 2002.
- [43] D. Poitras and J. A. Dobrowolski, "Toward Perfect Antireflection Coatings. 2. Theory," *Appl. Opt.*, vol. 43, p. 1286, 2004.
- [44] E. Hecht, *Optics (4th edition)*: Addison Wesley, 2002.
- [45] J. Zhao, A. Wang, P. Altermatt, and M. A. Green, "Twenty-four percent efficient silicon solar cells with double layer antireflection coatings and reduced resistance loss," *Appl. Phys. Lett.*, vol. 66, p. 3636, 1995.

- [46] S.-Y. Liena, D.-S. Wuua, W.-C. Yehb, and J.-C. Liu, "Tri-layer antireflection coatings (SiO₂/SiO₂-TiO₂/TiO₂) for silicon solar cells using a sol-gel technique," *Sol. Energ. Mater. Sol. Cells*, vol. 90, p. 2710, 2006.
- [47] J. Q. Xi, M. F. Schubert, J. K. Kim, E. F. Schubert, M. Chen, S. Y. Lin, W. Liu, and J. A. Smart, "Optical thin-film materials with low refractive index for broadband elimination of Fresnel reflection," *Nature Photonics*, vol. 1, p. 176, 2007.
- [48] W. H. Southwell, "Gradient-index antireflection coatings," *Optics Letters*, vol. 8, p. 584, 1983.
- [49] E. Yablonovitch, "Statistical ray optics," *J. Opt. Soc. Am.*, vol. 72, p. 899, 1982.
- [50] P. Campbell and M. A. Green, "Light trapping properties of pyramidally textured surfaces," *J. Appl. Phys.*, vol. 62, p. 243, 1987.
- [51] M. C. Bautista and A. Morales, "Silica antireflective films on glass produced by the sol-gel method," *Sol. Energ. Mater. Sol. Cells*, vol. 80, p. 217, 2003.
- [52] D. Lee, M. F. Rubner, and R. E. Cohen, "All-Nanoparticle Thin Film Coatings," *Nano Letters*, vol. 6, p. 2305, 2006.
- [53] D. Chen, "Anti-reflection (AR) coatings made by sol-gel processes: A review," *Sol. Energ. Mater. Sol. Cells*, vol. 68, p. 313, 2001.
- [54] Q. Chen, G. Hubbard, P. A. Shields, C. Liu, D. W. E. Allsopp, W. N. Wang, and S. Abbott, "Broadband moth-eye antireflection coatings fabricated by low-cost nanoimprinting," *Appl. Phys. Lett.*, vol. 94, p. 263118, 2009.
- [55] M. Tao, W. Zhou, H. Yang, and L. Chen, "Surface texturing by solution deposition for omnidirectional antireflection," *Appl. Phys. Lett.*, vol. 91, p. 081118, 2007.
- [56] W. Zhou, M. Tao, L. Chen, and H. Yang, "Microstructured surface design for omnidirectional antireflection coatings on solar cells," *J. Appl. Phys.*, vol. 102, p. 103105, 2007.
- [57] A. Yariv and P. Yeh, *Optical Waves in Crystals : Propagation and Control of Laser Radiation* Wiley-Interscience, 2002.
- [58] M. G. Moharam and T. K. Gaylord, "Rigorous coupled-wave analysis of planar-grating diffraction," *J. Opt. Soc. Am.*, vol. 71, p. 811, 1981.
- [59] K. C. Johnson, "Coupled Scalar Wave Diffraction Theory," *Applied Physics A: Materials Science & Processing*, vol. 24, p. 249, 1981.
- [60] M. Nevière and E. Popov, *Light Propagation in Periodic Media*. New York: MarcelDekker, Inc., 2003.
- [61] L. Li, "Formulation and comparison of two recursive matrix algorithms for modeling layered diffraction gratings," *J. Opt. Soc. Am. A*, vol. 13, p. 1024, 1996.
- [62] M. A. Green, "Polycrystalline silicon on glass for thin-film solar cells," *Appl Phys A*, vol. 96, p. 153, 2009.

- [63] <http://rredc.nrel.gov/solar/spectra/am1.5/>.
- [64] J. Zhao and M. A. Green, "Optimized Antireflection Coatings for High-Efficiency Silicon Solar Cells," *IEEE Transactions on Electron Devices*, vol. 38, p. 1925, 1991.
- [65] Y. Wang and W. Zhou, "A Review on Inorganic Nanostructure Self-Assembly," *Journal of Nanoscience and Nanotechnology*, vol. 10, p. 1563, 2010.
- [66] Y. Wang, L. Chen, H. Yang, Q. Guo, W. Zhou, and M. Tao, "Spherical antireflection coatings by large-area convective assembly of monolayer silica microspheres," *Sol. Energ. Mater. Sol. Cells*, vol. 93, p. 85, 2009.
- [67] Y. Wang, R. Tummala, L. Chen, L. Q. Guo, W. Zhou, and M. Tao, "Solution-processed omnidirectional antireflection coatings on amorphous silicon solar cells," *J. Appl. Phys.*, vol. 105, p. 103501, 2009.
- [68] S. Y. Lin, J. G. Fleming, Z. Y. Li, I. El-Kady, R. Biswas, and K. M. Ho, "Origin of absorption enhancement in a tungsten, three-dimensional photonic crystal," *J. Opt. Soc. Am. B*, vol. 20, p. 1538, 2003.
- [69] M. Sigalas, C. M. Soukoulis, E. N. Economou, C. T. Chan, and K. M. Ho, "Photonic band gaps and defects in two dimensions: Studies of the transmission coefficient," *Phys. Rev. B*, vol. 48, p. 14121, 1993.
- [70] E. Özbay, G. Tuttle, M. Sigalas, C. M. Soukoulis, and K. M. Ho, "Defect structures in a layer-by-layer photonic band-gap crystal," *Phys. Rev. B*, vol. 51, p. 13961, 1995.
- [71] P. Yeh, *Optical waves in layered media*. New York: Wiley, 1998.
- [72] J. D. Joannopoulos, S. G. Johnson, J. N. Winn, and R. D. Meade, *Photonic Crystals: Molding the Flow of Light, 2nd edition*: Princeton University Press, 2008.
- [73] A. Taflove, *Computational Electrodynamics: the Finite-Difference Time-Domain method* Boston: Artech House, 1995.
- [74] B. S. Song, S. Noda, T. Asano, and Y. Akahane, "Ultra-high-Q photonic double-heterostructure nanocavity," *Nature Mat.*, vol. 4, p. 207, 2005.
- [75] E. Kuramochi, M. Notomi, S. Mitsugi, A. Shinya, and T. Tanabe, "Ultra-high-Q photonic crystal nanocavities realized by the local width modulation of a line defect," *Appl. Phys. Lett.*, vol. 88, p. 041112, 2006.
- [76] W. L. Barnes, A. Dereux, and T. W. Ebbesen, "Surface plasmon subwavelength optics," *Nature*, vol. 424, p. 824, 2003.
- [77] W. Suh, "Displacement-sensitive photonic crystal structures based on guided resonance in photonic crystal slabs," *Appl. Phys. Lett.*, vol. 82, p. 1999, 2003.
- [78] Y. Kanamori, T. Kitani, and K. Hane, "Control of guided resonance in a photonic crystal slab using microelectromechanical actuators," *Appl. Phys. Lett.*, vol. 90, p. 031911, 2007.

- [79] K. B. Crozier, V. Lousse, O. Kilic, S. Kim, S. Fan, and O. Solgaard, "Air-bridged photonic crystal slabs at visible and near-infrared wavelengths," *Phys. Rev. B* vol. 73, p. 115126, 2006.
- [80] C. Grillet, D. Freeman, B. Luther-Davies, S. Madden, R. McPhedran, D. J. Moss, M. J. Steel, and B. J. Eggleton, "Characterization and modeling of Fano resonances in chalcogenide photonic crystal membranes," *Opt. Express*, vol. 14, p. 369, 2006.
- [81] L. Zhou and A. W. Poon, "Fano resonance-based electrically reconfigurable add-drop filters in silicon microring resonator-coupled Mach-Zehnder interferometers," *Opt. Express*, vol. 32, p. 781, 2007.
- [82] S. Fan, "Sharp asymmetric line shapes in side-coupled waveguide-cavity systems," *Appl. Phys. Lett.*, vol. 80, p. 908, 2002.
- [83] L. Y. Mario, S. Darmawan, and M. K. Chin, "Asymmetric Fano resonance and bistability for high extinction ratio, large modulation depth, and low power switching," *Opt. Express*, vol. 14, p. 12770, 2006.
- [84] C. Y. Chao, "Biochemical sensors based on polymer microrings with sharp asymmetrical resonance," *Appl. Phys. Lett.*, vol. 83, p. 1527, 2003.
- [85] W. Suh, O. Solgaard, and S. Fan, "Displacement sensing using evanescent tunneling between guided resonances in photonic crystal slabs," *J. Appl. Phys.*, vol. 98, p. 033102, 2005.
- [86] D. L. C. Chan, I. Celanovic, J. D. Joannopoulos, and M. Soljacic, "Emulating one-dimensional resonant Q-matching behavior in a two-dimensional system via Fano resonances," *Phys. Rev. A* vol. 74, p. 64901, 2006.
- [87] V. Lousse, W. Suh, O. Kilic, S. Kim, O. Solgaard, and S. Fan, "Angular and polarization properties of a photonic crystal slab mirror," *Opt. Express*, vol. 12, p. 1575, 2004.
- [88] S. Boutami, B. B. Bakir, H. Hattori, X. Letartre, J. L. Leclercq, P. Rojo-Romeo, C. M. Garrigues, Seassal, and P. Viktorovitch, "Broadband and compact 2-D photonic crystal reflectors with controllable polarization dependence," *IEEE, Photonics Technology Letters*, vol. 18, p. 835, 2006.
- [89] B. B. Bakir, C. Seassal, X. Letartre, P. Viktorovitch, M. Zussy, L. D. Cioccio, and J. M. Fedeli, "Surface-emitting microlaser combining two-dimensional photonic crystal membrane and vertical Bragg mirror," *Appl. Phys. Lett.*, vol. 88, p. 081113, 2006.
- [90] A. M. Yacomotti, F. Raineri, G. Vecchi, P. Monnier, R. Raj, A. Levenson, B. B. Bakir, C. Seassal, X. Letartre, and P. Viktorovitch, "All-optical bistable band-edge Bloch modes in a two-dimensional photonic crystal," *Appl. Phys. Lett.*, vol. 88, p. 231107, 2006.
- [91] M. F. Yanik and S. Fan, "Stopping and storing light coherently," *Phys. Rev. A*, vol. 71, p. 13803, 2005.
- [92] E. Drouard, H. Hattori, C. Grillet, A. Kazmierczak, X. Letartre, P. Rojo-Romeo, and P. Viktorovitch, "Directional channel-drop filter based on a slow Bloch mode photonic crystal waveguide section," *Opt. Express*, vol. 13, p. 3037, 2005.

- [93] H. C. Yuan, Z. Ma, M. M. Roberts, D. E. Savage, and M. G. Lagally, "High-speed strained-single-crystal-silicon thin-film transistors on flexible polymers," *J. Appl. Phys.*, vol. 100, p. 013708, 2006.
- [94] H. Yang, Z. Qiang, H. Pang, Z. Ma, and W. D. Zhou, "Surface-Normal Fano Filters Based on Transferred Silicon Nanomembranes on Glass Substrates," *Electron. Lett.*, vol. 44, p. 858, 2008.
- [95] Z. Qiang, H. Yang, L. Chen, H. Pang, Z. Ma, and W. D. Zhou, "Fano filter modal analysis based on transferred silicon nanomembranes on flexible substrates," *Appl. Phys. Lett.*, vol. 93, p. 061106, 2008.
- [96] J. Xu, D. Cui, T. Zhu, G. Paradee, Z. Liang, Q. Wang, S. Xu, and A. Y. Wang, "Synthesis and surface modification of PbSe/PbS core-shell nanocrystals for potential device applications," *Nanotechnology*, vol. 17, p. 5428, 2006.
- [97] K. R. Choudhury, W. J. Kim, Y. Sahoo, K.-S. Lee, and P. N. Prasad, "Solution-processed pentacene quantum-dot polymeric nanocomposite for infrared photodetection," *Appl. Phys. Lett.*, vol. 89, p. 051109, 2006.
- [98] G. Konstantatos, I. Howard, A. Fischer, S. Hoogland, J. Clifford, E. Klem, L. Levina, and E. H. Sargent, "Ultrasensitive solution-cast quantum dot photodetectors," *Nature*, vol. 442, p. 180, 2006.
- [99] J. M. Luther, M. Law, M. C. Beard, Q. Song, M. O. Reese, R. J. Ellingson, and A. J. Nozik, "Schottky Solar Cells Based on Colloidal Nanocrystal Films," *Nano Letters*, vol. 8, p. 3488, 2008.
- [100] J. Tang, L. Brzozowski, D. A. R. Barkhouse, X. Wang, R. Debnath, R. Wolowiec, E. Palmiano, L. Levina, A. G. Pattantyus-Abraham, D. Jamakosmanovic, and E. H. Sargent, "Quantum Dot Photovoltaics in the Extreme Quantum Confinement Regime: The Surface-Chemical Origins of Exceptional Air- and Light-Stability," *Nano Letters*, vol. 4, p. 869, 2010.
- [101] D. Cui, J. Xu, S.-Y. Xu, G. Paradee, B. A. Lewis, and M. D. Gerhold, "Infrared photodiode based on colloidal PbSe nanocrystal quantum dots," *IEEE Transaction on Electron Devices*, vol. 5, p. 362, 2006.
- [102] Q. SUN¹, Y. A. WANG², L. S. LI, D. WANG, T. ZHU, J. XU, C. YANG, and Y. LI, "Bright, multicoloured light-emitting diodes based on quantum dots," *Nature Photonics*, vol. 1, p. 717, 2007.
- [103] K. W. Johnston, A. G. Pattantyus-Abraham, J. P. Clifford, S. H. Myrskog, D. D. MacNeil, Larissa Levina, and E. H. Sargent, "Schottky-quantum dot photovoltaics for efficient infrared power conversion" *Appl. Phys. Lett.*, vol. 92, p. 131115, 2008.
- [104] D. C. Oertel, "Photodetectors Based on Colloidal Quantum Dots," in *Department of Chemistry*. vol. PhD: MIT, 2001.
- [105] S. Hoogland, V. Sukhovatkin, H. Shukla, J. Clifford, L. Levina, and E. H. Sargent, "Megahertz-frequency large-area optical modulators at 1.55 μm based on solution-cast colloidal quantum dots," *Optics Express*, vol. 16, p. 6683, 2008.

- [106] A. C. Arango, D. C. Oertel, Y. Xu, Mounji G. Bawendi, and V. Bulovic', "Heterojunction Photovoltaics Using Printed Colloidal Quantum Dots as a Photosensitive Layer," *Nano Letters*, vol. 9, p. 860, 2009.

BIOGRAPHICAL INFORMATION

Li Chen was born on Jan 17, 1974 in Anqing City, Anhui Province, China. His parents are Xiusheng Chen and Fengqiao Liu. In Anqing, he received his fundamental education at GaoQi School, the junior secondary education at The Fourth Middle School and senior secondary education at the First Middle School. He received his B.S. degree in Electronics Engineering from Hefei University of Technology in 1996. After graduation, he worked at Bank of China, Hefei branch. He finished his first year graduate study in 1999 at University of Science and Technology of China and transferred to the Chinese Academy of Sciences, Anhui branch until leaving in 2002. In 2004, he received his Master degree in Physics from University of Miami.

From June 2, 2005, he joined Prof. Weidong Zhou's NanoPhotonics group in Electrical Engineering at University of Texas at Arlington, pursuing his PhD degree and worked as a research assistant.

On August 4, 2009, his wife, Juanzhen He, gave birth to a lovely daughter, Nicole.

He enjoys his current research of solar cells and photodetectors. He plans to pursue his career in these two fields after graduation in 2010.